Carbon and sulfide metabolism of cable bacteria: investigated by stable-isotopic labelling and anoxic perturbation methods

Master thesis project performed within the context of the master programme Earth, Life and Climate

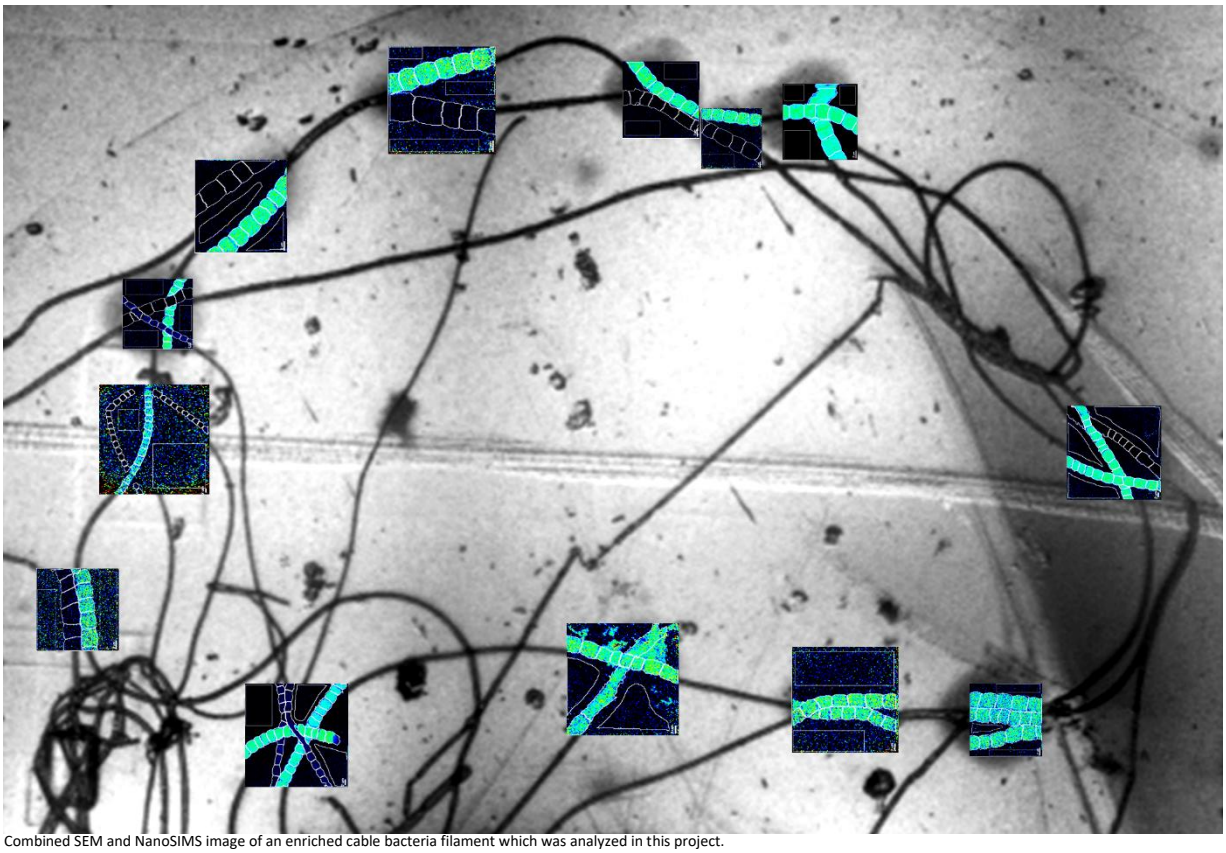

Combined SEM and NanoSIMS image of an enriched cable bacteria filament which was analyzed in this project.

Reviewers:
Prof. dr. J.J. Middelburg
Dr. L. Polerecky
Daily Supervisor:
N.J.M. Geerlings

By:
K.S.As (5844886)
k.s.as@students.uu.nl

Universiteit Utrecht

Acknowledgments

The work presented in this master thesis project has come about by the effort and work of multiple people and institutions. With regards to funding, the work was almost entirely supported by the professor Olaf Schuiling fund. This project owes great gratitude to the fund and its beneficiaries, without whom the fundamental experimental work would have not been possible. First and foremost I would like to thank dr. Lubos Polerecky, who I contacted in December 2016 to find a microbiology-related subject to graduate on, and, who has guided and helped me tremendously throughout the project. On a daily basis I would like to thank my daily supervisor and lab buddy Nicole Geerlings, who has helped me greatly with the experimental work. Next to this I would also like to sincerely thank the second reviewer for reading and reviewing the here presented work: prof. dr. J.J. Middelburg. Aside from the persons directly involved in the project, I would also like to thank all the people within the GML building who created a pleasant atmosphere to work in. I will remember many nice experiences here.

Abstract

Cable bacteria are filamentous chemo-litho-trophic bacteria that live in diffusion-dominated seasonally, anoxic sediments. They become active after transition to oxic overlying waters has taken place. Cable bacteria oxidize sulfide with oxygen and thereby deplete the upper sediment layer of porewater sulfide. This creates a gap (10-30 mm) between the oxic and euxinic zone. In between, there is a suboxic zone, in which no sulfide can be measured, because sulfide, produced from sulfate reduction and released by FeS-dissolution, is efficiently consumed by cable bacteria in a cryptic sulfur cycle. Electrons produced in the euxinic and suboxic zone are conducted by the cable bacteria filaments to the oxic zone, where oxygen reduction takes place. Within coarse lines, the metabolism of cable bacteria has been depicted. But multiple questions still remain regarding the extent of sulfide oxidation cable bacteria are able to perform, and, also, the carbon metabolism of cable bacteria has been so far under investigated. To investigate sulfide metabolism, a new experimental method was investigated that would allow to measure sulfide consumption rate within the suboxic zone. The method relies on breaking the suboxic cryptic sulfur cycle by exerting anoxic conditions. This eliminates sulfide consumption by cable bacteria, leading to sulfide-release within the porewater. This could then be measured using micro-sensors. Using this method, a suboxic consumption rate of 1.3 $mmol*m^{-2}*d^{-1}$, was determined to occur within oxically incubated Rattekaai sediment. Validation of the new method still has to be performed to ascertain accuracy of the obtained values. To investigate carbon metabolism, ^{13}C-DIC and ^{15}N-NH_4 stable-isotope-enrichment was performed of cable bacteria, residing in oxically-incubated Rattekaai sediment. The biomass ^{13}C and ^{15}N fractional abundances were subsequently analysed using NanoSIMS. The main observation made in the investigation of carbon metabolism was that ^{13}C-DIC was exclusively taken up by cells that resided within the suboxic zone. Thus, the oxic zone cells seemed to have a differential function compared to the suboxic zone cells. This suggested that oxic cells, merely served to reduce the oxygen using the electrons conducted by the filament. These observations, serve as the first example of cells having a differential function within a cable bacteria filament. Also, a surprisingly homogenous uptake was observed within a filament, suggestive of a mechanism that actively or passively allows for sharing of available reduction potential. Based on these findings, cells might truly function within the context of the filament rather than being electron-conducting links in the chain. In the future, using the new sulfide consumption rate measurement method, as well as stable-isotope labelling with organic carbon and DIC, a highly complete picture of combined carbon and sulfide metabolism can be established.

Table of Contents pg.

1. Introduction

Coastal waters form a very important part of the oceanic system. These parts of the ocean are closest to mankind. Changes in these oceanic systems will influence humans most directly and they will vice versa be most directly affected by us. What these future effects will entail remains uncertain and could surprise us. Recently it has come to the fore that apart from the coastal systems themselves, even our view on coastal geochemistry can still be shaken up.

A relatively new discovered part of the coastal geochemical system will be treated in this master thesis: the cable bacteria (genus: *Desulfobulbaceae*, genera: candidatus electrothrix/ candidatus electronema).[1] A lot remains to be discovered about these organisms, including their true impact and importance but great strides have already been taken in recent years to uncover their role in sedimentary geochemistry. The upcoming sections deal with the recent findings on cable bacterial metabolism and its impact on the mineralogy and geochemistry of coastal sediments, to appreciate their importance in a broader sense. In the final sections we will revisit cable bacterial metabolism in depth and discuss the aims of the project.

1.1 Discovery of cable bacteria and metabolism

In 2012 a major concept has been introduced in the world of sedimentary geochemistry by the discovery of cable bacteria.[2,3] Before the discovery of cable bacteria, the main sedimentary geochemical concept had always been that oxidation and reduction processes require close proximity of reduced and oxidized species, leading to the redox cascade.[4,5] When cable bacteria are active they spatially separate coupled oxidation and reduction processes over multiple centimeters distance.[3]

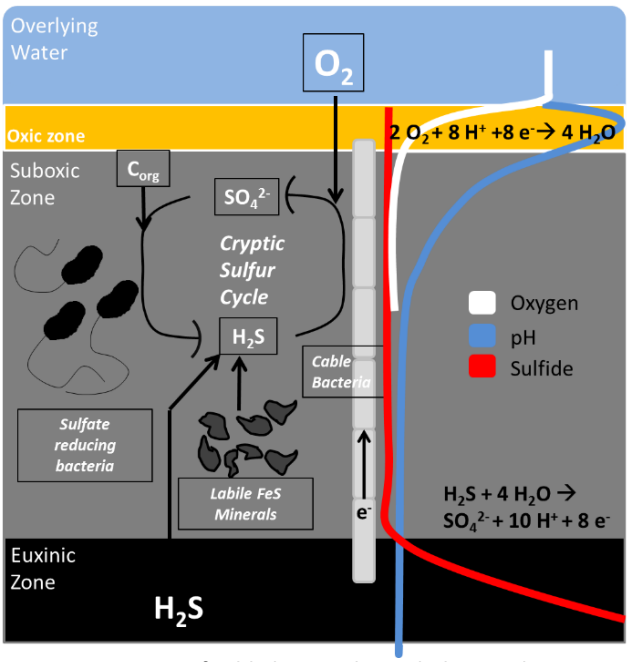

Figure 1. Overview of cable bacterial metabolism and its impact on oxygen, pH and sulfide depth profiles. *On the left side of the picture the sources of sulfide are summarized and on the right side an overview is given of the altered geochemical depth profiles.*

Cable bacteria thrive in non-bioperturbed sulfidic sediments with overlying oxygen-rich waters. They use sulfide as an electron-donor and oxygen or, more unlikely, nitrate, as the electron acceptor.[2,6] In doing so, porewater sulfide in the upper sediment layer is swiftly consumed and a growing spatial separation is created between the sulfide front and the oxic zone.

The cable bacterial cells divide and form a filament which is assumed to grow proportionally with the sulfide-oxygen gap, called the suboxic zone (figure 1). The filament facilitates the transfer of electrons within and across the suboxic zone. In this way electrons produced within the sediment by cathodic sulfide oxidation ($H_2S + 4\ H_2O \rightarrow SO_4^{2-} + 10\ H^+ + 8\ e^-$) can be used in the oxic zone in anodic oxygen reduction ($O_2 + 8\ H^+ + 8\ e^- \rightarrow 4\ H_2O$).

The transfer of electrons creates an electric circuit in the sediment which is closed by an induced counter-flux of porewater ions.[7,8] In order to distinguish it from regular sulfide oxidation this process is generally called electrogenic sulfur oxidation (e-Sox).

The individual half reactions are now separated in space and the protons involved in the redox reaction are no longer balanced at the same location, creating local extremes in pH. In this way, in the oxic zone a pH-peak (pH>8.4) was induced and in the suboxic zone a deep valley (pH<6.5). This leads to a characteristic pH-depth profile which serves as the main indicator of e-Sox activity (figure 1).[2,3,9] The creation of the suboxic zone gives cable bacteria the advantage of being the only specie able to employ oxygen to oxidize sulfide. In this way they can gain the largest biochemically possible amount of energy from sulfide oxidation. Interestingly, in incubation experiments a rather narrow range of maximum suboxic zone length and, likely, filament lengths were found, in the order of 15-30 mm.[10–12] It is not yet fully understood why there seems to be such a strict maximum size.

1.2 Impact of e-Sox on sedimentary geochemistry

The pH-decrease has a major impact on sedimentary geochemistry, because the present acid-sensitive minerals are greatly mobilized within the sediment.[10] Dissolution will most likely involve calcium carbonates ($CaCO_3$) and iron mono-sulfides (Mackinawite/Pyrrhotite or generalizing: FeS).[10,13]

Upon dissolution, the mentioned minerals are released as ions into the porewater. These cations are majorly drawn to the cathodic oxic zone. In this oxygen-rich and alkaline environment ferrous iron (Fe^{2+}) is efficiently oxidized to ferric iron (Fe^{3+}) and precipitates in the form of iron oxides.[14] The mobilized calcium and carbonate undergo a similar fate and precipitate as $CaCO_3$ in the alkaline environment of the oxic zone. Although, calcite precipitation is an acidifying process, the oxic zone of electrified sediment generally exhibited a pH-peak near the sediment-water-interface (SWI). Electrified sediments have the net effect of increasing the alkalinity of the overlying water because proton fixation outweighs the other acidifying processes.[19] With increased acidification of coastal oceans due to carbon emissions this could prove to be a positive effect on the alkalinity of coastal waters.[5]

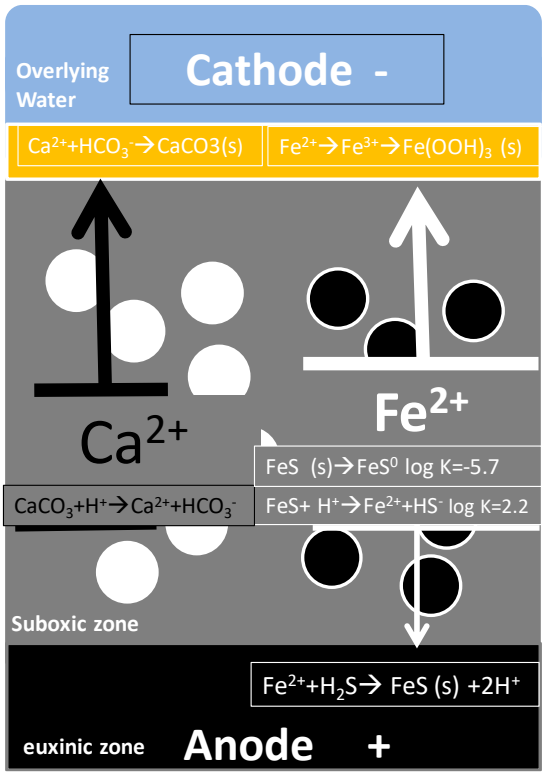

Figure 2. Overview of mobilization and precipitation reactions with Fe^{2+} and Ca^{2+} in electrified sediments.

Precipitation of iron oxides at the SWI was observed to have a rather indirect beneficial effect for anoxic marine systems. When cable bacteria are active there is a build-up of the iron oxide and carbonate top-layer crust. After anoxia sets in e-Sox ceases and sulfide is no longer consumed. The sulfide front will take over the suboxic zone once more and can creep up to the sediment-water interface. During this time there is a risk that sulfide is released in the bottom waters, with severe damage to the health of marine organisms. This could easily occur as oxidants that could neutralize sulfide are depleted under anoxic conditions.[5]

In the marine lake Grevelingen the crust of iron oxides, built up by cable bacteria, was able to take over the job of oxidizing sulfide. In this way, toxic sulfide leaks were delayed for a month.[15,16]

Cable bacteria can also exert influence over the sediment`s release and uptake of molecules. The main mediator in this process are the iron oxides, which associate with molecules such as phosphate, arsenate and other trace elements.[17] For instance, phosphate in the overlying water was bound to iron oxides at the SWI when cable bacteria were active. Once waters became anoxic, reduction of the iron oxides will lead to a release of phosphate.[18] In this way cable bacteria can influence the timing of uptake and release of these molecules. These molecules are usually present in small quantities but their importance for biology is often great. Knowing the above, cable bacteria could even prove to be of importance (negatively or positively) for human health because they have recently been found in aquifer sediments.[19]

Cable bacteria have now been found in marine and fresh waters all over the world.[20–22] In spite of this their true global impact on coastal sedimentary geochemistry still has to be fully established.

1.3 Sulfide sources and cryptic cycling

Now that effects on sedimentary geochemistry have been discussed, sulfide metabolism of cable bacteria will be treated. For cable bacteria there are three main sources of sulfide available in reduced sediments: 1) sulfide diffusing from the euxinic zone, 2) sulfide released by dissolution of FeS minerals and 3) sulfide produced by microbial sulfate reduction within the sediment.[10]

Depending on the sedimentary make-up dissolution of FeS was observed to frequently be the largest source of sulfide available to cable bacteria.[10,11] In some sediments dissolution of FeS-minerals can account for up to 95% of the sulfide consumed by cable bacteria. Consequently, growth and demise of cable bacterial activity was previously observed to be closely linked to dissolution and depletion of this FeS-storage.[11]

Another major source of sulfide originates from mostly delta-proteobacteria that use sulfate to oxidize organic matter.[12,23]As an end product oxidized organic matter and sulfide is obtained, which can be used by cable bacteria. In incubation experiments this source usually contributes less to sulfide consumption than FeS dissolution but is much larger than that of diffusion.[10,24] Although the above described processes both occur in the suboxic zone there is no measurable sulfide in the porewater. Cable bacteria exhibit a high affinity for sulfide and efficiently consume all produced sulfide. The suboxic zone in electrified sediment, therefore, has all the characteristics of a cryptic sulfur cycle.[25,26]

In cable bacteria research, major attention has been given to mass balances of most elements. A lot of knowledge is available about the cycling of elements within electrified sediment but the exact organisms, driving the cycle are not yet fully resolved.[10,24] In a major paper on metabolism it was found that correlated to e-Sox there was a strong surrounding chemo-litho-autotrophic community (genus: gamma proteobacteria), consisting of mainly sulfur oxidizing genera.[12,27] On the basis of this it was hypothesized that cable bacteria are not capable of fully oxidizing sulfide by themselves but require the associated chemo-litho-autotrophic community to complete the oxidation.

The hypothesis of a thriving chemo-litho-autotrophic community next to e-Sox was fueled further by net consumption of a sedimentary elemental sulfur pool when cable bacteria became active.[24,28] A problem remains because there is no obvious candidate molecular specie in the suboxic zone that could serve as an oxidant. To address this it has been suggested that either sulfur disproportionation is occurring ($S^0 + H_2O \rightarrow 3/4\ HS^- + 1/4\ SO_4^{2-} + 5/4\ H^+$) or, as a more exotic explanation, excess electrons from sulfur oxidation could be disposed of via nano-wires which are connected to the filament of the cable bacteria.[12,28] Such an explanation has actually become less exotic as more research suggests that nano-wire-genes are genetically encoded in a wide variety of different genera.[29] Still, a lot of the earliest research assumed cable bacteria would be able to fully oxidize sulfide, and, mass balance calculations were performed using this assumption.[10] It remains uncertain what occurs in sulfide metabolism and how it influences the energy budget of cable bacteria.

1.4 Sulfide oxidation of cable bacteria

Whether or not cable bacteria are able to fully oxidize sulfide might seem trivial at first, as long as the cryptic sulfur cycle is closed. But the energy released by e-Sox could be directly affected by whether or not cable bacteria are able to fully oxidize sulfide. If we look at incomplete oxidation (1: $HS^- + H^+ + ½\ O_2 \rightarrow S^0 + H_2O$[30]) only two electrons are released. In the case of complete oxidation this amount would involve six more electrons (2: $S^0 + 1½\ O_2 + H_2O \rightarrow SO_4^{2-} + 2\ H^+$ [30]). It seems likely that the energetic gain for cable bacteria would be different if a microbial community was required to complete oxidation.

A complicating factor in the analysis of sulfide metabolism is that a cryptic sulfur cycle takes place within the suboxic zone. Turnover of the consumed species cannot be directly measured, and, most studies determine sulfide consumption by first calculating proton consumption on the basis of the oxic zone pH-peak. This is then used to calculate the corresponding anodic sulfide oxidation, using the assumed stoichiometric ratio between sulfide and protons (figure 1).[2,31] Other more direct methods calculate sulfide consumption by employing SO_4^{2-}- and Fe^{2+}-depth profiles and sulfate reduction rate measurements.[10,24,28] In the end, only one study has measured both sulfide and proton consumption simultaneously using independent methods.[10]

1.5 Growth and carbon metabolism of cable bacteria

Sulfide oxidation is among the most energetically favorable lithotrophic reactions. But, still, under standard conditions it is not possible to directly reduce NAD^+ via this reaction.[30] Surprisingly, in laboratory incubation experiments, cable bacteria had a rather fast growth rate (doubling time= 20 h). This suggests that carbon uptake was efficient, and, this suggestion would then extend to the mechanism of electron transport.[11,12]As this observation contrasts with the consensus idea that carbon fixation by autotrophic sulfide oxidizers is a slow process. Cable bacteria would then most likely be mixotrophs, meaning they use organic (reduced) carbon as c-source but not to create reduction potential.[11,27,30]

Research into the carbon metabolism of cable bacteria has not been extensive but in the only research directly addressing this subject, a strong preferential uptake of ^{13}C-propionate (5x more) over ^{13}C-DIC was observed.[12] The small uptake of ^{13}C-DIC was ascribed to anapleurotic reactions that serve to replenish depleted pools of metabolic intermediates. Other more circumstantial evidence for mixotrophy comes from the fact that many of the closest cultivated relatives in Desulfobulbus spp. are organotrophs.[32,33] Interestingly, it was observed that the oxic zone cells were taking up ^{13}C faster than the sulfide anodic cells. This suggests there is a difference in production of reducing equivalents in different parts of the filament. In the paper it is suggested that this would be a consequence of differential energetic yield of the two half reactions. These observation do however require further substantiation because, as said, just one experiment directed at carbon metabolism has been performed.

1.6 Experimental aims

In this study, both carbon metabolism and the sulfide metabolism of cable bacteria will be investigated, albeit by different experimental approaches.

As mentioned above, measuring sulfide consumption of cable bacteria was hard, because for a large part it is hidden within a cryptic sulfur cycle. In this study a new method will presented that would allow to directly measure the suboxic sulfide consumption. The mechanistic idea is based on disrupting the cryptic sulfur cycle, which will be performed by removing the oxygen in the overlying water. Thereby, cable bacteria will now longer be able to oxidize sulfide and the previously consumed sulfide will now instead be released into the porewater. This can then be measured as increased H_2S-concentration using micro-sensors. The rate of increase would then be similar to the consumption rate of cable bacteria. In this way consumption rates can be measured at multiple depths within the suboxic zone and a consumption depth profile can be constructed. This new method, just as in the pH-peak method does not require slicing of the core. Also accuracy of sulfide determination could be increased because no metabolic assumptions have to be made on the relation between proton and sulfide consumption. Furthermore, combined with the pH-peak method, the proton consumption and sulfide oxidation can be independently measured. This could, in the future, possibly shed light on the extent of sulfide oxidation in the suboxic zone. **In this master thesis project the first preliminary experiments and results using the new sulfide consumption rate measurement method will be presented.**

Next to sulfide metabolism also carbon metabolism of cable bacteria will be investigated. This was of importance because there has been just one experimental study on this subject. Based on this one study, the state of the art is that the cable bacteria prefer reduced organic carbon over inorganic carbon. Also, within the filament a two-fold higher carbon assimilation-rate was observed in the anodic oxic-zone cells.[11,12] **More studies into carbon metabolism are required because developmental stage of the population and the sedimentary composition might be factors of importance in the obtained experimental results. Here we will add to this subject matter by performing a stable-isotope-labelling experiment, using ^{13}C-DIC and ^{15}N-NH_4. This allows carbon assimilation rates and differential uptake patterns within the filament to be analysed using NanoSIMS.**

2. Materials and Methods

2.1 Original location of reduced sediment and its properties

For now it remains impossible to grow pure cultures of cable bacteria, so, in order to obtain cable bacteria for our research, suitable reduced sediment was collected from the *Rattekaai* salt marsh in Zeeland, the Netherlands (figure 3, coordinates: 51.4391°N, 4.1697°E). At this location vast amounts of organic material are deposited and there is a tidal influx of seawaters; this combination allows for high rates of sulfate reduction and ultimately creates highly sulfidised sediment.[34–36] Collection of raw sediment material took place in summer 2016 and was immediately stored at 6 ^{0}C in a closed and dark container. When required for experimental procedures, the sediment was taken out and sieved using a pore size of 500 µm before further handling (Analysensieb 200 mm* 25 mm, Haan, Germany).

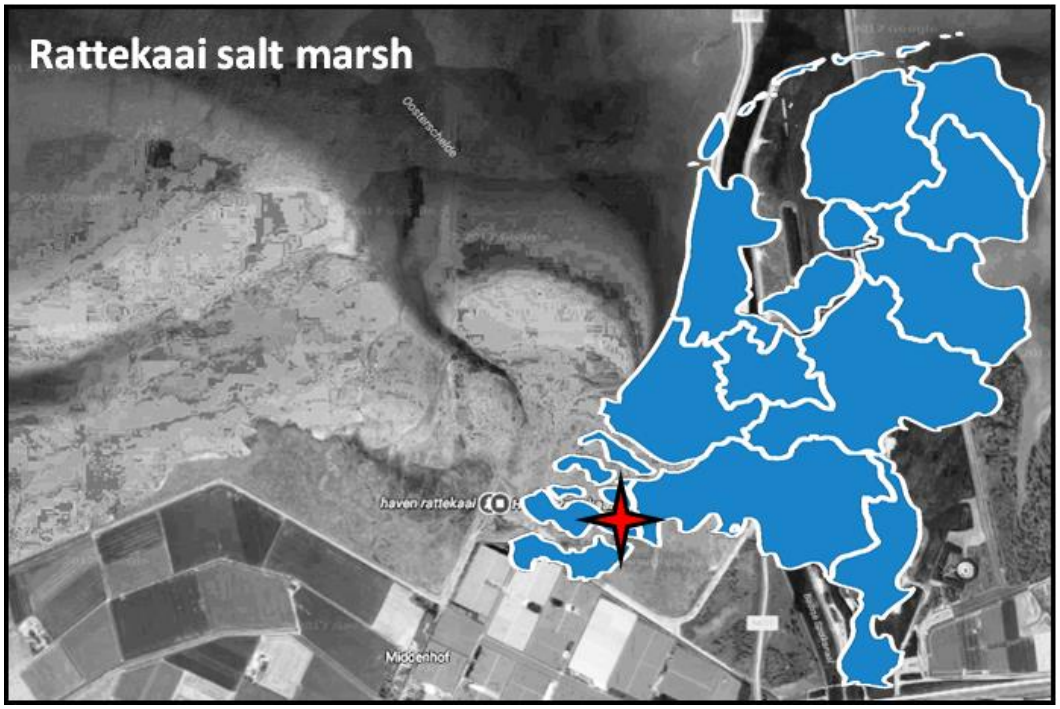

Figure 3. Satellite view of the Rattekaai salt marsh (taken from google maps) and location of the site within the Netherlands (indicated by the star).

2.2 Determination of porosity and organic matter content

Sieved sediment was brought into pre-weighted and volumetrically accurate 24-ml-syringes (Terumo Europe NV, Leuven). Then the syringes were weighed again on a Mettler Toledo XP504 balance (Mettler, Tiel, the Netherlands). To remove the water fraction, the sediment was put on a pre-weighted metal platter, weighed once more, and subjected to a heat treatment of 60 ^{0}C for 48 hours using a Memmert UF55 oven (Memmert, Schwabach, Germany).[34,37] The platters were weighed again and liquid volume was assumed to be equal to $V_{liq}=\frac{Wet\ weight-dry\ weight}{density\ of\ water}=\frac{Mwet-Mdry}{\rho(water)}$. Porosity of the sediment was then calculated as the liquid volume compared to the total volume: $\phi=\frac{Vliq}{Vtotal}$.

Organic matter (OM) content analysis was performed by bringing the sediment`s temperature up to 430 ^{0}C for 2 hours in a Heraeus M110 oven (Thermo Scientific, Landsmeer, the Netherlands). In this so-called loss on ignition approach, all organics are supposed to be combusted leaving solely mineral particles. OM content can then be given in a weight to weight ratio.

2.3 Oxic incubation set-up of sediment cores

Sieved sediments were transferred into polycarbonate incubation cylinders (cores) with dimensions of 10 cm x 4 cm. At the bottom of the core was a removable stub and at the top usually some space was free of sediment, reducing the volume effectively occupied by the sediment. Cores filled with sediment were left to settle for one day prior to being transferred to the incubation container. The incubation contained was filled with artificial seawater (ASW) with a salinity of 32 ppt, which was prepared using a commercial sea salt mixture (Instant Ocean Spectrum Brands, Blacksburg, Virginia, United States). Here cores were kept entirely submerged in ASW, while being aerated using air pumps (prosilent a50, JBL Neuhofen, Germany). To prevent possible growth of algae, which could alter the chemical composition of the seawater, the container`s non-translucent lid was kept closed as much as possible.

2.4 Micro-profile analysis of incubated cores

To monitor establishment and the development of cable bacterial populations, micro-sensor depth profiles were taken of the incubation cores at regular time intervals. Parameters and chemical species that were investigated were pH, H_2S and O_2. All micro-sensors were supplied by Unisense (Unisense A/S, Aarhus, Denmark) and attached to the motorized 1D profiling system from the same manufacturer, allowing for accurate depth control over the sensors. Micro-sensors were coupled to data signal acquisition electronics. Its signal was recorded into the Sensortrace pro software, also by Unisense, from which excel spread sheets were exported for further processing.

2.4.1 Calibration of micro-sensors

H_2S

Na_2S•9 H_2O-crystals were washed to remove the oxidized outer sulfide crystals and subsequently dissolved into anoxic waters to a concentration of 0.01 M. This solution was kept in the glove box` anoxic environment and was taken out in small gas tight injection vials just before calibration was performed. The stock solution was brought into anoxic ASW preventing oxidation of dissolved H_2S. pH of ASW had been brought down to pH 3 by titration with 32% HCl, to fully protonate all present $H_{(x)}S$-species (pKa_1=7.05), as the micro-sensor can solely measure H_2S and not deprotonated forms. Using a gas-tight 100-µl-syringe **(**Hamilton Robotics, Bonaduz Switzerland), several H_2S-concentrations were prepared in the acidified anoxic ASW to construct a calibration curve. The H_2S micro-sensor had an outer-tip diameter of 100 µm.

pH

pH was prepared using commercially available calibration standards (Orion™ ROSS™ All-in-One™ pH Buffer Kit, thermo scientific, Landsmeer, the Netherlands). Next to the pH micro-sensor a reference electrode was required to measure the pH-signal. For this we purchased the robust reference electrode with a tip of 5 mm. During measurement, the reference electrode was always brought into the overlying water (figure 4). The pH micro-electrode had an outer-tip diameter of 200 µm.

O_2

O_2 calibration was performed alongside the measurement of the core profile. Overlying water was always kept fully oxygenated using air pumps and the corresponding signal was set to be the theoretical 235 µM for seawater with salinity 32 ppt and at T=20 ^{0}C.[38] In the core pore water was fully anoxic and signal was set to correspond to 0 µM. The O_2 micro-electrode had a tip diameter of 50 µm, allowing for high depth resolution.

Overall set-up and operation procedures

In order to cause least alteration during measurement compared to the incubation environment, cores were put into fully oxygenated water during micro-profiling (figure 4). For this purpose a custom-made aquarium (15 cm* 10 cm * 8 cm) was constructed using a combination of polycarbonate and acrylate (Pyrasied, Leeuwarden, the Netherlands). To prevent floating of the core and resulting damage to the micro-sensors a core holder was constructed that stabilizes the core and weighs down the core holder using sand. To add to its stability the holder exactly locked itself between the two sides of the aquarium.

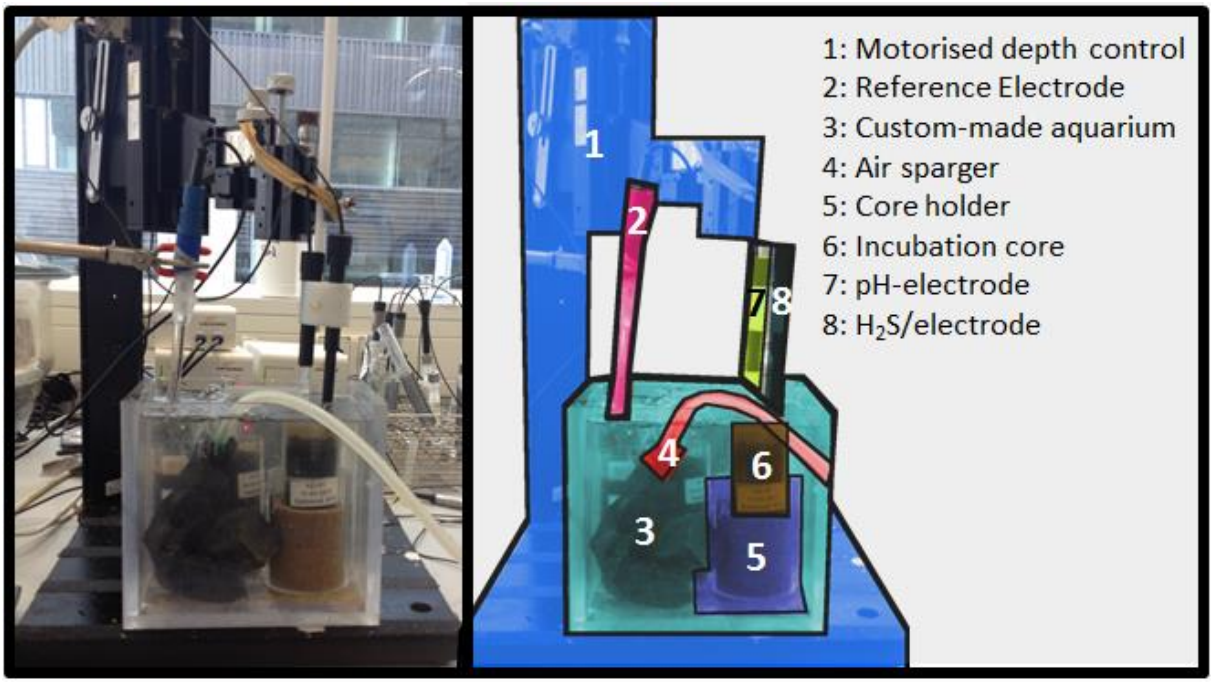

Figure 4. Micro-profile sensor set-up as used in the lab (left) and a schematic picture of the instruments that constitute the set-up (right).

Once in place, pH- and H_2S-profiles were measured simultaneously to also account for deprotonated forms of H_2S.[39] This was performed by employing the first acid dissociation constant of H_2S:

$$[\sum H_2S] = [HS^-] + H[_2S] = [H_2S] + \frac{[[H_2S]*Ka1}{[H^+]} \ (Ka_1=^{10\text{-}6.8})$$

A depth range was measured from 2 mm in the overlying water until 5 cm depth in the sediment core. As a step size, 150-250 µm was chosen until the length of the suboxic zone was accurately determined. After each step in depth a waiting period of 3 seconds ensued after which the subsequent signal over 5 seconds was averaged. Once the euxinic zone was reached, step size was increased up to 2 mm to make measurement of a large amount of cores more time-efficient.

O_2 measurement was performed with a depth range of 2 mm in the overlying water until 3 mm depth was reached. Waiting and measuring period both lasted 2 seconds. For O_2 profiling, step size was varied between 50-100 µm.

Calculation of fluxes from profiles

Fluxes were calculated using the 1D Fick`s diffusion law (1). For H_2S and O_2 we only performed diffusion calculations outside the suboxic zone. Fluxes of these species will therefore not be affected by the electric field. For Fe^{2+} which has a charge and a flux within the suboxic zone, where electrostatic potential was present, an extra term was added to the 1D Fick`s law (2).[10]

$$J_{H2S/O2}=\text{-Dsed}*(\frac{dC}{dz}) \quad (1)$$

$$J_{Fe2+}=\text{-Dsed}*[(\frac{dC}{dz}+/-.\frac{nF}{RT} * C * \frac{d\psi}{dz})] \quad (2)$$

Diffusion coefficients were taken from Boudreau 1996 and adjusted for T=20 ^{0}C and Salinity =32, using the marelac package.[40,41] The obtained diffusion coefficients were adjusted for porosity of the sediment using formula (3)[28]:

$$Dsed = \frac{D0*\varphi}{1-2*\ln(\varphi\ )} \quad (3)$$

A more elaborate calculation is given in appendix V.

2.5 Determination of Fe^{2+} and NH_4 depth profiles

To determine Fe^{2+}- and NH_4-depth profiles, the cores were sacrificed and sliced in 2 to 5 mm thick slices inside the anoxic environment of a glove bag (Sekuroka, Carl Roth, Karlsruhe, Germany). Porewater and sediment for each slice were separated by centrifuging at 3000 rpm for 10 minutes on a SL40 R table top centrifuge (Thermo Scientific, Landsmeer, the Netherlands). The supernatant was taken off and filtered over 0.45 µm pore size filters (Advanced Microdevices Pvt. Ltd**,** Ambala Cantt, India) before further analysis was performed.

Fe^{2+} concentration of the porewater was determined colorimetrically using the ferrozine method.[42,43] A calibration line was constructed by creating multiple concentrations of $NH_3Fe(II)SO_4 \bullet 7\ H_2O$ from a stock solution (Sigma-Aldrich, Zwijndrecht, the Netherlands). To limit occurrence of Fe^{2+}-oxidation, the salt was dissolved into a 0.1 M HCl solution. Fe^{2+} to ferrozine complexation is very fast, so, after adding the porewater sample/Fe^{2+}-solution absorption could immediately be recorded. Absorption was determined at a wavelength of 562 nm on a Shimadzu UV-1800 spectrophotometer (Shimadzu Benelux, s-Hertogenbosch, the Netherlands).

To determine NH_4-concentrations the colorimetric indophenol blue method was used.[44,45] Maximum and stable yield for this reaction is obtained between pH 10.5-11.5, making pH control extremely important.[45] Thus, in order to create a calibration line at a comparable pH, NH_4 was dissolved into ASW, which would have a similar buffering capacity as the porewater samples. To ascertain pH was indeed similar for the samples and the calibration line, pH was measured after the absorption measurement using a Consort C830 pH-meter (Consort, Turnhout, Belgium).

Starting from a NH_4Cl stock solution, multiple NH_4-concentrations were prepared to construct the calibration curve. To limit inaccuracies due to ammonia outgassing, stock solutions for the calibration curve were always prepared just prior to sample preparation. Reaction was incubated for 4 hours before the absorption measurement at 630 nm took place on the same photo spectrometer as above. Porewater samples were handled anoxically to prevent oxidation of dissolved Fe^{2+}-ions.

Example calibration lines can be viewed in appendix III.

2.6 Isolation, washing and observation of cable bacteria

Cable bacteria were isolated from the surrounding sediment using glass hooks under a Zeiss Stereo Discovery V8 light microscope (Carl Zeiss, Jena, Germany). After isolation the filaments were washed multiple times in miliQ droplets to remove salts. Next the filaments were deposited onto carbon adhesive discs (Agar scientific, Stansted, United Kingdom), mounted onto a 12.5 mm*8 mm SEM stub (Agar scientific, Stansted, United Kingdom). Filaments could now be observed on the benchtop scanning electron microscope (SEM) (JCM-6000PLUS NeoScope, JEOL, Peabody, Massachusetts, United States). The SEM was set to function under 0.1-0.3 mbar high-vacuum conditions with an electron accelerating voltage of 15 kV.

2.7 Analysis of metabolic activity using isotopically-labeled nutrients

To investigate the metabolic activity of cable bacteria the porewater was enriched with ^{13}C-DIC and ^{15}N-NH_4. A stock solution was prepared containing 62 mM of a ≥98 atom % C-enriched $NaH^{13}CO_3$ and 0.35 mM of ≥98 atom % N-enriched $^{15}NH_4Cl$ (Sigma-Aldrich, Zwijndrecht, the Netherlands). In order to avoid $Mg^{13}CO_3$/$Ca^{13}CO_3$-precipitation and minimize disturbance to the core`s pH and ionic composition, these compounds were dissolved in an altered seawater recipe that contained solely SO_4^{2-}, Na^+, K^+, Cl^-, Sr^+ and Br^-ions (appendix X). The artificial sea water was bubbled with N_2 to remove all dissolved oxygen. The prepared solution had a pH of 6.15 which is comparable to pH-values regularly found in the suboxic zone.

500 µl of the enriched solution was injected into the core by 10 50-µl-injections into a circular area with a 1 cm diameter. In order to create a homogeneous spread of enrichment, the filled needle was first inserted up to 5 cm depth. Then, while moving upwards the liquid was released evenly up to the water-sediment interface. After this, the core was left to stand in the dark without overlying water for an incubation period of 24 hours. The next day a subcore was taken at the injection area, from which filaments were isolated. The subcore was divided into the suboxic and oxic zone, as determined from micro-profiling. These were then searched separately for cable bacterial filaments, using the previously described protocols. Duplicates for filaments from both zones were prepared.

For both zones, a portion of filaments was incubated for 15 minutes in a 1% SDS and 1 mM EDTA to the leave the outer electron-conducting structure. Treated and isolated filaments were deposited on a 0.2 µM filter (Merck Millipore, Amsterdam, the Netherlands) pre-coated with a 10 nm-thick gold layer. The filter was subsequently deposited on a custom-made holder suitable for both SEM and the Nanoscale secondary ion mass spectrometer (NanoSIMS) 50L (Cameca, Paris, France).

2.8 Stable isotopic enrichment and Nanoscale secondary ion mass-spectrometry (NanoSIMS)

Field of view in NanoSIMS was set in-between 40 µm*40 µm and 70 µm* 70 µm. All fields of view were pre-sputtered with Cs^+-ions to reach a stable secondary-ion signal. The primary Cs^+-ion beam (current 1–2 pA, energy 16 keV, focused to a nominal spot size of 130 nm) was applied with a dwelling time of 1 ms/pixel. Secondary-ion species released in this way were separated in the magnetic section of the mass detector. Simultaneous separation and detection of $^{14/15}$N and $^{12/13}$C species was performed.

Mass to signal tuning was performed daily before analysis, ensuring the quality of specie identification. Obtained data was processed using the Look@Nanosims (LANS) software.[46] For each separate plane signals were accumulated and carbon and nitrogen enrichment was calculated by dividing the isotopic signals: $\frac{^{13}C}{^{13}C + ^{12}C}$ and $\frac{^{12}C^{15}N}{^{12}C^{14}N + ^{12}C^{15}N}$. This was performed using the LANS-software.

Example of ROI definition and analyses

In figure 5, it is illustrated how the NanoSIMS images were divided into regions for which the enrichment values could be calculated. Starting from a mass signal field of view (figure 5A), the regions of interest (ROIs) were drawn as in figure 5B, which corresponded to either part of a filament or individual cells. The signal for the specified areas and species was averaged. Enrichment within a ROI was calculated as the fractional abundances of ^{13}C and ^{15}N ($\frac{^{13}C}{^{13}C + ^{12}C}$ and $\frac{^{12}C^{15}N}{^{12}C^{14}N + ^{12}C^{15}N}$). Thus, quantitative comparison between filaments and cells became possible.

Care was taken to prevent analyzing ROIs that showed highly variable signal-intensity over multiple measurement. Adjustment was made by either limiting the amount of planes included into the accumulation or removing the ROI all together.

Quantative overview of samples and measurements

From the oxic zone we collected in total 14 individual filaments of which 5 were SDS/EDTA-treated and analysed over 21 separate views. From the suboxic zone we collected 17 filaments of which 5 were SDS/EDTA-treated. These were analysed over 29 separate views (table 1).

Table 1. Overview of the samples that were analysed using the NanoSIMS method. *The measurements signify the amount of different locations for which enrichment of ^{13}C and ^{15}N was determined. The individual ROIs correspond to individual cells within the filament.*

DEPTH LAYER	SDS/EDTA-TREATED	MEASUREMENTS(#)	FILAMENTS (#)	INDIVIDUAL ROIS ANALYSED (#)
OXIC ZONE	Yes	3	5	53
OXIC ZONE	No	18	9	391
SUBOXIC ZONE	Yes	9	5	124
SUBOXIC ZONE	No	20	12	509

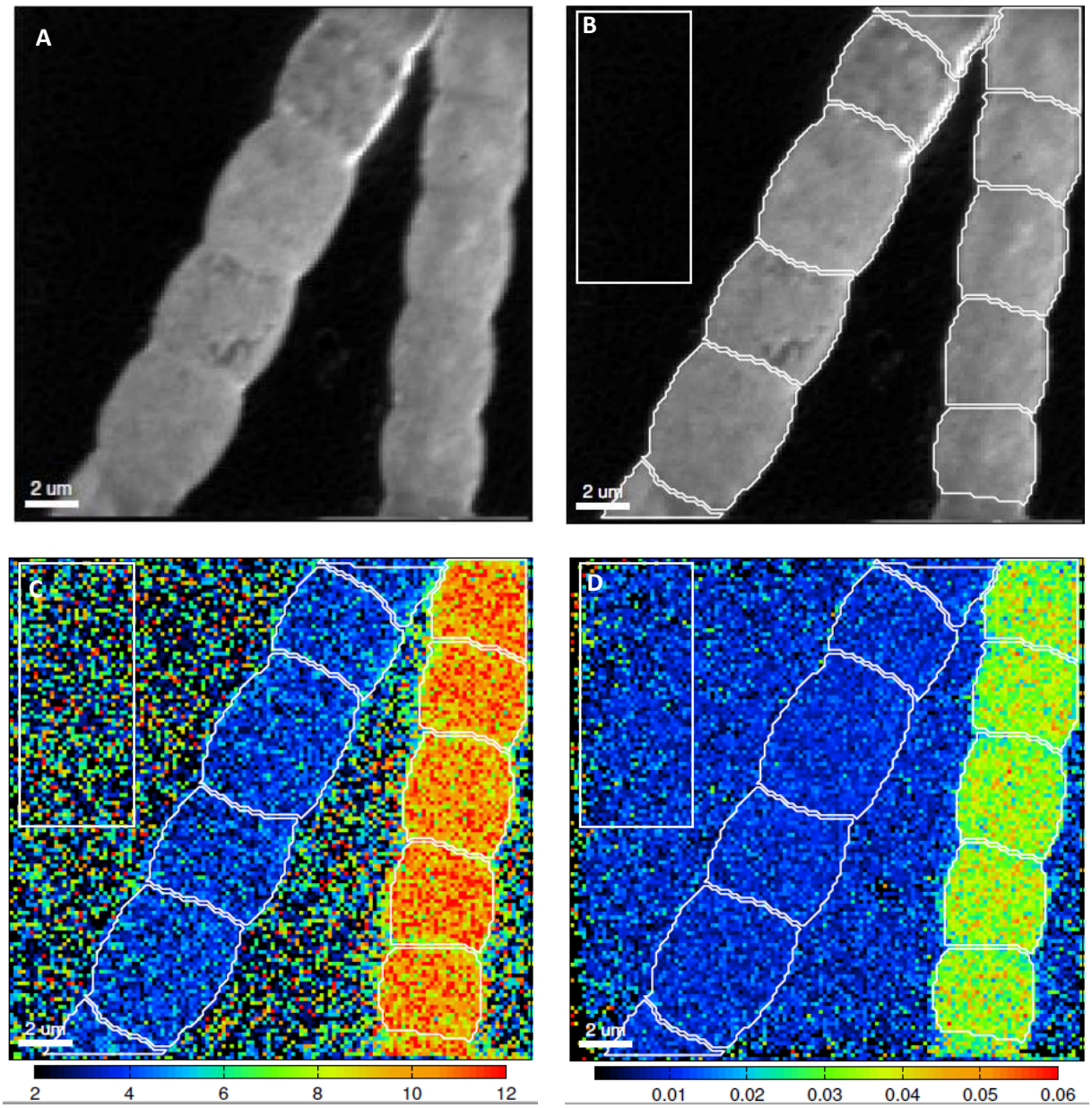

Figure 5. NanoSIMS images that illustrate ROI definition and enrichment results for one measurement. Panel A: $^{12}C^{14}N$ NanoSIMS image of part of the cable bacterial filament that will be analysed for stable isotope enrichment. Panel B: Image showing the ROIs to calculate enrichment within an area (white lines). *The square ROIs served to analyse the background enrichment signal.* **Panel C: ^{15}N-enrichment.** *Enrichment was calculated as a fractional abundance ($\frac{^{12}C^{15}N}{^{12}C^{14}N+^{12}C^{15}N}$). Scale bar was in units of *10^{-3}.* **Panel D: ^{13}C-enrichment**. *Enrichment was calculated as* $\frac{^{13}C}{^{13}C+^{12}C}$.

3. Results

3.1 Sediment characteristics

The sieved and homogenized Rattekaai sediment had a wet weight density of 1150 kg/m^3 and a porosity of 0.72±0.02. The organic matter (OM) content was determined to be 0.082±0.002 g OM/g dry sediment and 0.029±0.0008 g OM/g wet sediment. The obtained values were similar to what has been reported previously in literature for this location.[34,36]

3.2 Establishment of cable bacterial populations and development of micro-sensor depth profiles

3.2.1 Establishment of cable bacteria in incubated sediment

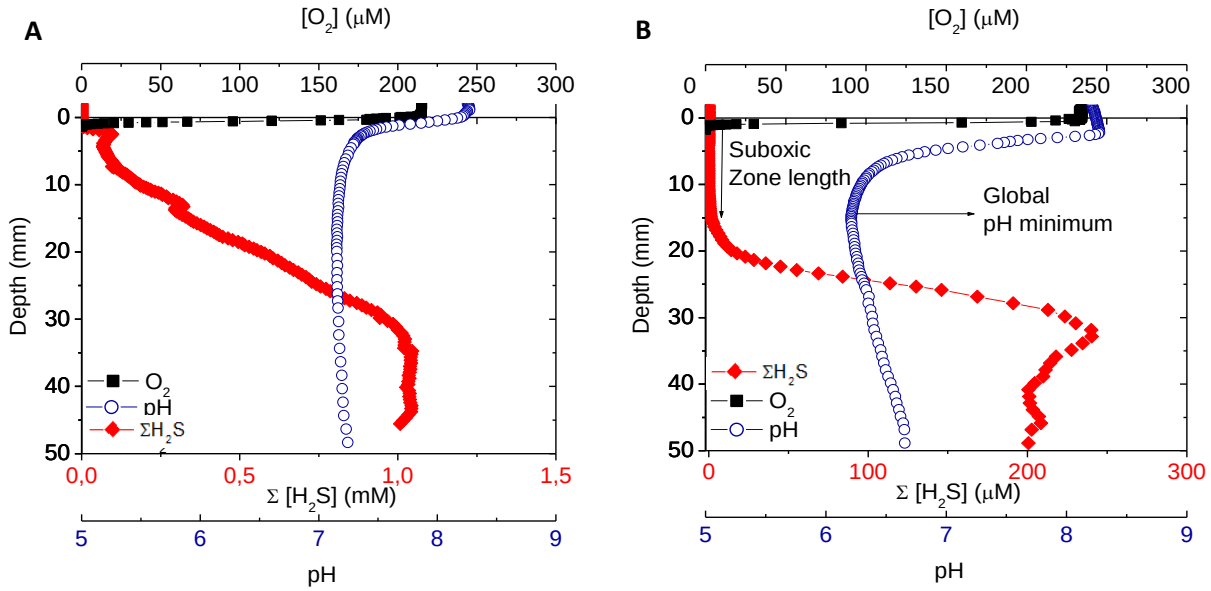

Figure 6. pH, O_2 and H_2S-profiles of oxic-incubated Rattekaai sediment Panel A: Incubated for 1 day. Panel B: Incubated for 21 days. *Notice the difference in unit for ΣH_2S between panel A and B.*

At the start of incubation, oxygen could be measured in the sediment until a depth of 2.5 mm (oxygen penetration depth) was reached. The sulfide appearance depth, defined as the depth at which sulfide concentrations exceed 1 µM, was 0.6 mm (figure 6A). In the depth range of 0.6 to 2.5 mm the concentration profiles of oxygen sulfide overlapped. In this zone sulfide is oxidized with oxygen to sulfate. Compared to the artificial sea water, the sediment was more acidic, decreasing from pH 8.4 to pH 7.1, deeper in the sediment.

During three weeks of incubation the geochemical profile gradually changed and started to resemble that shown in figure 6B. The oxygen penetration depth had decreased with 1 mm to 1.5 mm, indicating an increased oxygen consumption of the sediment. The sulfide appearance depth was found 12 mm deeper at 15 mm; now the oxygen and sulfide profiles no longer overlapped. Also the pH in the sediment was strongly decreased after three weeks of incubation, from a global pH minimum of 7.1 to pH 6. The decrease in pH and the formation of the suboxic zone served as the primary geochemical characteristics of the establishment of a cable bacterial population.

The establishment of the profile as in figure 6B served as the main indicator that cable bacteria were present in the sediment. For stronger support, cable bacteria were isolated using glass hooks under a light microscope. Using a SEM microscope the morphology of isolated filaments was checked to be similar to that of cable bacteria (figure 7).

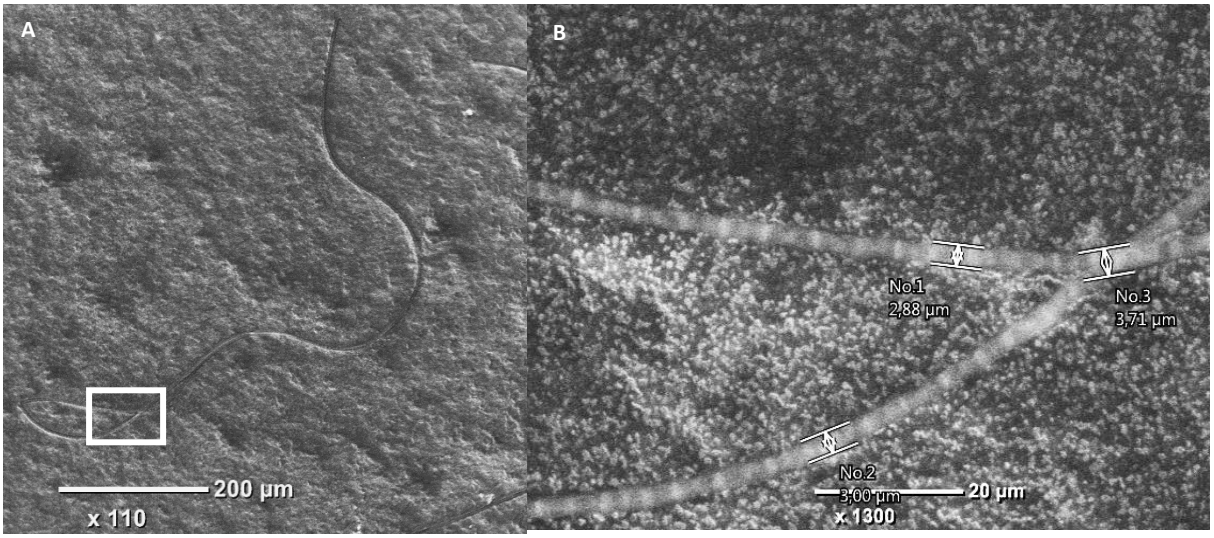

Figure 7. Cable bacterial filament as viewed under the SEM microscope. Panel A: Overview of the filament. Panel B: Zoom in of square. *The cable bacteria are the long "banded" strings.*

3.2.2 Changing of geochemical profiles induced by cable bacteria

3.2.2.1 Indicators of cable bacterial activity and lateral heterogeneity

To monitor development of the cable bacterial populations, global pH minimum and the length of the suboxic zone in the micro-sensor profiles were used as indicators (figure 6). pH would be an indicator of activity because cable bacteria produce protons when oxidizing sulfide. Suboxic zone length would serve as an indicator for cable bacterial length at that point in time. Because over long periods of time, measurement at the exact same location would prove too meticulous, the lateral heterogeneity of these indicators in our cores was investigated (figure 8).

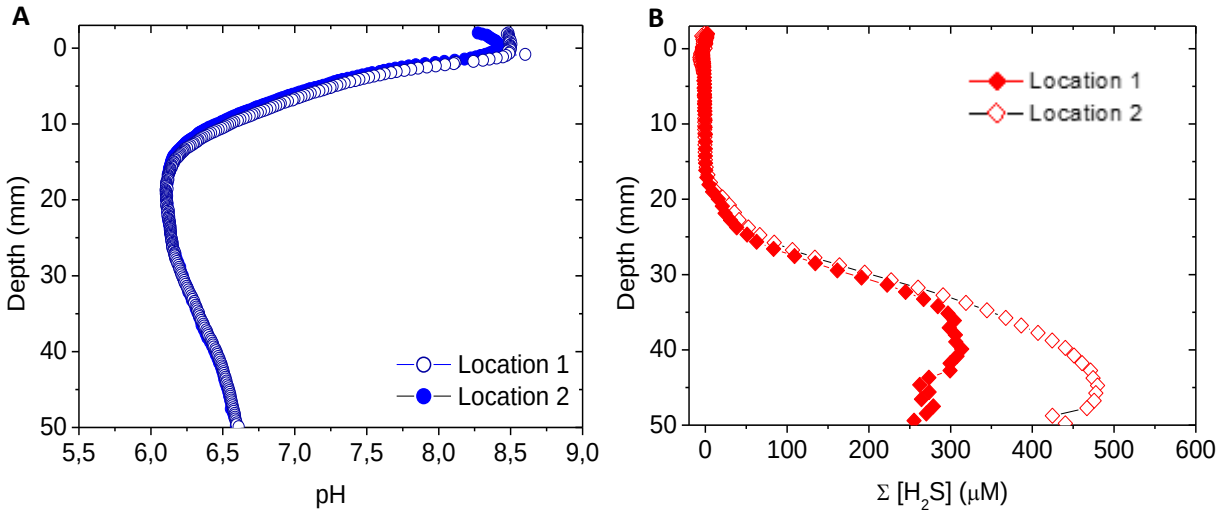

Figure 8. micro-sensor depth profiles at two distinct location within one core to investigate lateral heterogeneity. Panel A: pH-profile measured at two distinct location in one core. Panel B: H_2S depth profile at two distinct locations. *More lateral heterogeneity profiles can be found in appendix I.*

For the two laterally different measurements, the pH depth profile was nearly identical (figure 8A). IN both measurements the global pH minimum was around pH 6. The corresponding [ΣH_2S] profiles did exhibit the same sulfide appearance depth but within the euxinic zone the H_2S-levels started to exhibit some lateral heterogeneity (figure 8B). However, because solely the suboxic zone length was used for the monitoring of core development, this does not pose problems. Concluded was that the pH-minimum and location of the euxinic front serve as reliable activity indicators.

3.2.2.2 Development of activity indicators over time

Five cores were incubated and regularly profiled to monitor development over a 90 day period (figure 9). The five cores consisted of three groups which were incubated at different points in time: two couples (core 1 and 2; core 3 and 4) and one independent core (core 5). For all five cores there was a quick decrease in pH in the first 14 days of incubation. For cores 3 and 4 decrease continued, although less intensely, until day 45 (figure 9A and appendix II). After day 45, the global pH minimum for cores 3 and 4 started to increase but never returned to the original pH of 7.2 over the entire 90-day-period. In contrast to this, the global pH-minimum of core 1 and 2 immediately started to increase after reaching peak values on day 14, and, on day 50 the global pH-minimum had returned to a value of 6.8. Core 5, although being incubated at a different time point, behaved most similar to core 3 and 4.

For the length of the suboxic zone a similar but inverted pattern was observed (figure 9B and appendix III): again all cores exhibited a steep increase in the first 14 days after which core 3 and 4 showed again a more long lasting suboxic zone compared to core 1 and 2. Interestingly, cores, incubated at the same point in time, behaved rather similar whereas between the couples the behavior showed more disparity. This could be possibly due to heterogeneity in the stock sediment or alteration of the stock sediment during storage.

Based on the averages depicted in figure 9A and B and for ease of further writing, the following distinction in time periods during core development is proposed: 1) *rise*-period (day 0-14), 2) *plateau*-period (day 14-45) and 3) *demise*-period (day 45-90).

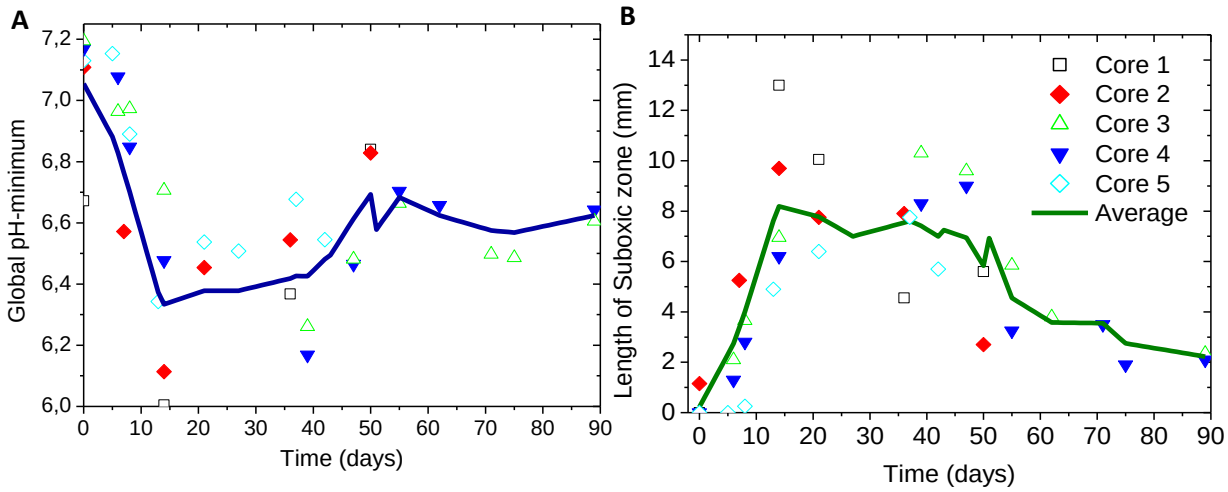

Figure 9. Development of the activity indicators for five independent cores over a 90 day period Panel A: Global pH-minimum development. *Global pH minimum was defined as the lowest pH in a full pH-profile.* **Panel B: suboxic zone length development** *Suboxic zone length was defined as: Oxygen penetration depth – sulfide appearance depth (where [ΣH₂S]=1 µM)). Continuous graphs for the individual cores were made by interpolation between the separate measurements . The continuous graphs were subsequently averaged for the relevant periods of time, here depicted by the line.*

3.2.2.3 Correlation between the development indicators

In figure 9 the indicators pH-minimum and length of the suboxic zone showed a similar development but inverted from one another. This suggested that pH and suboxic zone length were in some way coupled. To address this coupling, figure 10 was created in which the two indicators were correlated for the three proposed periods.

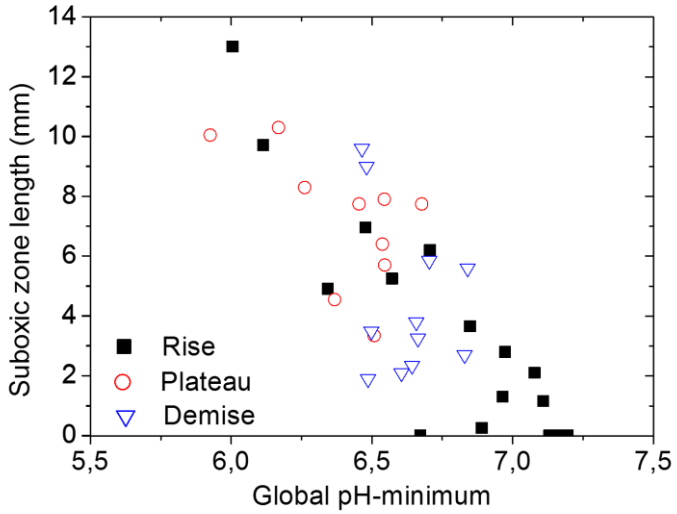

Figure 10. Correlation between the observed global pH minimum and the length of the suboxic zone. *The activity indicator values over time for all five core, as shown in figure 9***,** *were mapped in this graph.*

Figure 10 depicts the negative linear correlation between suboxic zone length and global pH minimum over all developmental periods. The coupling was not very tight when averaged over all periods (y=-8.78+63.02, R^2=0.66, using origin 6.1 fitting software). The correlation was most strongly present for the rise period (y=-9.19x+65.77,R^2=0.80). Although the *plateau*-data more or less followed the *rise*-correlation there was a decrease in the coefficient of determination (R^2) upon addition of these points (y=-8.94x + 64.20, R^2=0.78). For the *demise*-period, nothing resembling a correlation could be found (R^2 = 0.087). Coupling, therefore, only seemed to be a property of these parameters during phases of high activity and growth.

3.2.3 Induced dissolution of ferrous minerals in electrified Rattekaai sediment

In previous experiments on cable bacteria FeS had been identified as an important source of sulfide. To investigate induced dissolution of FeS in the incubated sediment, cores were sliced into 2 to 5 mm slices and porewater [Fe^{2+}] was determined (figure 11).

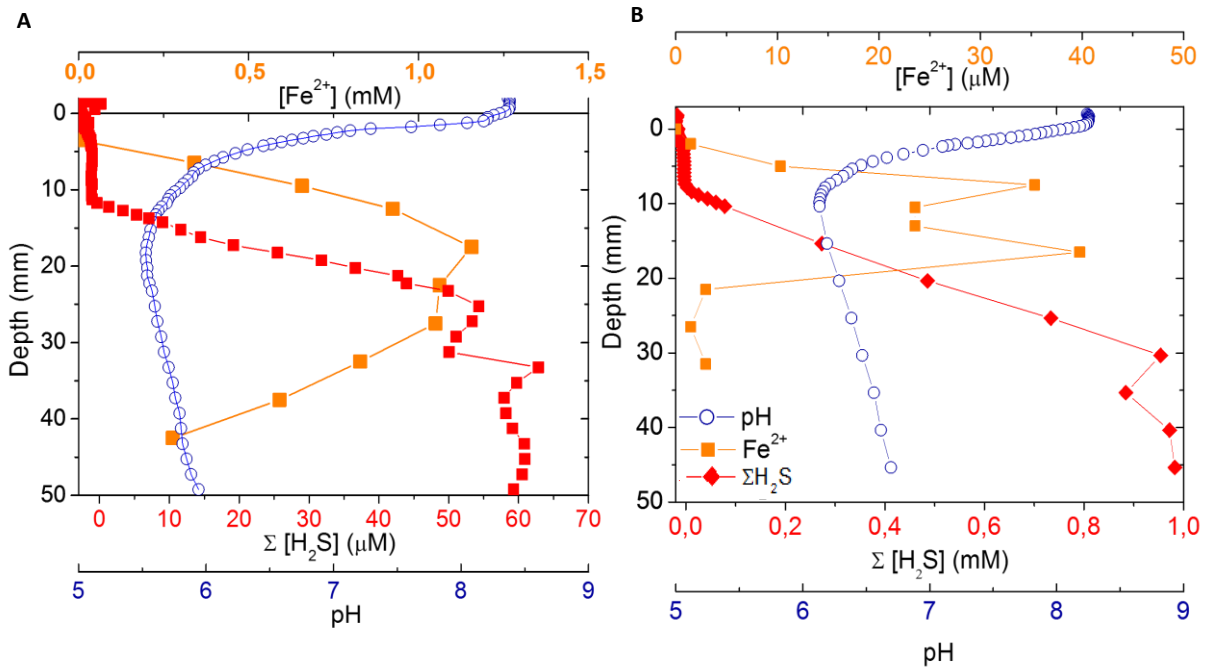

Figure 11. micro-sensor depth profiles of pH, H_2S and depth-profile of porewater Fe^{2+} Panel A: a core with a low global pH-minimum. Panel B: a core with a high global pH-minimum *Note the different units between panel A and B for [Fe^{2+}] and [ΣH_2S] .*

The largest concentration of Fe^{2+} (ferrous)-ions, exceeding 1 mM, was observed just below the suboxic zone between 18 and 30 mm depth (figure 11A). Here, the iron produced in the core reached a maximum concentration and diffused towards the surface-water-interface (SWI) as well as deeper into the euxinic zone. Towards the SWI a decrease in Fe^{2+}-concentration was observed, ultimately reaching zero below depths of 2 mm. At these depths, within the oxic zone, ferrous iron was quickly oxidized to iron (hydro) oxides which could be observed as a thick orange-colored layer on top of the sediment (appendix IV). A smaller amount of ferrous ions diffused towards greater depths and would likely reprecipitate as FeS, if the associated solubility product becomes sufficiently large. The ferrous ion concentration in the core were considerable indicating that cable bacteria did indeed induce release of ferrous ions in the Rattekaai sediment. The most likely sources of these ions would be acid-labile FeS.

pH is generally regarded as the main controlling factor in FeS dissolution. In the profiles of figure 6A evidence can be found for this, as the pH minimum coincided with the maximum Fe^{2+} concentration. Also, when a core was investigated with a less acidic pH profile, it was observed that the maximum Fe^{2+}-concentration was 20-fold lower (figure 11B). For this core, the total depth-range in which Fe^{2+} was present was just 17 mm compared to over 40 mm for the lower pH core.

3.2.3.1 Fe^{2+}-ion fluxes and pH effect

To further investigate effects of pH on ferrous iron release, a total of six ferrous iron concentration profiles were investigated. The flux towards both the euxinic zone (downward flux) and the SWI (upward flux). was investigated using Fick`s law (appendix V, table 2). In electrified sediments an electrostatic potential was present within the suboxic zone that influenced the magnitude of the upward ferrous iron flux.[10] For downward diffusion the effect was absent because net flux only started to occur below the suboxic zone (figure 11). Here there is no electrostatic gradient; $\frac{d\psi}{\mathrm{dz}} = 0$.

Table 2. Overview of the fluxes for six independent cores as calculated from depth profiles. *Fluxes were determined from the ferrous iron concentration profiles. ‡For the electrostatic potential flux an electrostatic potential of -0.08 V/m was assumed as mentioned in Nielsen et al. 2012.[10] ◊:Correction was calculated as ((Flux adjusted – Upward flux)/Flux adjusted)*100%*

CORE	GLOBAL PH MINIMUM	DOWNWARD FLUX (MMOL $FE^{2}*M^{-2}*D^{-1}$)	UPWARD FLUX (MMOL $FE^{2}*M^{-2}*D^{-1}$)	FLUX ADJUSTED FOR ELECTROSTATIC POTENTIAL (MMOL $FE^{2}*M^{-2}*D^{-1}$)‡	TOTAL FLUX	ELECTROSTATIC CORRECTION (%)◊
1	5.51	1.51	1.64	1.74	3.25	6.08
2	5.53	0.90	1.44	1.50	2.4	3.68
3	5.62	0.53	0.68	0.73	1.26	7.19
4	5.97	0.16	0.23	0.24	0.4	2.16
5	6.03	0.16	0.19	0.20	0.36	1.25
6	6.2	0.07	0.08	0.09	0.16	2.28

For all cores the downward flux was smaller than the upward flux, on average 25 %. This cannot be explained by the effects of the assumed electric potential alone, as the thus induced increase remained below 10% of the total flux. Likely, the precipitation reaction of ferrous iron with oxygen in the oxic zone is more efficient, which allowed to maintain a greater gradient towards the SWI than to the euxinic zone.

Cores with the lowest pH exhibited the greatest fluxes towards both the SWI as well as the euxinic zone. The effect of pH seemed to be strong: between the global pH-minima of 5.51 and pH 6.03 there was a ten-fold decrease in the observed fluxes. Further investigation on pH and Fe^{2+} fluxes was performed by plotting pH and the upward and downward fluxes. The obtained lines was found to be best fitted by an exponential decay curve (figure 12). Although a considerably accurate fit was made, the data presented here do not allow for reliable quantitative prediction of fluxes based solely on pH. Of unknown influences were, for instance, the effects of incubation time on buffering capacity of the porewater and the residual ferrous minerals available for dissolution. These factors will also influence the observed pH and the corresponding induced magnitude of dissolution.

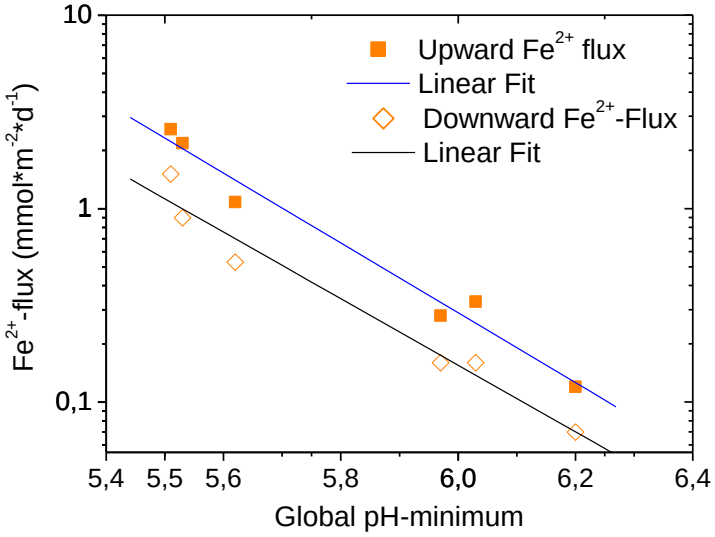

Figure 12. Summary of correlation between the global pH minimum and the upward and downward flux for six independent cores. *A logarithmic scale was employed on the y-axis. A fit was made using the fitting algorithm of the origins software, version 6.1. Obtained relation between pH upward flux was:* $y=2*10^{10}*e^{-4.148x}$, $R^2=0.98$, *for the downward flux:* $y=3*10^{9}*e^{-3.964x}$, $R^2=0,96$

3.2.4 Effects of anoxia on electrified sediment and the direct rate measurement method

3.2.4.1. Impact of anoxia on pH and sulfide micro-sensor profiles

Within the suboxic zone, sulfide released from dissolution and produced in sulfate reduction, cannot be directly measured, as long as cable bacteria consume nearly all sulfide and close the cryptic sulfur cycle. To disrupt the cycle, the oxygen source for cable bacteria was taken away, resulting in elimination of sulfide consumption. Hence, porewater sulfide concentrations would increase and would be measurable. This increase would then be representative of the sulfide consumption rate by the cable bacteria. First, for exploratory purposes, impact of anoxia on the sediment system was investigated by exposing a core to anoxia for 16 hours (figure 13 and 14).

The onset of anoxic conditions in the overlying water immediately caused a steep linear increase in ΣH_2S-concentration. An initial slope was observed of 0.25 µM*min^{-1} for H_2S and for H^+ this was 6.8 nM*min^{-1}. Linearity lasted for five minuted but at a ΣH_2S-concentration of 1.5 µM the increase in ΣH_2S-concentration slowly decreased until a concentration of 2.1 µM was reached. Now the ΣH_2S signal started to exhibit a rupture with the previous trends, resulting in an inclination towards a more shallow slope for both pH and ΣH_2S-increase (0.24 nM*min^{-1} (H^+) and 4.8 nM*min^{-1} (ΣH_2S). This decreasing slope continued until after minute 280, the [ΣH_2S] signal stabilized and attained a concentration of 3 µM. Interestingly, the pH continued to increase during this time and no longer seemed to be coupled to changes in ΣH_2S-concentration.

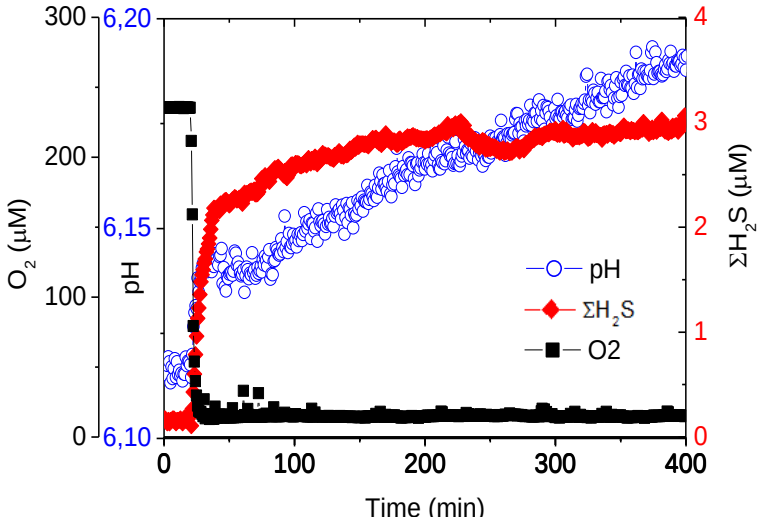

Figure 13. pH, H_2S and O_2 dynamic micro-sensor measurement during a 7 hour Long term anoxic perturbation experiment. *The experiment was performed at a depth of 9 mm.*

Contrary to what we initially expected, long-term anoxia only raised [ΣH_2S] by a few micro-molar. This observation was valid for the entire core, because, after 16 h of anoxia, throughout the previous suboxic zone [ΣH_2S] concentrations equilibrized between 1 and 2 µM (figure 14B). This indicated the suboxic sulfide consumption works closer to equilibrium than we had expected. Therefore, cable bacteria required [ΣH_2S] to be below micromolar concentrations in order for sulfide release to be continued.

A small H_2S-flux, 0.4 nmol*m^{-2}*d^{-1}, into the oxic zone was observed after 16 hours of anoxia. Here sulfide was likely consumed by redox proccesses with iron oxides and due to a minor residual oxygen influx into the sediment (section 3.2.4.2).

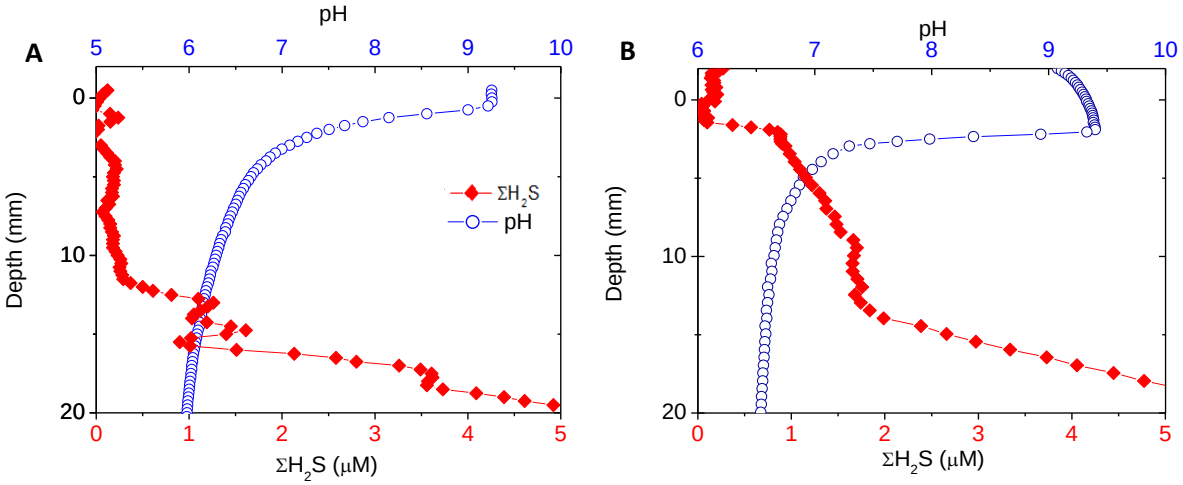

Figure 14. pH and H_2S-micro-sensor profiles of the suboxic zone for a core subjected to anoxia Panel A: before perturbation. Panel B: after 16 h of anoxia. *pH in the overlying water was increased from 8.2-8.4 to >9 due to outgassing of CO_2 by bubbling with N_2.Note this core is not the same as the core in figure 13.*

3.2.4.2. Measuring sulfide consumption of cable bacteria by direct rate measurement

From section 3.2.4.1 it followed that the initial rate of [ΣH_2S]-increase slows down as [ΣH_2S] exceeds low micromolar concentrations. On the contrary, when cable bacteria are active [ΣH_2S] will always remain below micro-molar concentrations and, therefore, in an active system, the initial rate would not decrease. From this it followed that measurement of true sulfide consumption by this experimental approach would only be possible if ΣH_2S-concentrations never exceeded rate-reducing concentrations. To ascertain low ΣH_2S-concentrations during perturbation, anoxia was applied for just 15 minutes. Then, oxic conditions were restored until pH and ΣH_2S values returned to pre-anoxic values. This cycle was repeated two times (figure 15A). This method will be termed direct rate measurement from here on.

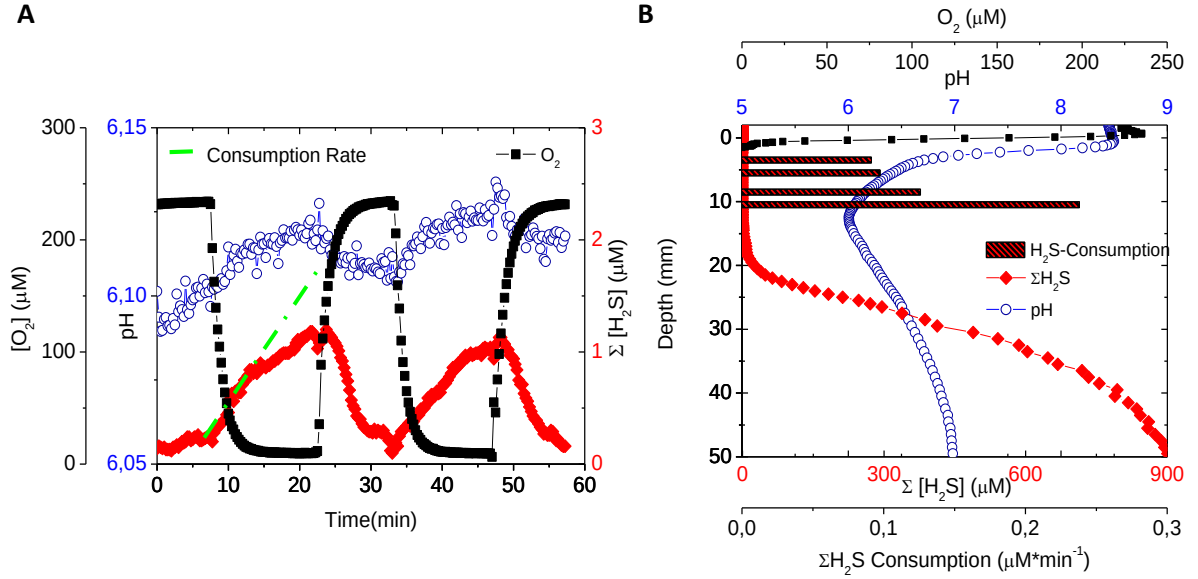

Figure 15. Panel A: direct rate measurement at a depth of 5.5 mm. *Anoxia was applied for 15 minutes after which oxia was restored until pH and [ΣH₂S] were back to oxic levels. The green line is a tangent and serves to demonstrate how the initial slope was determined.* **Panel B: pH, H_2S and O_2 micro-sensor depth-profile with the sulfide consumption rate depth profile.** *pH. O_2 and H_2S depth-profile (line+symbol) of core 1 on day 12. Consumption rates were indicated by the bars.*

In the first 5 minutes after the onset of anoxia the increase in [ΣH_2S] approximated linearity. This part of the graph was assumed to represent the sulfide consumption rate as experienced in active electrified sediment. Two cycles of interchanging oxic and anoxic conditions were performed; subsequently, the obtained rates were averaged to arrive at a single rate for the particular depth. Response of sulfide increase to anoxia was observed to be highly repeatable over these two cycles. Using this approach, multiple measurements were performed at regular depth intervals within the suboxic zone, obtaining a rate depth profile (figure 15B, appendix VI).

Using the direct rate measurement, no increase in sulfide was measured within the oxic zone in response to anoxia, possibly due to iron oxides. Just below the oxic zone, at a depth of 3.5 mm, a rate of 0.08 µM S*min^{-1} was measured, which continued to increase all the way up to the sulfide appearance depth. Here a maximum initial slope of 0.18 µM S*min^{-1} was measured. Over this same depth-range pH decreased as well, and, thus, again, a relation was observed between pH and the initial slope (appendix VII).

Next, to arrive at an area-specific rate, the values within the suboxic zone were integrated over depth and adjusted for porosity to calculate the aereal suboxic consumption rate for the electrified sediment.

$$=\frac{\Sigma Rates*(conversion\ from\ min\hat{}-1\ to\ d\hat{}-1)}{Nrates} * suboxic\ zone\ length * porosity=$$

$$=\frac{(0.08+0.09+0.12+0.18)*60*24}{4} *(0.014-0.0015\ m)*0.72=1.4\ mmol\ S*m^{-2}*d^{-1}$$

Apart from increase in [ΣH_2S] within the suboxic zone, there was also an immediate, rather strong response to anoxia within the euxinic zone. The increase in response to anoxia was odd as here, theoretically, the sediment would be oversaturated with respect to FeS. Although, initially mysterious, the same observation was made before in anoxic experiments.[2,34] These studies suggest that the measured increase in the euxinic zone could have been caused by contraction of the suboxic zone in response to anoxia rather than FeS-dissolution or sulfate reduction.

This contraction is however too slow to significantly increase [ΣH_2S] within the suboxic zone over a 15 minute time span. Therefore, lateral diffusional effects would most likely be responsible for the observed signal. All sulfide dynamics within the euxinic zone that are relevant for sulfide consumption will be accounted for by calculating the sulfide flux into the suboxic zone.

Residual oxygen consumption during near anoxic conditions

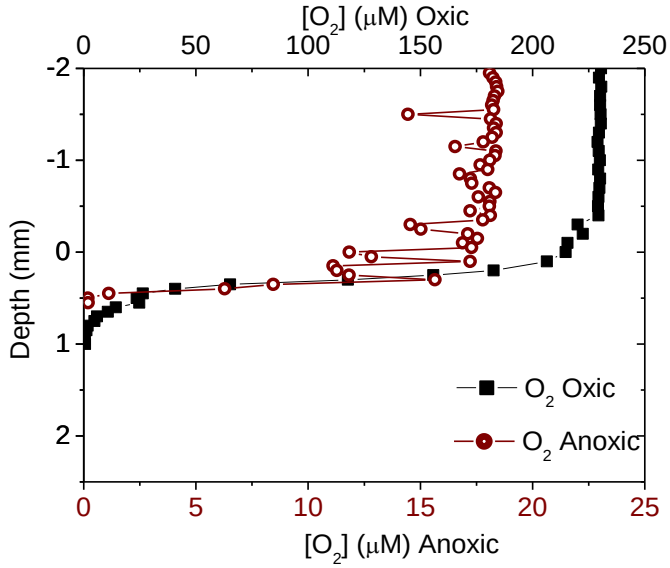

Figure 16. O_2-micro-sensor profile under oxic and anoxic conditions. *Profiles were obtained for the same core subjected to oxic and anoxic overlying water. Note the different x-axis scale used for the anoxic (red) and oxic conditions (black).*

Although anoxia was applied to the greatest possible extent, in the end a residual oxygen concentration could not be removed. This always remained limited to a range of 5 to 20 µM. In the here described case there was a rather high residual concentration of 18 µM O_2, which was 7.5% percent of that in fully aerated water (figure 16). For the aerated profile a flux of 18.2 mmol $O_2*m^{-2}*d^{-1}$ was calculated over the first 1 mm; the flux over the first 0.4 mm under near-anoxic conditions amounted to a comparatively large value of 2.3 mmol $O_2*m^{-2}*d^{-1}$: 13%. This means that during direct rate measurements a significant amount of oxygen might still be available for sulfide oxidation. If the magnitude of sulfide consumption during measurement was assumed to be proportional to the amount of residual oxygen flux, the true sulfide consumption rate would amount to be 13% higher.

3.2.4.3 Modelling pH and H_2S dynamics in response to anoxic perturbation

A. $FeS\ (s) \rightarrow FeS^0(aq)$ $K_{I,eq}=\frac{[FeS^0]_{eq}}{[FeS]}=10^{-5.7}$, ref:[47] (1)

B. $FeS^0(aq)+H^+(aq) \leftrightarrows Fe^{2+}(aq)+HS^-(aq)$ $K_{II,eq}=\frac{[HS^-]_{eq}[Fe^{2+}]_{eq}}{[H^+]_{eq}[FeS^0]_{eq}}=10^{2.2}$ ref:[48] (2)

C. $FeS^{0-}(aq)+2H^{+-}(aq) \leftrightarrows H_2S^{-}(aq)+Fe^{2+-}(aq)$

D. $H^{+-}(aq) + HS^{--}(aq) \leftrightarrows H_2S^{-}(aq)$ $K_{IV,eq}=\frac{1}{Ka_1([H_2S])}=\frac{[H_2S]_{eq}}{[HS^-]_{eq}[H^+]_{eq}}=10^{6.8}$ (3)

E. $FeS^{0-}(aq) + (2c1+c2)\ H^{+-}(aq) \rightarrow Fe^{2+} + c1\ H_2S^{-}(aq) + c2\ HS^{--}(aq)$

$K_{V,eq}=K_{IV}^{c1} * K_{II}=\frac{[HS^-]_{eq}^{c2}[H_2S]_{eq}^{c1}[Fe^{2+}]_{eq}}{[H^+]_{eq}^{2c1+c2}[FeS^0]_{eq}}$ (4)

In all direct rate measurements it was observed that ΣH_2S-concentration increased quickly but reached an equilibrium, at low micromolar concentrations. From literature it was deduced that, for the pH-range observed in our perturbation experiment, the dominant FeS-dissolution mechanism is that of pH-independent dissolution (reaction A, dominant at pH>5.3).[47,48] In this pathway, dissolution into Fe^{2+} and ΣH_2S occurs via the intermediary soluble complex FeS^0 (reaction B and C); equilibrium between these species, in the experimentally relevant pH-range, is reached at low micromolar concentrations of ΣH_2S, just observed in sections 3.2.4.1 and 3.2.4.2.[47,48] Here we will come up with a conceptual and mathematical model to describe the pH and H_2S dynamics within sediment subjected to anoxic perturbation. This to better understand the importance of the parameters pH, Fe^{2+} and ΣH_2S in the initial slope of ΣH_2S-increase and the equilibrium attained.

Conceptual model for [ΣH_2S]- increase and the establishment of the anoxic equilibrium

[ΣH_2S] in the suboxic zone was produced by both dissolution of FeS (s) and sulfate reduction. In the here presented model these sources will not be separately incorporated but were taken together as the experimental initial slope of sulfide increase (section 3.2.4.2). Such a simplification was possible because all in the end all produced sulfide will equilibrize with the species Fe^{2+}, FeS^0 and H^+ (reaction E).

FeS (S) dissolution into ΣH_2S (aq) and Fe^{2+} (aq) occurs via the intermediary specie FeS^0 (reaction A). The equilibrium constant for this reaction indicated that equilibrium with FeS^0 was reached at low concentrations (equation 1). The dissolution rate (10^{-4} mol*s^{-1}) was however, likely rapid, based on surface specific dissolution rate and the surface area of mackinawite.[48–50] Therefore, rates of FeS (s) dissolution into FeS^0 would be much greater than the sulfide consumption rates of cable bacteria. Hence, the FeS^0-pool was assumed to remain stable at a concentration of $10^{logK1}=10^{-5.7}$= 1.99 µM, as long as FeS (s) was abundant within the sediment.[47] Protonation of produced HS^- (reaction D) would also be a quick process and would not be rate limiting.

Based on this reactions (B) and (C) can be viewed as the rate-limiting reactions in FeS-dissolution and reactions (B) to (D) as the equilibrium determining reactions during anoxia. By combining these reactions, a total reaction could be set up (reaction E), in which speciation of ΣH_2S is determined by the pH during reaction. Using pH and the equilibrium constant for HS^-protonation (equation 3), the proportions of [HS^-] and [H_2S] compared to [ΣH_2S] (equations 5-7) could be calculated. These are also the stoichiometric coefficients for proton consumption in the overall reaction (reaction E), termed c1 and c2 (equation 8 and 9).

$[HS^-]=\frac{Ka[H_2S]}{[H^+]}$ (with $Ka=Ka_1(H_2S)=\frac{1}{K_{IV,eq}}=10^{-6.8}$) (5) $[H_2S]=\frac{[HS^-][H^+]}{Ka}$ (6)

(combining equation 5 and 6 to calculate $[\Sigma H_2S]$) $\Sigma H_2S=[H_2S]+[HS^-]\rightarrow[H_2S]*\frac{[H^+]+Ka}{[H^+]}$ (7)

$c1=\frac{[H_2S](eq.6)}{[\Sigma H_2S](eq.7)}=\frac{[H^+]}{Ka+[H^+]}$ (8) $c2=\frac{[HS^-](eq.5)}{[\Sigma H_2S](eq.7)}=\frac{Ka}{Ka+[H^+]}$ (9)

Using c1, $K_{V,eq}$ (equation 4) could be converted to an equilibrium constant with only $[\Sigma H_2S]$ instead of its individual species. This was done, using equation 8 and 9: $[H_2S]=c1*[\Sigma H_2S]$and $[HS^-]=c2*[\Sigma H_2S]$. Inserting this into (equation 4) gives the following equation 10 which now only depends on $[\Sigma H_2S]$:

$$K_V=\frac{c1^{c1}*c2^{c2}*[\Sigma H_2S][Fe^{2+}]}{[H^+]^{(2c1+c2)}[FeS^0]}. \quad (10)$$

Theoretical equilibrium constant value for anoxically perturbed cable bacteria sediment

Reaction E could be obtained by adding reactions B and D. The weight of reaction D is determined by the extent of protonation of HS^-, which is governed by c1. The total equilibrium constant of reaction E was calculated by multiplying the equilibrium constant $K_{II,eq}$ (equation 2) with K_{IV}^{c1} (equation 4). At pH 6 (c1=0.863) this would mean that the equilibrium constant for the total reaction: $K_{V,eq}= K_{II,eq}* K_{IV}^{c1}=10^{2.2}*(10^{6.8})^{0.863}=1.17*10^8$, a much larger value than for $K_{II,eq}$ alone. Addition of the protonation reaction increased the equilibrium concentration of $[\Sigma H_2S]$ in porewater.

Although pH was not entirely constant during the direct-rate measurement, the change in pH was rather small (section 3.2.4.2). Assumption of a constant pH would therefore not result in great deviations from true values for the equilibrium constants or proportionality constants, c1 and c2. Calculating with a fixed pH does make the kinetic-equations much simpler because only dynamics of $[\Sigma H_2S]$ had to be calculated.

Sulfide dynamics and equilibrium concentrations

$[Fe^{2+}]$ also increased during dissolution but for most depths it holds that $[Fe^{2+}]>>[\Sigma H_2S]$. The relative effect of $[Fe^{2+}]$-increase on K_V would therefore be comparatively small to that of $[\Sigma H_2S]$-increase. The approach to model ΣH_2S dynamics will be based on the experimentally determined initial rate (R_{H2S}). This rate will decrease as the reaction constant K_V approaches the equilibrium constant, $K_{V,eq}$.[9,51] The rate of H_2S increase will then be calculated as in equation 11, with R_{H2S} as the measured initial slope of $[\Sigma H_2S]$-increase in $\mu M*min^{-1}$(section 3.2.4.2):

$$\frac{d[\Sigma H_2S]}{dt}=R_{H2S}*(1-\frac{K_V}{K_{V,eq}}) \quad (11)$$

From this it follows that if $\frac{K_V}{K_{V,eq}}=1$, the change in $[\Sigma H_2S]$, i.e. $\frac{d[\Sigma H_2S]}{dt}$,will become zero, and, therefore, using equation 10, an equilibrium is attained at a $[\Sigma H_2S]$ of:

$$[\Sigma H_2S]_{eq}=\frac{[H^+]^{(2c1+c2)}[FeS^0]*K_{V,eq}}{c1^{c1}*c2^{c2}*[Fe^{2+}]} \quad (12)$$

From equation 12 it can be observed that the equilibrium ΣH_2S concentration is determined by $[Fe^{2+}]$, $[H^+]$, $[FeS^0]$ and $K_{v,eq}$. The large influence of pH is clearly visible in this formula because $K_{v,eq}$ also depends on pH (equation 4).

We can rewrite $\frac{K_v}{K_{v,eq}}$ in equation 11, using equation 12 and $[\Sigma H_2S]$ to, deduce equation 13.

$$\frac{d[\Sigma H_2S]}{dt} = R_{H2S}*(1-\frac{[\Sigma H_2S]}{[\Sigma H_2S]_{eq}}) \qquad (13)$$

Now this differential equation was integrated over time, with boundary conditions t=0, $[\Sigma H_2S]=[\Sigma H_2S]_0$ and t=∞,$[\Sigma H_2S]=[\Sigma H_2S]_{eq}$,. An exponential solution was obtained (equation 14). With $[\Sigma H_2S](t)$ as the developing concentration through time, $[\Sigma H_2S]_0$ as the initially present $[\Sigma H_2S]$ and $[\Sigma H_2S]_{eq}$ as the $[\Sigma H_2S]$ when equilibrium was reached:

$$([\Sigma H_2S](t) - [\Sigma H_2S]_0) = -([\Sigma H_2S]_{eq} - [\Sigma H_2S]_0)*\exp(-\frac{R_{H_2S}}{[\Sigma H_2S]_{eq}}*t)+[\Sigma H_2S]_{eq} \qquad (14)$$

This equation means that as t becomes larger, $[\Sigma H_2S](t)$ approaches its equilibrium value: $[\Sigma H_2S]_{eq}$. The slope of the graph becomes increasingly shallow over time, due to its exponential nature. In the end the speed with which equilibrium is attained depends on the experimentally determined initial rate and the $[\Sigma H_2S]_{eq}$. Because, all direct rate measurements in the report were performed for $[\Sigma H_2S]_0=0$, equation 14 could more simply be written as in equation 15.

$$[\Sigma H_2S](t) = -[\Sigma H_2S]_{eq}*\exp(-\frac{R_{H_2S}}{[\Sigma H_2S]_{eq}}*t)+[\Sigma H_2S]_{eq} \qquad (15)$$

Proton dynamics under anoxic conditions: modelling buffering effects within the porewater

For pH, development was calculated based on the solution of sulfide dynamics (equation 15). From the theoretical outline (reaction E) it was deduced that at pH 6, for every ΣH_2S produced 1.86 protons would be consumed. Buffering compounds within the porewater however greatly compensated for theoretical effects on $[H^+]$. This was observed by comparison between the initial slopes of $[\Sigma H_2S]$-increase (R_{H2S}) and $[H^+]$-increase: R_{H2S} was 0.25 µM*min^{-1} and for H^+ this was 6.8 nM*min^{-1} (section 3.2.4.1). To account for the discrepancy between the two rates a buffering factor (β) was introduced into the rate equation for H^+. This approach was outlined in literature (equation 16).[51] For every increase in H_2S a corresponding theoretical consumption of c2+2*c1 (called ν in literature) in H^+ would follow. Using this relation, the buffering factor could be calculated in the following way, using the experimentally determined initial slopes in section 3.2.4.1, (for pH=6.1, ν=c2+2*c1=1.83):

$$\beta = \frac{H^+ \text{ response based on reaction E}}{\text{true response}} = \frac{R_{H_2S}*\nu}{\text{Initial slope of } H^+ - \text{increase}} = \frac{0.25*10^{-6}*1.83}{6.8*10^{-9}} = 67 \qquad (16)$$

From the buffering factor it can be concluded that just 1 out of every 67 consumed H^+ would truly be consumed from the $[H^+]$ in the porewater. The rest of the protons would be compensated for by proton release of buffering species. Majority of the consumed acidity only results in a decrease in protonation of the buffering species.

Proton dynamics under anoxic conditions: pH-dynamics under anoxic conditions

As mentioned, the basis for the pH modelling will be the dynamics of H_2S-increase. The weighing factor, $\frac{\nu}{\beta}$, will be used to translate the theoretical effect of H_2S increase on proton consumption to the effect with a buffering system in place as in equation 17.

$$\frac{d[H^+]}{dt} = \frac{\nu}{\beta} * \frac{d[\Sigma H_2S]}{dt} \qquad (17)$$

For $[\Sigma H_2S](t)$ (equation 15) a solution has already been found. Differentiating this solution with respect to t, gives: $[\Sigma H_2S](t) = R_{H2S} * \exp(-\frac{R_{H2S}}{\Sigma H_2S]_{eq}} * t)$. Using equation 15, equation 17 was now written as in equation 18.

$$\frac{d[H^+]}{dt} = -\frac{\nu}{\beta} * R_{H2S} * (\exp(-\frac{R_{H2S}}{[\Sigma H_2S]_{eq}} * t)) \qquad (18)$$

Integration of this equation, with boundary conditions t=0, $[H^+]=[H^+]_0$ and t=∞, $[H^+]= [H^+]_{eq}$, yields equation 19:

$$[H^+]^t_0 = [\frac{\nu}{\beta} * R_{H2S} * \frac{[\Sigma H_2S]_{eq}}{[R_{H2S}} \exp(-\frac{R_{H2S}}{[\Sigma H_2S]_{eq}} * t)]^{\infty}_0 \rightarrow$$

$$[H^+](t) - [H^+]_0 = \frac{\nu}{\beta} * [\Sigma H_2S]_{eq} * \exp(-\frac{R_{H2S}}{[\Sigma H_2S]_{eq}} * t) - \frac{\nu}{\beta} * [\Sigma H_2S]_{eq} \qquad (19)$$

In equilibrium, attained for very large t, the exponent becomes zero. So equation 19 can be rewritten to obtain the following equation:

$$[H^+]_{eq} - [H^+]_0 = -\frac{\nu}{\beta} * [\Sigma H_2S]_{eq}. \qquad (20)$$

So, starting from an initial proton concentration, the final concentration was calculated by subtracting the total change induced by $[\Sigma H_2S]$-increase. Substituting $([H^+]_{eq}-[H^+]_0)$ for $-\frac{\nu}{\beta} * [\Sigma H_2S]_{eq}$ into equation 19 yields equation 21.

$$[H^+](t) = ([H^+]_{eq} - [H^+]_0) * \exp(-\frac{R_{H2S}}{[\Sigma H_2S]_{eq}} * t) + [H^+]_{eq} \qquad (21)$$

As can be observed in equation 21, the exponent which describes the dynamics was entirely constructed based on the solution of $[\Sigma H_2S](t)$. Therefore, the time at which $[H^+]$ will reach equilibrium will be entirely synchronized with $[\Sigma H_2S]$.

Fitting sulfide and pH dynamics for long term anoxia

Using the model described above, the long term anoxia experiment could now be fitted (figure 17). The parameters used for fitting were only β and [Fe^{2+}]. [FeS^0] was kept constant at 1.99 µM and R_{H2S} was determined from the experimental graph as the initial slope of ΣH_2S increase in µM*min^{-1} (appendix VI). H_2S dynamics could be fitted using [Fe^{2+}] and, using β, H^+-dynamics could be fitted.

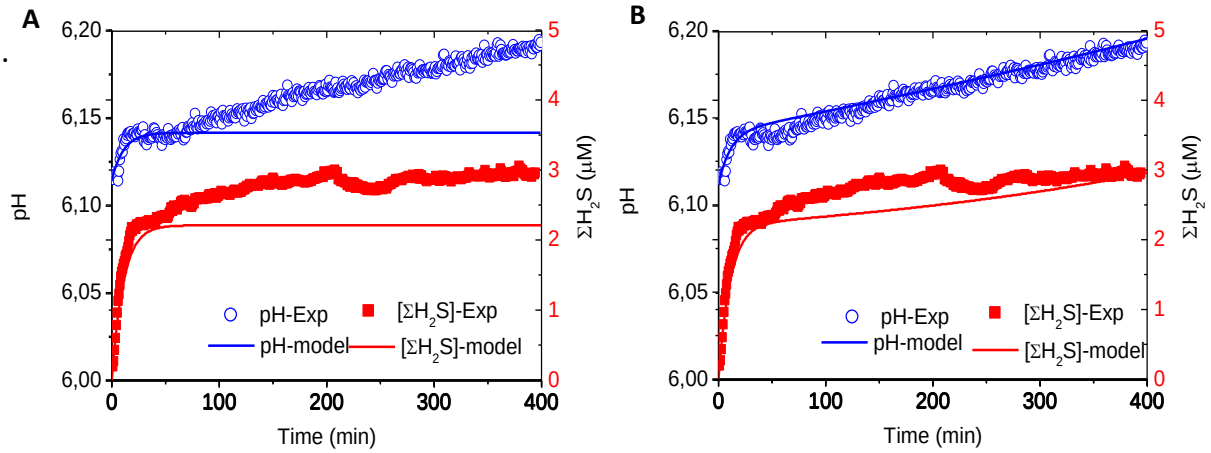

Figure 17. Fittings for long term anoxia perturbation measurement of figure 13. Panel A: fitted using the model. Panel B. fitted with the addition of crude transport and pH increase equations.

For figure 17A, using [Fe^{2+}]=650 µM and β=80, both experimental dynamics could be accurately described for the first 30 minutes. At this point equilibrium concentrations were reached for free protons at pH 6.14 and for [ΣH_2S] at 2.2 µM. At a depth of 9 mm an Fe^{2+}-concentration of 650 µM was within the expected range of values. For β, calculated using the initial rate method (equation 15) ,a value of 73 was calculated. A slight underestimation compared to what was deemed to be the best fit: β=80. After 30 minutes the fitted [ΣH_2S] and pH remained at the same level, but the actual pH and [ΣH_2S] increased.

This would likely be caused by three main factors, namely, 1) decrease in [Fe^{2+}] due to effluxes, resulting in increased [ΣH_2S] to reestablish equilibrium, 2) sulfate reduction and 3) microbial processes increasing pH.

So to address these theories, some crude [Fe^{2+}]-transport and pH increase equations were added to the model. In the end the fit in figure 17B was made by assuming a pH increase of 0.001 pH units*min^{-1} and assuming a very high Fe^{2+}-decrease rate of 0.6 µM*min^{-1}Although unsure what processes within the sediment cause the long-term H_2S and pH-dynamics, in the end, the observed dynamics were dependent on the dynamic net effect on the ratio $\frac{[Fe^{2+}][\Sigma H_2S]}{K_{v,eq}*[H^+]^{2c1+c2}}$ (equation 13).

Fitting of sulfide and pH dynamics in direct rate measurements

Perturbation experiments were performed on short-time scales and, therefore, the crude long-term equations for iron efflux and pH-increase were neglected in modelling these graphs. Just as in the previous paragraph, fitting was performed by adjusting parameters β and [Fe^{2+}] (figure 18A and B, appendix VIII). Here all the experimental data for core 1 on day 12 (figure 15B) will be fitted in order to construct a fitted Fe^{2+}-depth profile.

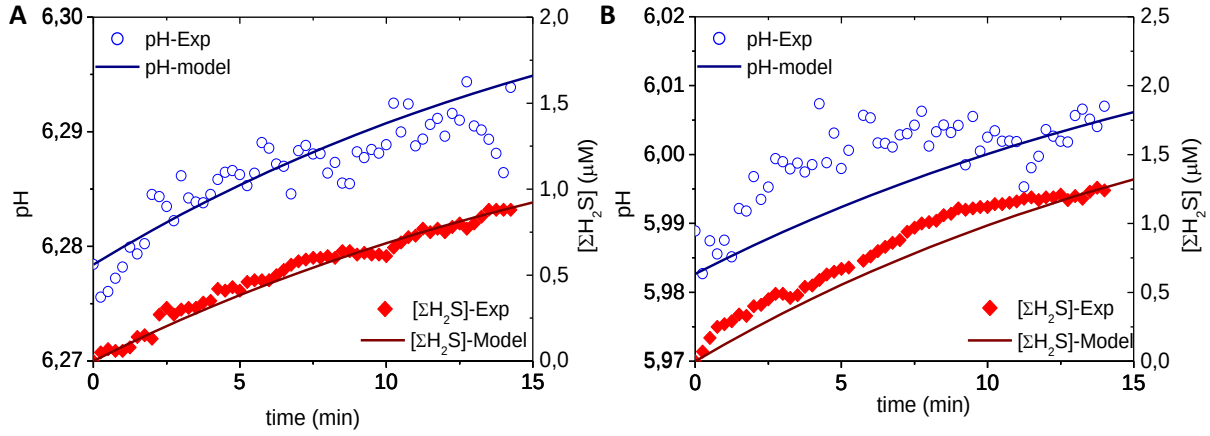

Figure 18. pH and H_2S profile from experimental and fitting data Panel A: for core 1 on day 12 at a depth of 3.5 mm, 2nd cycle. Panel B: core 1 on day 12 at a depth of 8.5 mm, 1st cycle. *Parameter values as used to fit the experimental graphs can be observed in table 3. More fitted curves can be observed in appendix VIII.*

Generally the experimentally observed [ΣH_2S] dynamics resembled that of an exponential curve. Model fits using the exponential model [ΣH_2S] tended to be close to the original shape of the graphs. Fits for pH were primarily based on the exponential curve of [ΣH_2S], but, especially for greater depths pH- tended to deviate from exponential behavior (figure 18B and appendix VII). pH generally had a steep initial increase after which an inclination occurred. This made pH rather hard to closely fit using our model. Also, due to the steep initial increase the calculation of β, based on the initial slopes (equation 15), was underestimated compared to the perceived best fit (β_{fit}, table 3). This indicated that pH and sulfide dynamics were not solely governed by FeS^0-dissolution. Sulfate reduction using organic matter would for instance also alter the ratio between pH and H_2S observed in the direct rate measurement.

[Fe^{2+}] was primarily fitted on the basis of the H_2S dynamics. Doing so, resulted in an [Fe^{2+}] range between 450 µM to 1300 µM over 10.5 mm depth (table 3). These values were larger than previously observed for cores with a global pH-minimum of 5.95 but they were within the previously observed range of lower pH cores (table 2).[10] These concentrations therefore do seem to make sense.

Table 3. Overview of the fitted parameters and experimental values as used in the model for fitting.

Core 1 **Day 12**	**Experimental values**			**Model parameters**		
Depth and cycle	**Initial H_2S-slope** **(µM*min^{-1})**	**pH_0**	**β_{exp}**	**β_{fit}**	**[Fe^{2+}] (µM)** **Model** **fit**	**[ΣH_2S]$_{eq}$** **Calc. by** **model**
3.5 mm cycle 1	0.0965	6.285	78	120	650	1.14
3.5 mm cycle 2	0.0863	6.278	78	80	450	1.6
5.5 mm cycle 1	0.1061	6.102	35	70	650	2.3
5.5 mm cycle2	0.0889	6.104	35	45	650	2.25
8.5 mm cycle 1	0.1255	5.988	44	45	1000	2.42
8.5 mm cycle 2	0.1273	5.982	44	35	1000	2.51
10.5 mm cycle 1	0.2123	5.950	51	35	1300	2.12
	0.2640	5.940	51	60	1300	2.27

3.2.4.4 Applying the direct rate measurement to measure suboxic sulfide consumption

Direct rate measurements, as described in section 3.2.4.2, were performed on two cores at two different time points during incubation. Diffusion of sulfide and oxygen into the suboxic zone was determined from the micro-sensor depth profiles using Fick`s laws (table 4, appendix V).

Table 4. Overview of sulfide fluxes, suboxic consumption rates and diffusive O_2 flux of the sediment for two independent cores after 12 and 21 days of incubation. *The pH, H_2S and O_2-profiles for both cores at both time points can be viewed in appendix IX. All rates within the suboxic zone can be viewed in in appendix VI.*

DAY 12	CONSUMPTION RATE SUBOXIC ZONE (MMOL ΣH_2S *M^{-2}*D^{-1})	DIFFUSIVE ΣH_2S FLUX (MMOL ΣH_2S *M^{-2}*D^{-1})	TOTAL ΣH_2S CONSUMPTION (MMOL ΣH_2S *M^{-2}*D^{-1})	DIFFUSIVE O_2 FLUX (MMOL O_2*M^{-2}*D^{-1})
CORE 1	1.6	2.7	4.28	18.3
CORE 2	1.0	0.3	1.36	Not Measured
AVERAGE	**1.3**	**1.5**	**2.82**	**18.3**
DAY 21	**Consumption rate suboxic zone (mmol ΣH_2S *m^{-2}*d^{-1})**	**Diffusive ΣH_2S flux (mmol ΣH_2S *m^{-2}*d^{-1})**	**Total ΣH_2S consumption (mmol ΣH_2S *m^{-2}*d^{-1})**	**Diffusive O_2 flux (mmol O_2*m^{-2}*d^{-1})**
CORE 1	1.1	1.8	2.9	12.1
CORE 2	0.9	0.1	1.0	10.2
AVERAGE	**1.0**	**0.95**	**2.0**	**11.6**

On day 12 of incubation, an averaged suboxic zone consumption rate value of 1.3 mmol sulfide*m^{-2}*d^{-1} was measured. At this point both core 1 and 2 had a rather similar consumption within the suboxic zone. The amount of sulfide diffusing from the euxinic zone was almost ten-fold higher in core 1. In core 2 the euxinic sulfide flux was only responsible for 20 % of the consumed sulfide, but, in core 1 it was by far the main source of sulfide. Averaged over both cores the total consumption rate amounted to 2.8 mmol ΣH_2S*m^2*d^{-1} with the majority coming from diffusional sulfide.

The total oxygen consumption of the sediment was, with 18.3 mmol O_2*m^{-2}*d^{-1}, six times larger than the summated sulfide consumption of the cable bacteria. Assuming a metabolic ratio between H_2 and O_2 of 1:2, in case H_2S was fully oxidized, then, cable bacterial consumption accounted for 30% of the oxygen uptake of the sediment. The remaining oxygen would then likely be consumed by other microbes and the oxidation of organic matter and ferrous ions.

On day 21 for both core 1 and core 2 a decrease in the euxinic sulfide flux was observed compared to day 12. On top of this there was a drop of 0.26 mmol $\Sigma H_2S * m^2 * d^{-1}$ in the average sulfide release within the suboxic zone. For core 1 this decrease was largest: 0.5 mmol $\Sigma H_2S * m^2 * d^{-1}$. Between day 12 and 21 all sulfide sources were more slowly provided and became more scarce. Hence, there was a decrease in the total sulfide available to cable bacteria. The total average sulfide consumption of the two cores dropped by 29% compared to day 12. Indicating a decrease in activity from day 12 to 21. Coinciding with this, the total oxygen demand of the sediment decreased by a third. However, using the same metabolic assumption as above, the relative contribution of cable bacterial activity to oxygen consumption remained rather stable: now 34%.

3.3 Stable Isotopic DIC enrichment and NanoSIMS analysis

Cable bacteria are chemo-litho-trophs which metabolize sulfide and oxygen. The sulfide sources and consumption have been investigated in section 3.2.4. To further investigate cable bacterial metabolism focus was put on both carbon and nitrogen assimilation by cable bacteria. To do so cores were enriched and incubated for 24 hours with ^{13}C-DIC and ^{15}N-NH_4.

3.3.1 Stable isotopic enrichment: injection of $Na_2{}^{13}CO_3$ and $^{15}NH_4Cl$

3.3.1.1 Core characteristics

For injection a core was taken that was incubated for 120 days but still was active according to our indicators (section 3.2.2); the profile showed a suboxic zone length of 12 mm and a global pH minimum of 6.0 (figure 19A).

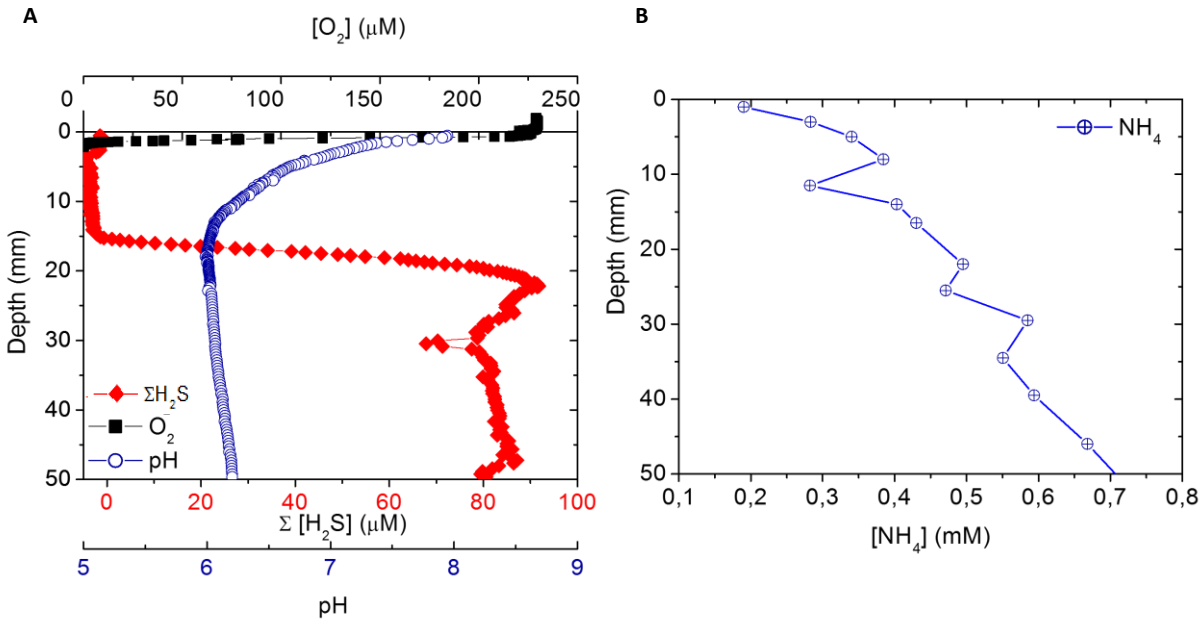

Figure 19. Panel A: pH, H_2S and O_2 Micro-sensor depth profiles of the core enriched with stable-isotopic-labelled nutrients. Panel B: ammonium depth profile.

The matrix into which the enriched compounds were dissolved was Mg and Ca-free artificial seawater with a similar pH as in the core (pH=6.15) and without buffering capacity (appendix X). This, to prevent precipitation with $Na_2H^{13}CO_3$ and to minimize disturbance to the geochemical environment of the cable bacteria.

With the same aim in mind a NH_4Cl-solution was injected with a concentration similar to that present in the core. For previous [NH_4]-depth profiles, an average concentration of 0.35 mM was found and therefore this concentration was used again here. For this core, in hind-sight, the $[NH_4]_{average}$ was determined to be 0.47 mM (figure 19B): thus, injection will have slightly decreased the [NH_4].

The effect on the pH-profile by injection of the enrichment-liquid was a decrease in smoothness (figure 20A). The effect on the length of the suboxic zone was much greater as it dropped from 12 mm to 6 mm in the injection area. The most likely explanation for this would be mechanical disturbance of the filaments and sediment by the injection needle. After 24 hours of incubation, the suboxic zone length was however completely restored, indicating that effects were only transient (figure 20B).

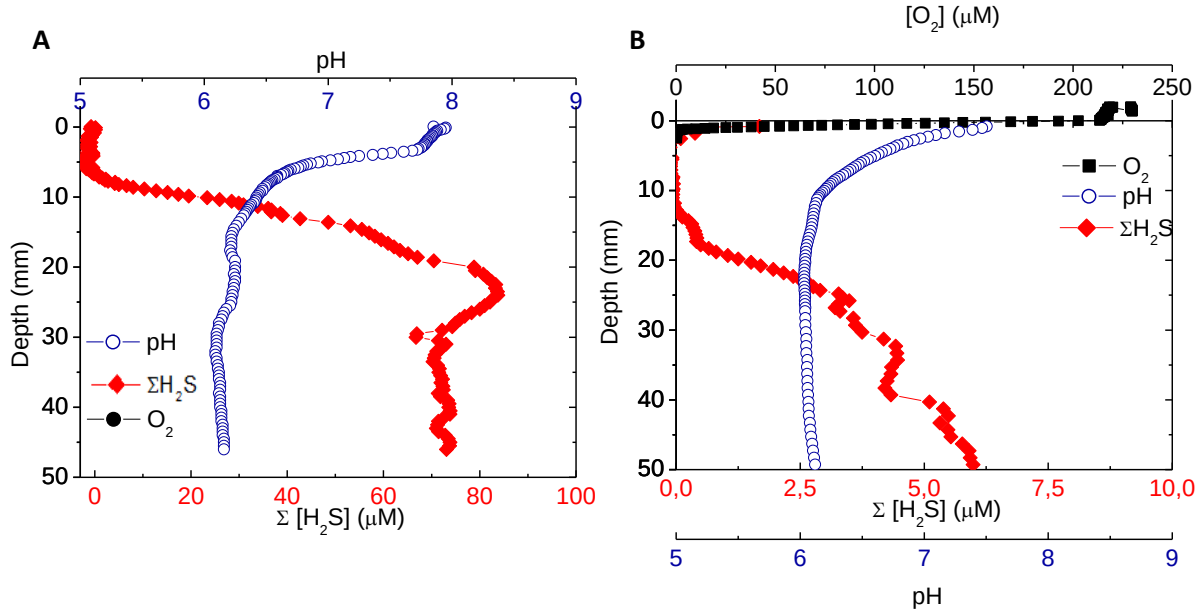

Figure 20. pH and H_2S micro-sensor depth-profiles of the sediment core that was incubated with the ^{15}N-NH_4 and ^{13}C-DIC solution. Panel A: Immediately after injection. Panel B: after 24 hours of incubation..

3.3.2 Mathematical intermezzo: relation between porewater and biomass enrichments

During incubation the cable bacteria will take up isotopically-labeled nutrients. This allows to determine the enrichment value of the biomass using NanoSIMS. By calculation, these values could be converted into biomass specific assimilation rate constants. In order to understand and appreciate the information contained within the enrichment values, it is required to understand the mathematics involved. Here an intermezzo is presented which explains these calculations and hopefully provides good insight herein.

3.3.2.1 Description of assimilation rate calculations

The final biomass` enrichment values do not only depend on uptake rate but also on the background biomass` enrichment and the porewater enrichment. Using these values a more generalized quantitative result could be obtained by calculating the corresponding assimilation rate constants (ARCs). These have the units $C*C^{-1}*d^{-1}$ and $N*N^{-1}*d^{-1}$. Here an example calculation will be presented for carbon enrichment of an enriched filament (filament A, section 3.3.4.4, appendix XVI).

The biomass specific carbon assimilation rate of filament A will be calculated using the differential equation describing the biomass` enrichment (calculated as a fractional abundance: $\frac{^{13}C}{^{13}C + {}^{12}C}$) in terms of a biomass specific uptake rate (C-ARC) and the initial biomass present(C-E(BM)):

C-E(BM)= *^{13}C-enrichment of biomass measured with NanoSIMS without background subtracted*
^{13}C-E(BM)$_{t=0}$=*^{13}C-enrichment of biomass at the start of incubation*
^{13}C-E(pw)=*Fractional ^{13}C-enrichment of the porewater after injection*
t=*time of incubation*
C-ARC= *biomass-specific assimilation rate of cable bacteria biomass.*
^{13}N-E(BM)$_{t=o}$= *^{15}N-Enrichment of biomass at the start of incubation*
^{15}N-E(pw)= *Fractional ^{15}N-enrichment of the medium after*

$$\frac{d^{13}\mathrm{C-E(BM)}}{\mathrm{dt}}=\text{C-ARC}*\text{C-E(BM)} \quad (21)$$

Integration of the equation with initial conditions leads to the following formula, in which ^{13}C-E_{BM} (t) is the measured biomass` enrichment, $^{13}$C-E(BM)$_{t=0}$ is the carbon enrichment at the start of the incubation and $^{13}$C-E(pw) is the enrichment of carbon in the porewater (and maximum biomass` enrichment):

$$^{13}\text{C-E(BM)(t)}-{}^{13}\text{C-E(BM)}_{t=0}=(^{13}\text{C-E(pw)}-{}^{13}\text{C-E(BM)}_{t=0})*e^{-\text{C-ARC}*t} \quad (22)$$

Then, for small C-ARC*t a linear approximation can be made, so, $e^{-\text{C-ARC}*t}\approx$-C-ARC*t. This gives the following equation:

$$\text{C-ARC}=\frac{^{13}\mathrm{C-E(BM)}-\ {}^{13}\mathrm{C-E(BM)t=0}}{^{13}\mathrm{C-E(pw)}-\ {}^{13}\mathrm{C-E(BM)t=0}}*t^{-1} \quad (23)$$

For filament A , with ^{13}C-E(pw)=0.35 ([DIC]0=20 mM and extent of dilution=1.5 cm, figure 21A), ^{13}C-FA(BM)=0.01 and ^{13}C-E(BM)=0.0321. The calculation will then be:

$$\text{C-ARC}=\frac{0.0321-0.01}{0.35-0.01}=0.118\ C*C_{biomass}^{-1}*d^{-1}$$

For nitrogen enrichment was calculated as $\frac{^{12}\mathrm{C}^{15}N}{^{12}\mathrm{C}^{14}N+\ {}^{12}\mathrm{C}^{15}N}$. A similar calculation was employed using ^{15}N-E(BM)$_{t=0}$= 0.0037 and ^{15}N-E(pw)= 0.10 (for extent of diffusion=1.5 cm, figure 21 A). Yielding a N-ARC of 0.121 $N*N_{biomass}*d^{-1}$.

All mean enrichments of the enriched filaments are given in appendix XVII.

3.3.2.2 Relation between C:N ratio of porewater and biomass

Based on the units of the ARCs, these constants could be viewed as a sort of replacement rates of present biomass. In case biomass of the same composition would be replaced, the assimilation rate constants would relate to one another as: $\frac{\mathrm{C-ARC}}{\mathrm{N-ARC}}$=1. This would be a reasonable assumption in the light of the rather fixed relation between C and N biomass` enrichment ($\frac{^{13}\mathrm{C-E(BM)}}{^{15}\mathrm{N-E(BM)}}$) for the cells of cable bacteria (section 3.3.4.4).

Looking at the $\frac{\mathrm{C-ARC}}{\mathrm{N-ARC}}$ calculation, it can be observed that porewater and the experimentally determined biomass` ^{13}C and ^{15}N-enrichment are of main importance. Unfortunately, porewater ^{13}C and ^{15}N-enrichment were only known within a some uncertainty. For ^{13}C-E (pw), uncertainty was especially large (section 3.3.3.2). Here we will investigate relation between ^{13}C:^{15}N-enrichment of porewater and biomass`, using $\frac{\mathrm{C-ARC}}{\mathrm{N-ARC}}$.

$$\frac{\mathrm{C-ARC}}{\mathrm{N-ARC}}=\frac{(^{13}\mathrm{C-E(BM)-}\ \ ^{13}\mathrm{C-E(BM)t=0})}{(^{13}\mathrm{C-E(pw)-}\ \ ^{13}\mathrm{C-E(BM)t=0})}*\frac{(^{15}\mathrm{N-E(pw)-}\ \ ^{15}\mathrm{N-E(BM)t=0})}{(^{15}\mathrm{N-E(BM)-}\ \ ^{15}\mathrm{N-E(BM)t=0})}$$

To make the formula look less complicated, the biomass`initial enrichment was assumed negligible. Of course this will lead to a small deviation of the true relation between C:N. But the factor is small compared to the other values and to some extent cancel out due to division. The simplification does however make the relation between porewater and biomass` enrichment become more clear:

$$=\frac{^{13}\mathrm{C-E(BM)}}{^{15}\mathrm{N-E(BM)}}*\frac{^{15}\mathrm{N-E(pw)}}{^{13}\mathrm{C-E(pw)}}.$$

The first term of the calculation ($\frac{^{13}\mathrm{C-E(BM)}}{^{15}\mathrm{N-E(BM)}}$) was known by experimental determination. Now, to arrive at a $\frac{\mathrm{C-ARC}}{\mathrm{N-ARC}}$ =1, the second term ($\frac{^{15}\mathrm{N-E(pw)}}{^{13}\mathrm{C-E(pw)}}$) should be the inverse of the first term. This, therefore, means that if $\frac{^{13}\mathrm{C-E(pw)}}{^{15}\mathrm{N-E(pw)}}$=$\frac{^{13}\mathrm{C-E(BM)}}{^{15}\mathrm{N-E(BM)}}$, then assimilation rate constants were the same ($\frac{\mathrm{C-ARC}}{\mathrm{N-ARC}}$=1). In order to reach equal assimilation rates the ill-constrained [DIC]0 (figure 21B) was chosen such to arrive at $\frac{\mathrm{C-ARC}}{\mathrm{N-ARC}}$=1 for clean untreated filaments (3.3.4.5).

3.3.3. Porewater enrichment of stable isotopically-labelled nutrients

3.3.3.1 ^{13}C and ^{15}N-enrichment of porewater

Table 5. Overview of calculation results for stable isotopic enrichment of the core`s porewater.

Enrichment (as Fractional abundance)	Molecule	Natural Background	Calculated enrichment	Concentration before enrichment (mM)	concentration after injection(mM)
$\frac{^{13}C}{^{13}C + {}^{12}C}$	DIC	0.01	0.35	20	26
$\frac{^{12}C^{15}N}{^{12}C^{14}N + {}^{12}C^{15}N}$	NH_4	0.0037	0.13	0.47	0.43

^{13}C was added to the inorganic carbon pool in the porewater by injecting 0.5 ml of 62 mM of $Na_2{}^{13}CO_3$ and 0.35 mM $^{15}NH_4Cl$ into a circular area with a 1 cm diameter with a depth of 5 cm. If the injected compounds remained within this column, injection had increased [DIC]0 from 20 to 26 mM (appendix XI). Concomitantly ^{13}C-enrichment increased from 0.01 to 0.35, about 35 times. Porewater ^{15}N-enrichment increased from 0.0037 to 0.13, but concentration slightly decreased by injection.

Unfortunately, [DIC] was not directly measured after the experiment, making this value a source of uncertainty. From literature a [DIC] between 15-30 mM, increasing with depth, was found for in-situ Rattekaai sediment.[36] The here used sediment had been incubated for some time, thereby possibly changing this value significantly. Based on the biomass enrichment of cable bacteria and assuming equal assimilation rate constants for nitrogen and carbon the best estimate for the initial [DIC] ([DIC]0) was judged to be 20 mM (section 3.3.4.4).

3.3.3.2 Dilution of enrichment by lateral diffusion of the stable-isotope labelled compounds

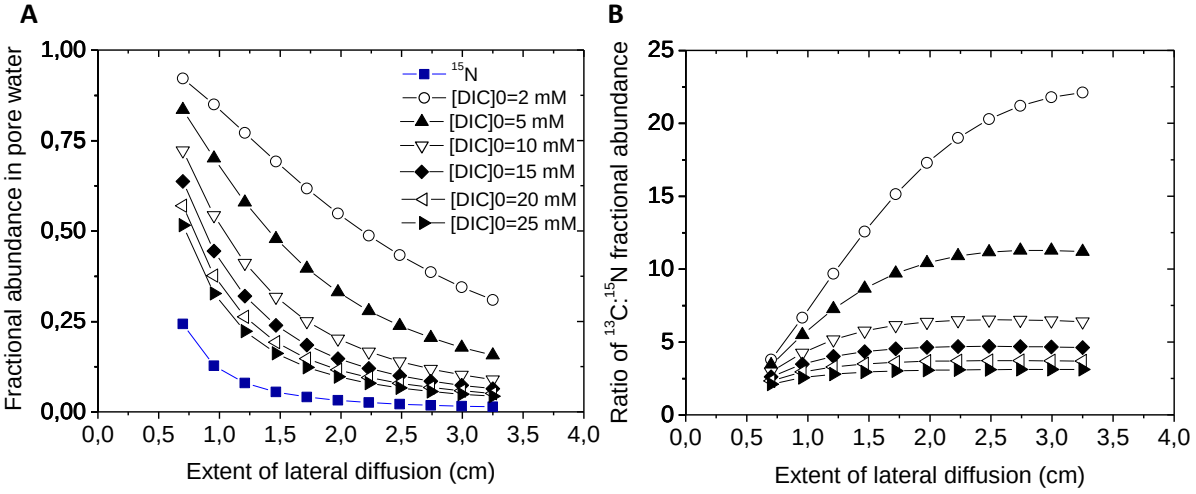

Figure 21. Panel A: dilutional effects on porewater enrichment values for ^{15}N and ^{13}C as a function of the extent of lateral diffusion. Panel B: ratio between the porewater ^{13}C and ^{15}N- Enrichment. *The porewater enrichment of nitrogen was fixed because the initial concentration of NH_4 was measured and therefore better constrained. Porewater enrichments were calculated as* $\frac{^{13}C}{^{13}C + {}^{12}C}$ *for carbon and for nitrogen as* $\frac{^{12}C^{15}N}{^{12}C^{14}N + {}^{12}C^{15}N}$..

Apart from the uncertainty in the [DIC]0 concentration further uncertainty was created because the isotopically labeled molecules were not physically confined within the circular area with a 1 cm diameter. This made diffusion an unknown influence on the porewater`s enrichment. Therefore, effect of diffusion on porewater enrichment was calculated for a lateral spread from 0.7 cm, until the maximum diameter of the core, 3.25 cm. Throughout this extent a homogeneous distribution was assumed (appendix XI).

For $^{15}NH_4$, effects of lateral diffusion were initially strong, decreasing by 60% from d=0.95 cm to d=1.45 cm (figure 21A). For ^{13}C-DIC there was also a decrease in porewater enrichment with increasing diffusion but it did not decrease as swiftly as ^{15}N-enrichment. This was caused by the lower initial enrichment of ^{15}N making the initial dilution effects stronger for nitrogen. Therefore, $\frac{^{13}C-E(pw)}{^{15}N-E(pw)}$ for porewater initially increased with increasing extent of diffusion (figure 21B). However, with further extents of diffusion, a maximum ^{15}N:^{13}C enrichment ratio was reached which did not greatly change with further diffusion. This was because with greater extent of diffusion, the relative change in ^{13}C and ^{15}N-enrichment became increasingly similar.

From figure 21B it was deduced that the higher [DIC]0 was, the less extent of diffusion was required for $\frac{^{13}C-E(pw)}{^{15}N-E(pw)}$ to become constant. What was further important to note was that for higher [DIC]0 the variability in the maximum ratio became increasingly smaller. For instance for [DIC]0=2 mM the maximum ratio was 22. Changing to [DIC]0=10 mM decrease the maximum ratio all the way to 7. In the relevant range for Rattekaai sediment, being 15-25 mM[36], the maximum ratio only decreased from 5 to 2. Therefore, variability in the porewater enrichment was actually not as large as might be expected.

3.3.4. Carbon uptake rates and enrichment cable bacteria

Isotopic enrichment in biological organisms, apart from experimental settings, can also occur due to natural fractionation by preferential isotope uptake of enzymes. This would be of influence on the quantitative results shown throughout section 3.3.4. To assess background fractionation, the fractional abundance of inactive filaments was analysed (Appendix XII). From this analysis, based on 91 background values and 586 inactive cells, it was established that the natural isotopic biomass signature did not significantly differ from the background values. Natural fractionation was therefore not regarded of influence on the stable-isotopic assimilation results.

3.3.4.1 Differential enrichment between cable bacteria in the oxic and suboxic zone

The total number of analysed cells was easy to count as these were separated for every single measurement as a region of interest (ROI) (figure 5). Counting filaments, however, was a harder feat due to the great lengths of filaments and their tendency to intertwine with themselves and other filaments (appendix XIII.) Even when using high resolution SEM images, it was difficult to find the beginning and end for individual filaments. Not all filaments could be disentangled, but a good estimation could be made for the number of filaments in most samples. In total 31 unique filaments were identified of which 1027 cells were measured in 50 separate measurements (table 6).

Table 6. Overview of the amount of analysed filaments and cells and whether they were enriched.

Depth layer	SDS/EDTA-treated	Analysed Filaments (#)	Enriched Filaments (#)	Analysed Cells (#)	Enriched cells (#)
Oxic	Yes	5	0	53	0
Zone	No	9	0	391	0
Suboxic	Yes	5	3	124	99
Zone	No	12	2	509	212

Out of the in total 1027 individual cells, 311 were found to be enriched with respect to both ^{13}C and ^{15}N. All these cells were located in just five of the 31 filaments according to the filament identification. Intriguingly, all active filaments came from the suboxic zone and none from the oxic zone. Considering the enrichment efficiency for filaments within the suboxic zone (5 active on a total of 17), there would be a good chance of finding an active filament out of the 14 analysed filaments in the oxic zone as well. Therefore, the absence of enrichment in the oxic zone was unlikely a result of a sampling bias, but, instead, caused by a real difference in metabolic activity in different parts of the filament.

3.3.4.2 *Homogeneity of enrichment within enriched filaments*

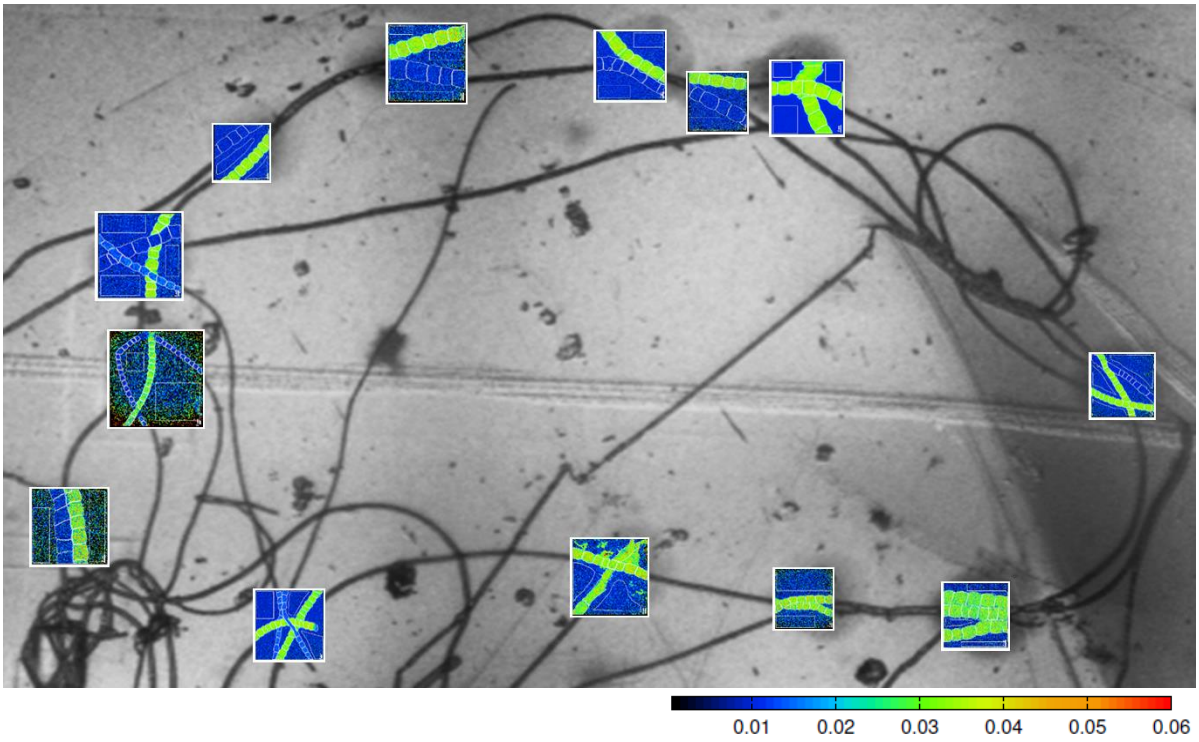

Figure 22. Combined SEM and NanoSIMS images (^{13}C-fractional abundance) for untreated filament A from the suboxic zone. *On top of a SEM image, NanoSIMS images were placed at their specific locations. To all NanoSIMS images the scale bar, signifying the ^{13}C- enrichment, calculated as* $\frac{^{13}C}{^{13}C + ^{12}C}$*, apply.*

Zooming in on cell enrichment of the untreated filament A from the suboxic zone (appendix XIII) allowed to construct an overview picture (figure 22). For filament A enrichment at a total of 14 locations was investigated. Observed was that all the investigated cells were active and had a rather similar value for both nitrogen and carbon enrichment. Interestingly, if nitrogen enrichment was relatively high this was also the case for carbon (figure 23), suggesting a related uptake. After subtraction of the background fractional abundance, the coefficient of variation, calculated as $\frac{\text{Std.deviation}}{Mean\ enrichment} * 100$, was just 8.1% for ^{13}C-enrichment (table 7) and For ^{15}N-enrichment the coefficient of variation was 13%.

Filament A was 4.2 mm long, and, all cells were about 3.5 µm long, this means that the filament was constructed from about 1260 cells. Over a large number of cells the filament showed a rather similar enrichment. The same pattern was observed for the other four enriched filaments, although with differing mean enrichments and standard deviations (table 7, Appendix XV).

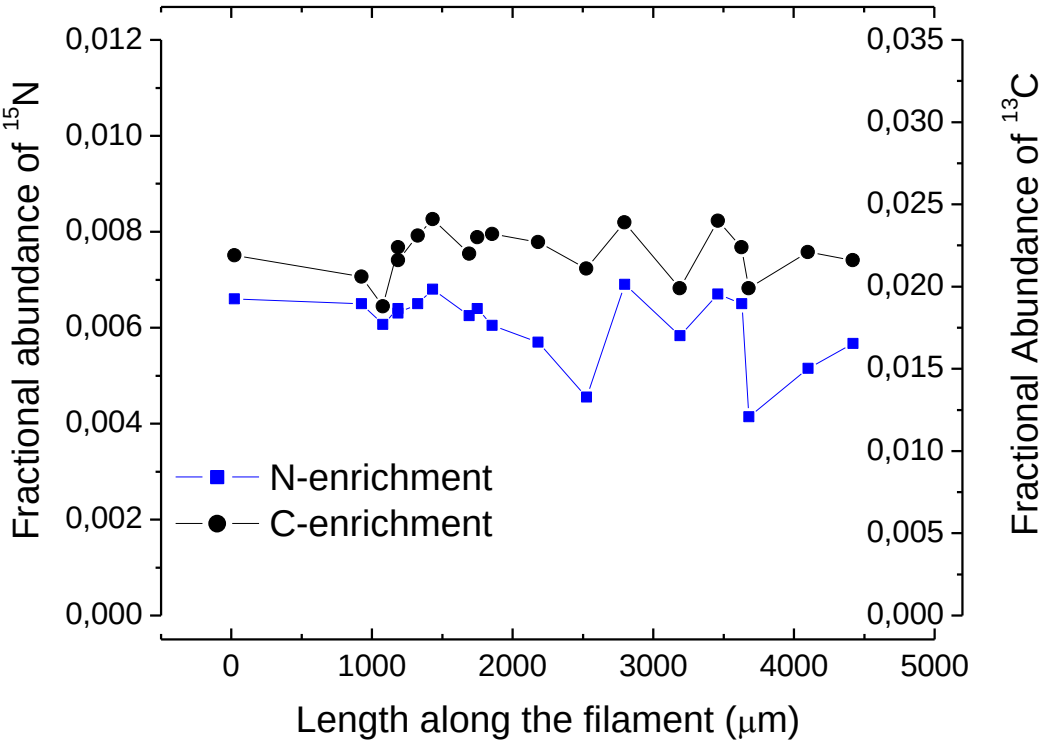

Figure 23. Enrichment values for separate measurements at several locations along the filament. *Every point signifies the mean enrichment (calculated as fractional abundance) of the cells belonging to filament A within one view at the specific location. The background enrichment was subtracted from the here presented ^{15}-enrichment and ^{13}C-E values (^{13}C-E(BM)-^{13}C-E(BM)t=0 and ^{15}N-E(BM)-^{15}N-E(BM)t=0).*

3.3.4.3 Comparison of homogeneity in carbon uptake of enriched filaments

Within a filament, enrichment was highly homogeneous but between filaments there was a great disparity in observed enrichment. For instance, between untreated filament A and filament C there was a six-fold difference in ^{13}C-enrichment (table 7). The standard deviation of enrichment within the cells of a filament confirmed the observations in figure 22 and 23: cells, belonging to one filament, all had a strikingly similar ^{13}C and ^{15}N-enrichment. For cells within a filament the coefficient of variation was generally within 15%, except for filament C. Filament C had a rather high relative standard deviation of 25% of the background-corrected enrichment value. This was likely caused by the low background-corrected enrichment. For filaments SDS A and SDS C a remarkably similar enrichment and standard deviation was observed, which would suggest, based on the homogeneity principal, that these two filaments could actually be one and the same filament.

Table 7. Overview of average enrichment, standard deviations and coefficient of variation ($\frac{\text{Std.deviation}}{\textit{Mean enrichment}} * 100\%$) for the 5 enriched filaments. *For the enrichment the background enrichment was subtracted from the mean value (i.e ^{13}C-E(BM)-^{13}C-E(BM)t=0 and ^{15}N-E(BM)-^{15}N-E(BM)t=0). A SEM image of the filaments can be observed in appendix XIII.*

FILAMENT	MEAN ^{15}N-ENRICHMENT	STANDARD DEVIATION	COEFFICIENT OF VARIATION (%)	NUMBER OF ANALYSED CELLS(#)
FILAMENT A	6.08*10^{-3}	8.40*10^{-4}	14	165
FILAMENT C	9.70*10^{-4}	2.44*10^{-4}	25	38
SDSA	3.03*10^{-3}	1.99*10^{-4}	7	36
SDSB	5.13*10^{-3}	6.73*10^{-4}	13	23
SDSC	2.94*10^{-3}	2.02*10^{-4}	7	37
AVERAGE	**3.63*10^{-3}**	**4.32*10^{-4}**	**12**	**-**
FILAMENT NAME	**Mean ^{13}C-Enrichment**	**Standard deviation**	**Coefficient of variation (%)**	**Number of analysed Cells (#)**
FILAMENT A	2.21*10^{-2}	1.79*10^{-3}	8	165
FILAMENT C	4.05*10^{-3}	9.19*10^{-4}	23	38
SDSA	1.55*10^{-2}	1.27*10^{-3}	8	36
SDSB	2.29*10^{-2}	2.95*10^{-3}	13	23
SDSC	1.44*10^{-2}	1.36*10^{-3}	9	37
AVERAGE	**1.58*10^{-2}**	**1.66*10^{-3}**	**10**	**-**

SDS was hypothesized to increase variability in the enrichment values but at first glance did not exhibit this effect (table 7). The highest standard deviation, for SDS B, was similar to that of the untreated filament A, and, even lower than that of filament C (table 7). This surprisingly low standard deviation could also be caused by the shorter size of the SDS-filaments. Cells closer to one another would behave more similar because they are in a similar chemical environment. Filament A was the longest filament by far and measurements would therefore also span a more diverse chemical environment. Possibly this would be a stronger source of variability than induced by SDS treatment. Possibly, if standard deviation was determined based on measurements at one location, results might indicate that SDS did increase variability.

3.3.4.4 Correlation between the fractional abundance of ^{13}C and ^{15}N for untreated filaments

As noticed earlier for filament A (figure 23), there was a correlation between the enrichment in ^{15}N and ^{13}C. For ^{13}C on average a 3.6 times higher enrichment value was found than for ^{15}N- within untreated enriched filaments. This correlation proved to be rather persisntent for all untreated enriched cells (figure 24) and possibly even through all cell phases (figure 25, appendix XIV).

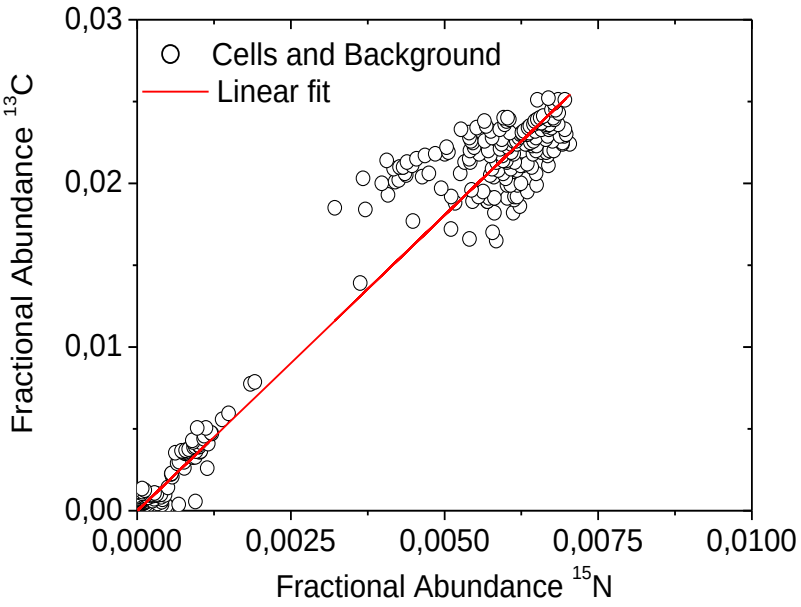

Figure 24. Correlation between ^{13}C and ^{15}N enrichment for the untreated suboxic samples. *A linear fit was made using the origin v. 6.1 fitting software to assess the correlation between enrichment in carbon and nitrogen (y= 3.61x, R^2=0.97, red). All points were enrichment values forf individual cells and backgrounds, analyzed over 20 dependent measurements. The background fractional abundance, corresponding to the specific measurement, was subtracted of all fractional abundance values (i.e. ^{13}C-E(BM)-^{13}C-E(BM)t=0 and ^{15}N-E(BM)-^{15}N-E(BM)t=0)*

In some cells, elongated, highly enriched regions were observed which were likely in a growing and dividing phase during isotopic labelling (figure 25A and appendix XIV). Even though the region exhibited different metabolic activity, the ^{13}C:^{15}N enrichment correlation remained the same. This means the correlation was persistent throughout all the measurements and seemingly even all developmental stages of the cell. There were no indications that the cable bacteria altered bulk biomass composition at any point during incubation. Therefore, the assumption of $\frac{C-ARC}{N-ARC}=1$, as made in section 3.3.2.2, would seem to be correct. And, continuing on this, it would now hold that porewater and biomass enrichment should be equal: $\frac{^{13}C-E(pw)}{^{15}N-E(pw)}=\frac{^{13}C-E(BM)}{^{15}N-E(BM)}$ (section 3.3.2.2). For the porewater enrichment the most likely [DIC]0 would then be 20 mM because then the maximum and rather constant value for $\frac{^{13}C-E(pw)}{^{15}N-E(pw)}$ was 3.6 (figure 21B).[36]

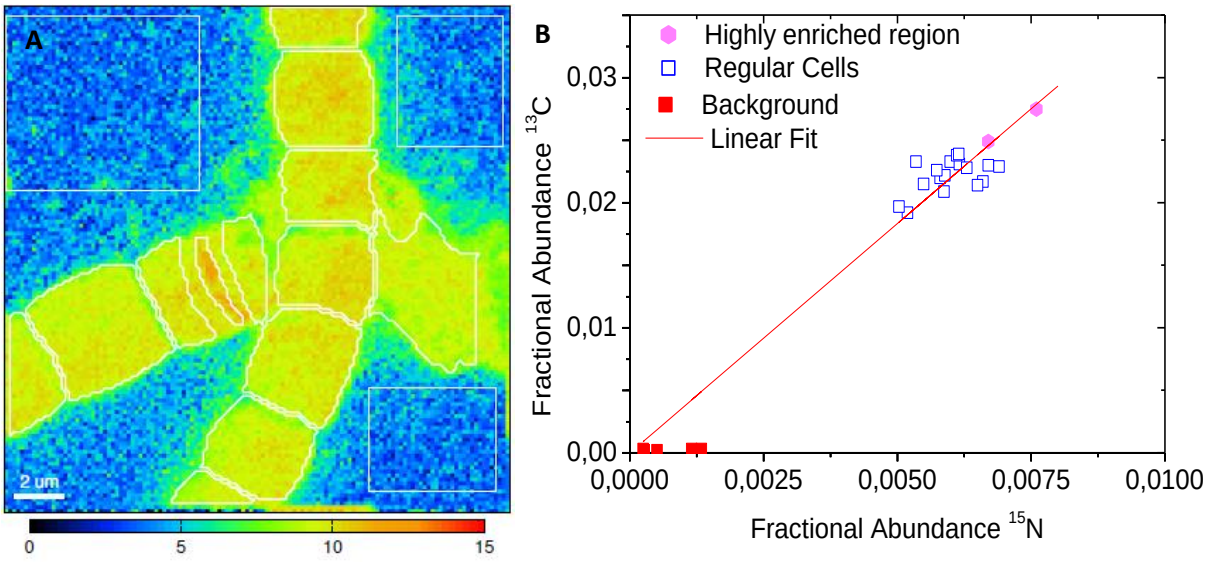

Figure 25. Panel A:NanoSIMS image depicting the ^{15}N-Enrichment values for part of filament A. *Enrichment was calculated as a fractional abundance: $\frac{^{12}C^{15}N}{^{12}C^{14}N+\ ^{12}C^{15}N}$. The scale bar is given in units of 10^{-3}, without subtraction of the background. Notice the highly enriched, red band on the left side of the filament.* **Panel B: Correlation between the observed fractional abundances of regular cells and the highly enriched regions.** *Data points include the second measurement which can be viewed in the appendix XIV. The enrichment values were normalized to the background values ((i.e. ^{13}C-E(BM)-^{13}C-E(BM)t=0 and ^{15}N-E(BM)-^{15}N-E(BM)t=0**)**. The best linear fit was found for y=3.67x, R^2=0.96.*

3.3.4.5 Fractional abundances of ^{13}C and ^{15}N of SDS-treated filaments

For SDS treated filaments there was a large alteration in the observed ^{13}C to ^{15}N-Enrichment correlation, changing from 3.6 to 4.7 (figure 26). Because the SDS treated filaments were retrieved from the same incubated core, initially, SDS-treated filaments, would have exhibited the same ^{13}C:^{15}N correlation as filament A and C. Thus, SDS seemed to have mostly removed nitrogen-rich compounds, thereby, causing $\frac{^{13}\mathrm{C-E(BM)}}{^{15}\mathrm{N-E(BM)}}$ to increase.

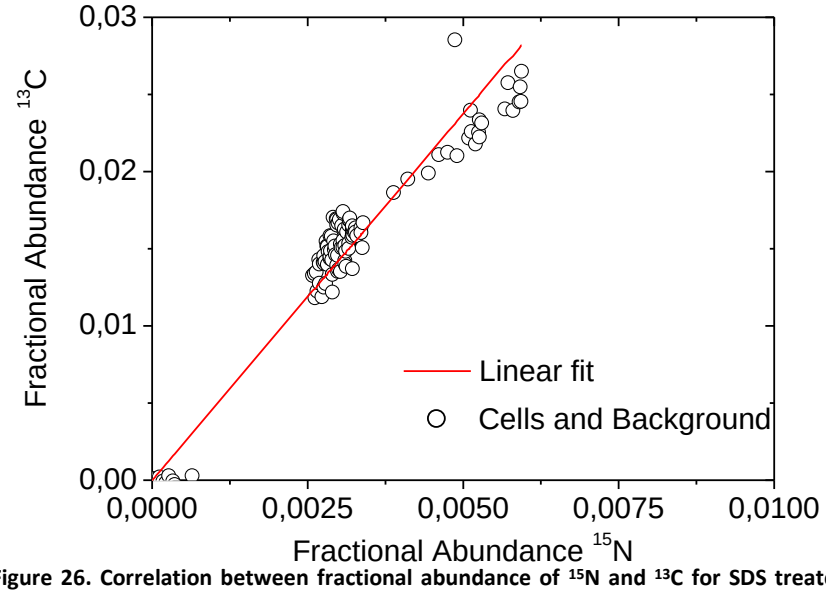

Figure 26. Correlation between fractional abundance of ^{15}N and ^{13}C for SDS treated filaments. *Background enrichment was subtracted from the absolute enrichment (i((i.e. ^{13}C-E(BM)-^{13}C-E(BM)t=0 and ^{15}N-E(BM)-^{15}N-E(BM)t=0). Based on this data a linear fit of the C:N relation was made (y=4.71x, R^2=0.98).*

3.3.4.6 Overview of the calculated assimilation rate constants

For, the likely best estimate of [DIC]0=20 mM (section 3.3.4.4), $\frac{^{13}\mathrm{C-E(pw)}}{^{15}\mathrm{N-E(pw)}}$ attained a value of 3.6 at a diffusion of 1.5 cm which remained more or less constant up to 3.25 cm (figure 21B). With extent of diffusion the absolute porewater enrichment however did still decrease (figure 21A), which would also alter the calculated assimilation rate constants. Because of this, the ARCs were calculated for the two most extreme extents of diffusion for which it held that $\frac{^{13}\mathrm{C-E(pw)}}{^{15}\mathrm{N-E(pw)}}$ was 3.6. Thus, to calculate the independent uptake rates (C-ARC and N-ARC), porewater ^{13}C and ^{15}N-enrichment were used for [DIC]0=20 mM and extents of diffusion of 1.5 cm and 3.25 cm (figure 21A, section 3.3.3.2).

Table 8. Overview of calculated N-ARCs, C-ARCs and their ratio for all enriched filaments. *The units of N-ARC are N*N^{-1}*d^{-1} and the units of C-ARC are C*C^{-1}*d^{-1}. The mean enrichment values for the filaments can be viewed in appendix XVI.*

FILAMENT	1.5 CM EXTENT OF DIFFUSION			3.25 CM EXTENT OF DIFFUSION		
	C-ARC	N-ARC	$\frac{\mathbf{C-ARC\ (C*C^{-1}*d^{-1})}}{\mathbf{N-ARC\ (N*N^{-1}*d^{-1})}}$	C-ARC	N-ARC	$\frac{\mathbf{C-ARC\ (C*C^{-1}*d^{-1})}}{\mathbf{N-ARC(N*N^{-1}*d^{-1})}}$
FILAMENT A	0.118	0.121	0.978	0.591	0.530	1.116
FILAMENT C	0.019	0.022	0.854	0.094	0.097	0.973
SDSA	0.059	0.085	0.692	0.293	0.372	0.789
SDSB	0.100	0.125	0.799	0.499	0.548	0.911
SDSC	0.057	0.079	0.726	0.286	0.346	0.828
AVERAGE	**0.071**	**0.086**	**0.81**	**0.353**	**0.378**	**0.92**

For filament A, and a diffusion extent of 1.5 cm, C-ARC was calculated to be 0.118 C*C^{-1}*d^{-1}; the N-ARC was very similar with a value of 0.121. For filament A and 1.5 cm extent of diffusion the ratio $\frac{\mathrm{C-ARC}}{\mathrm{N-ARC}}$ =0.98 was very close to 1 and this ratio only increased by 0.14 going to an extent of 3.25 cm. The ARCs of the individual molecular species did however greatly change with extent of diffusion. For filament A the C-ARC was 5 times as large for 3.25 cm compared to 1.5 cm. For filament C the general pattern was similar, for both extents of diffusion a ratio close to 1 was found for $\frac{\mathrm{C-ARC}}{\mathrm{N-ARC}}$. But the ARCs increased over five times from 1.25 cm to 3.25 cm.

For the SDS-treated filaments, $\frac{\mathrm{C-ARC}}{\mathrm{N-ARC}}$ was further away from 1 for both extents of diffusion. This was caused by the different ratio of $\frac{^{13}\mathrm{C-E(BM)}}{^{15}\mathrm{N-E(BM)}}$, which was 4.7, unlike the calculated ratio of porewater, which was 3.6. Consequently, $\frac{\mathrm{C-ARC}}{\mathrm{N-ARC}}$ was calculated to be smaller than 1. This suggests a preferential uptake of nitrogen over carbon. More likely however was that the altered correlation was an effect of the SDS treatment.

As suggested by the altered correlation, the value of the ARCs for SDS-treated filaments could have been altered by the SDS treatment. Albeit the treatment, the SDS filaments, all had larger ARCs than filament C. Even though the average ARC might be influenced by the treatment, the SDS treated filaments did seem to have an ARC within a relevant range. If the doubling time for the cable bacteria was calculated using the mean C-ARC value, for a diffusion of 1.5 cm, then doubling time would be ($\frac{\ln(2)}{\mathrm{C-ARC(average)}}$)= 9 days. This was on the low side compared to peak activities in literature but this does make sense because sulfide sources will have become more scarce.

3.3.4.7 [DIC] and possible assimilation of organic carbon

Although the above calculations and analyses were performed using the most likely assumptions regarding [DIC]0 and ratio of assimilation rate constants. The porewater concentrations and enrichments were not directly measured. Furthermore, there are a number of processes known to occur in electrified sediment that could have great effects on porewater [DIC], namely 1) $CaCO_3$-dissolution due to acidification of the sediment and 2) uptake of [DIC] by chemo-litho-autotrophs within the sediment.

Out of all the values reported in section 3.3.4 the most certain values were the ^{13}C and ^{15}N enrichment of the biomass. To reach similar assimilation rate constants for both carbon and nitrogen [DIC]0=20 mM was chosen (section 3.3.4.4). However, [DIC]0 could in fact be lower or higher, leading to two cases: 1) [DIC]0 is such that $\frac{C-ARC}{N-ARC}<1$ and 2) [DIC]0 is such that $\frac{C-ARC}{N-ARC} > 1$. The separating line between the scenario`s was [DIC]0=20 mM. Below [DIC]0=20 mM, $\frac{^{13}\mathrm{C-E(pw)}}{^{15}\mathrm{N-E(pw)}}$ was lower than 3.6, suggesting preferential nitrogen uptake, and, above [DIC]0= 20 mM, carbon would preferentially be taken up.

Calculation of organic carbon uptake for varying [DIC]0

Here focus was placed on case 1 as this seemed to be most relevant for cable bacteria. In a previous stable-isotope labelling experiment it was observed that reduced organic carbon compounds were preferentially taken up over DIC.[12] The uptake of unlabeled reduced organic carbon would lead to an observed case of $\frac{C-ARC}{N-ARC}<1$ because unlabeled substrates will not contribute to biomass` enrichment but do quench the need for carbon. Effectively, this would result in a lower effective enrichment of the porewater`s available carbon pool. To address uptake of unlabeled reduced organic carbon (C_{red}) a factor was added to the ^{13}C-E(pw) calculation (appendix X), which was now called $^{13}C\text{-}E_{effective}$. With TLV as the total porewater volume as a function of extent of diffusion (appendix X) the following calculation could be made:

$$^{13}C\text{-}E_{effective}=\frac{^{13}C\ of\ available\ carbon}{total\ amount\ of\ available\ carbon}=\frac{^{13}C\ (pw)}{Ctot}=\frac{TLV*[DIC]*^{13}\mathrm{C-E(pw)}+\mathrm{TLV}*[\mathrm{Cred}]*^{13}\mathrm{C-E(bg)}}{TLV*([DIC]+[Cred])}.$$

(divided by TLV and [DIC](both as calculated for fixed extent of diffusion as in appendix X):

$$^{13}\text{C-E}_{\text{effective}}=\frac{^{13}\text{C}-\text{E(pw)}+(\frac{[\text{Cred}]}{[DIC]}-)*^{13}\text{C}-\text{E(bg)}}{1+(\frac{[Cred]}{[DIC]})}.$$

^{13}C-E(bm)=mean ^{13}C-enrichment of filament A (0.0321)
^{13}C-E(BM)t=0=^{13}C-enrichment of filament A at the start of incubation (0.01)
^{15}N-E(BM)=mean ^{15}N-enrichment of filament A (0.01)
^{15}N-E(BM)t=0=^{15}N-enrichment of filament A at the start of incubation (0.0037)
^{15}N-E(pW)= the ^{15}N-enrichment of porewater at 1.5 cm diffusion (0.055):

This term can be introduced into the calculation of C-ARC to calculate the ratio of $\frac{\text{Cred}}{\text{DIC}}$ that would be required to result in equal assimilation rate constants and thus arrive at $\frac{\text{C}-\text{ARC}}{\text{N}-\text{ARC}}$=1. For [DIC]0=20 mM no reduced organic carbon would have to be taken up, as mentioned, because C-ARC and N-ARC were already nearly equal. Here an example calculation is shown for an extent of diffusion of 1.5 cm and [DIC]0=10 mM. For such a case the theoretical $\frac{^{13}\text{C}-\text{E(pw)}}{^{15}\text{N}-\text{E(pw)}}$ would be 5.7 (figure 21B), and assuming equal ARCs the ^{13}C-E$_{,\text{effective}}$ could be calculated.

$$5.7=\frac{C-ARC}{N-ARC}=\frac{\frac{^{13}\text{C}-\text{E(BM)}-\ ^{13}\text{C}-\text{E(BM)t=0}}{^{13}\text{C}-\text{E}(effective)-\ ^{13}\text{C}-\text{E(BM)t=0}}}{\frac{^{15}\text{N}-\text{E(BM)}-\ ^{15}\text{N}-\text{E(BM)t=0}}{^{13}\text{N}-\text{E}(pw)-\ ^{15}\text{N}-\text{E(BM)t=0}}}. \rightarrow {}^{13}\text{C-}_{\text{Epw,effective}}=0.0461$$

So, therefore, from equation 24, with ^{13}C-FA(pw)=0.319 for 1.5 cm diffusion (figure 21A),

$$\frac{[\text{Cred}]}{[DIC]}=\frac{^{13}\text{C}-\text{E}(pw,effective)-\ ^{13}\text{C}-\text{E(pw)}}{^{13}\text{C}-\text{E(bg)}-\ ^{13}\text{C}-\text{E}(pw,effective)}=0.89.$$

For the here calculated case 45% of the carbon taken up would then be from another source than the labeled DIC.

From this analysis it was observed that with increasing initial [DIC]0 the amount of organic carbon being taken up was decreased. Within Rattekaai sediment a [DIC]0 range of 15-30 mM was expected, for which a maximum $\frac{[\mathrm{Cred}]}{[DIC]}$ of 0.5 was found (figure 27). Thus, at most a third of the carbon taken up would not be DIC. Furthermore, within the range of [DIC]0 for Rattekaai sediment, variability in $\frac{[\mathrm{Cred}]}{[DIC]}$ was rather small and very close to 0. Therefore, for the most likely conditions the majority of carbon taken up by cable bacteria would be DIC.

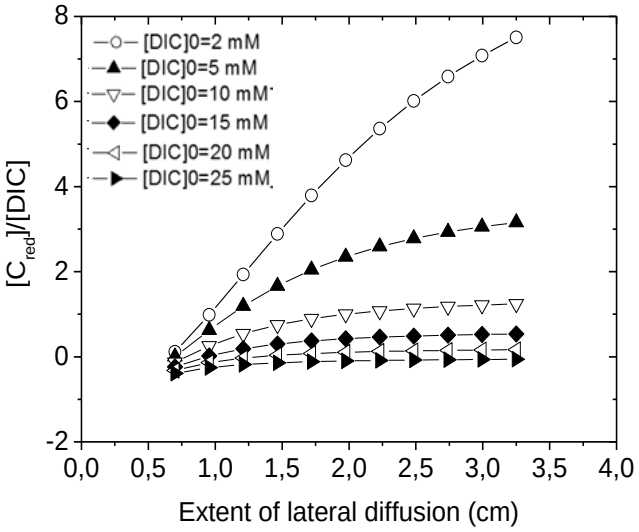

Figure 27. Calculation of the ratio of taken up organic carbon proportional to [DIC] for several [DIC]0 and the extent of lateral diffusion.

4. Discussion

4.1 General development characteristics

To monitor development, two indicators were employed that came directly from micro-sensor profiles: the global pH minimum and suboxic zone length. Based on these parameters, peak activity was observed in the cores between day 14 and 45. This corresponded well to incubation experiments in literature. In Schauer et al. 2014 a maximum in oxygen use by cable bacteria was observed on day 14 and cable bacterial density peaked just after this, around day 21.[11] Interestingly, suboxic zone length in their experiment reached a maximum much later, on day 53, which resembled the behavior of core 3 and 4 in the here presented experiments (figure 9).[11] Another oxic core incubation, in Rao et al. 2016, yielded similar results, with peak activity occurring between day 14 to 35 after the start of incubation. On day 71 a decline in both sulfide appearance depth and pH minimum was observed.[24] Although these sediments came from different sources and, therefore, likely had a different geochemical make-up, the cable bacterial development was more or less similar. This illustrates the great power cable bacteria have to employ their surroundings in service of their own growth pattern.

Another growth-characteristic observed in this study was the coupling between the suboxic zone length and the global pH minimum during growth periods. When a lot of resources were available to cable bacteria, as in the start of the incubation, activity is high, which will lead to production of protons and thus lower pH and subsequently lead to FeS-dissolution. Coinciding with increased availability of sulfide there will be growth, allowing for expansion of the suboxic zone, and, thus, pH and suboxic zone length exhibited coupling during growth periods (figure 10).

On the contrary, when activity decreased, suboxic-zone-length-decrease and pH-minimum-increase were out of sync and coupling was lost (figure 10). Apparently, suboxic zone length could be maintained for some time with an increasing pH or vice versa. Interestingly, for older cores, incubated for over 50 days, more and more disparity in our activity indicators was observed. For instance, the core used in the stable-isotopic labeling had incubated for 120 days, but, despite the long incubation time, a considerable suboxic zone remained. This was in stark contrast to all the core incubations cited in literature.[2,10–12,24] Also, in literature, incubation times exceeding 50 days are rarely performed. This could have contributed to the creation of a dogma that incubated cable bacterial populations always exhibit crash-and-boom-like life-cycles. Possibly, long-term incubations could provide clues into conditions underlying occurrence of theoretically possible stable cable bacteria populations.[2,52]

4.2 Direct consumption rate measurements: method assessment

4.2.1 Impact of anoxia on sulfide dynamics and the FeS^0 equilibrium

In this study a new method to measure rate of sulfide consumption by cable bacteria was presented. This method aimed to inhibit sulfide consumption of cable bacteria, by applying anoxia in the overlying water, thereby breaking the cryptic sulfur cycle. This results in an immediate increase in [ΣH_2S], which is produced by sulfate reduction and FeS dissolution. Contrary to expectation, the absolute increase in concentration was observed to be rather limited. Based on literature research, this was caused by the dissolution mechanism, which occurs via the pH-independent pathway. In the pH-independent pathway, [Fe^{2+}] and [H_2S] reach an equilibrium with [FeS^0] and [H^+] at low micro-molar [ΣH_2S] and subsequently dissolution comes to a halt.[48] This pathway would actually be the dominant dissolution pathway in all sediments with pH>5.3, which would be the case for almost all electrified sediments. Consequently, in some studies the dissolution of FeS, induced by cable bacteria, has been inaccurately given as the pH-dependent mechanism ($FeS\ (s)+2H^+ \rightarrow Fe^{2+}+H_2S$).[10]

Although this study has been the first time anoxia was applied with the previously mentioned aim in mind, anoxic perturbation has been performed before. For instance, in Nielsen et al. 2010, cyclic anoxic perturbation was applied for 10 hour-stretches and, as their main conclusion, they observed that concomitantly with anoxic overlying water the euxinic front had become more shallow.[2] Interestingly, they did not report [ΣH_2S] higher than 1 µM within the suboxic zone, which, on the contrary, was observed in this study for every perturbation experiment. On the basis of the modelling performed in this study, this could be caused by a high [Fe^{2+}] in the incubated sediment of Nielsen et al. 2010. Due to the high [Fe^{2+}], [ΣH_2S] would then never exceed their chosen euxinic cut-off limit of 1 µM. The possibly observed minor increase could then have been discarded as an artefact. Although not synchronously measured, [Fe^{2+}] within the Rattekaai sediment in this study must have remained sufficiently low to allow observation of the [ΣH_2S] increase.

4.2.2 Evaluation of the anoxic perturbation model

4.2.2.1 Validity and predictive power of the anoxic perturbation model

The model presented in this study was not the first time the geochemistry of electrified sediment was modelled but it was the first, to our knowledge, dynamic model for anoxic perturbation.[9] Using the model, development of [ΣH_2S](t)] was fitted well. The experimental pH could however not be accurately described by an exponential curve. Probably this was caused by the assumption that the proton consumption: ΣH_2S-increase was entirely determined by the iron dissolution mechanism. While, in fact, sulfate reduction would have been responsible for some of the H_2S-increase as well. Thereby, the experimentally observed proton consumption: ΣH_2S-increase was different in experimental situations than one solely based on FeS^0-dissolution.

On longer time scales an increasing discrepancy between the modelled concentration and the actual concentration was observed. To accurately model long-term effects, transport and precipitation equations for H_2S and Fe^{2+} and microbial influence on pH, would have to be added to the model. Description of these long term processes would however defeat the purpose of the limited scope the presented model had within the context of this study.

Although allowing for good fits one of the main drawbacks was that the initial rate could not be fitted. In these still preliminary experiments, [Fe^{2+}] and [FeS^0] within the porewater were not experimentally determined: [FeS^0] was calculated on the basis of a literature value and the [Fe^{2+}] was determined by fitting.[47] This limited the predictive power for the parameter of main interest, being the initial slope of H_2S-increase. This leads to an inability to correct the possible error in the experimental determination of initial rate.

Interestingly, as far as we could find, in literature no information was found on the rate constant for the ionization reaction of FeS^0. Investigation of this rate constant could however be of great use. Because, in this way FeS^0-dissolution rate, assuming [ΣH_2S] was negligible, could be directly calculated, knowing only pH and [FeS^0], by means of: $k_{fw,dis}*[H^+]^x*[FeS^0]^y$ (in which x and y are the reaction orders of the species). In this way, the amount of sulfide released by means of FeS dissolution might be directly calculated from an oxic pH-profile. The amount of sulfide produced in sulfate reduction would however still require explicit investigation.

4.2.3 Quantitative assessment of the direct-rate measurement method

At peak activity, using the direct rate measurement method, an averaged total of 1.3 mmol $\Sigma H_2S *m^{-2}*d^{-1}$ was measured to be consumed within the suboxic zone. One week later this total had decreased by 30% to 1 mmol $\Sigma H_2S *m^{-2}*d^{-1}$. For both investigated cores this amount was rather similar. Unfortunately, no synchronous Fe^{2+}-depth profile was measured to distinguish between ΣH_2S from sulfate reduction and FeS dissolution. However, the maximum magnitude of the Fe^{2+}-flux in asynchronous Fe^{2+}-profiles far exceeded that of the sulfide consumption rate measured within the suboxic zone. Therefore, the cable bacterial populations in the Rattekaai sediment could depend greatly on FeS dissolution. Still, the maximum Fe^{2+}-flux was lower than other [Fe^{2+}]-fluxes in oxic incubation in literature.[10] Only the range observed in Rao et al 2016 was close (table 9).[24] Performing,

Apart from suboxic sulfide, a major part of consumed sulfide was delivered by diffusion from the euxinic zone. Interestingly, although being prepared from the same stock sediment, the amount of consumed sulfide that came from diffusion was markedly different. For core one, the majority of sulfide (62%) originated from euxinic influx, for core 2 this was just 28%. Still, percentage-wise, both these values were on the high side compared to the other reported oxic incubation experiments (table 9). This could be caused by sediment characteristics. Rattekaai sediment has high porewater sulfide concentrations (up to 8 mM); therefore, euxinic sulfide fluxes would generally be high.[36]

The total rates measured using the new technique were the lowest rates observed out of all oxic incubation experiments (table 8). The only oxic incubation experiment for which lower rates were observed was for Aarhus harbor sediment, as described by Nielsen et al. 2010.[2,52] Therefore, these low rates would not be entirely out of the ordinary and could have simply been a result of sediment characteristics. This was suggested by the maximum Fe^{2+}-flux but also by the magnitude of the sedimentary oxygen consumption. In this study the maximum O_2-flux was 18 $mmol*m^{-2}*d^{-1}$, whereas, for instance, in Vasquez et al. 2015, this flux was over 50 $mmol*m^{-2}*d^{-1}$.[12] To some extent the lower oxygen flux, and possibly the overall lower activity, might be a result of the relatively salt water used in this study. Because of this, oxygen concentrations in overlying water were just 235 µM in this study, compared to 285 µM in most literature studies.[11,24]

Based on the above, there were multiple indications that the investigated sediment has a lower potential sulfide release than most examples in literature. However, for a new method, validation of the results by other methods would be useful. Therefore, the possibility of underestimation by the method itself should not be neglected. Most other studies used the pH-peak in the oxic zone and the buffering capacity to calculate the amount of protons being produced and therewith the amount of sulfide consumed.[2,10–12] Unfortunately, the pH-peak method could not be employed for comparison with our method because pH-profiles in this study almost never exhibited the oxic zone pH-peaks.

Two possible reasons for this absence are: 1) incubation with large amounts of overlying water which would enhance diffusion of buffering compounds and therewith diminish build-up of alkalinity within the oxic zone and 2) cable bacteria might reduce O_2 directly in the water column rather than within the oxic zone of the sediment. Another study also did not observe the, supposedly, characteristic cable bacterial pH-peak and used [SO_4^{2-}] and [Fe^{2+}]-depth profiles to determine suboxic sulfide consumption.[24]

4.2.4 Indication for an underestimation of sulfide consumption rate

4.2.4.1 Presence of ferrous ions in the porewater

Although, based on oxygen and iron fluxes, activity of cable bacteria within Rattekaai-sediment might truly be lower than most sediments in literature, there were several indications that underestimation of the experimentally determined initial slope of [ΣH_2S]-increase could have occurred. From the modelling effort the most likely cause for underestimation would be the presence of high [Fe^{2+}] within the porewater, which, in theory, could have decreased rates even at [ΣH_2S] below detection limit. The extent to which this occurred remains unknown as data on [Fe^{2+}] and FeS^0 were not directly experimentally determined. Generally, it would however be expected that decreases in observed initial rate due to high [Fe^{2+}] would be soothed by a coincident low pH. Hereby increasing the [ΣH_2S] at which major decreases in rate would occur. As no experimental data was available on the true [FeS^0] (aq) and [Fe^{2+}] in the core it was hard to make a proper estimation of possible deviation that occurred by this mechanism.

4.2.4.2 Residual oxygen flux

Anoxia had been applied to the greatest possible extent, but, a minor amount of oxygen remained within the overlying water. Generally, this concentration was rather small, varying between 1%-8%. The corresponding flux, calculated for just one situation, was found to be 2.3 $mmol*m^{-2}*d^{-1}$, which was considerable relative to the total sulfide consumption. This would definitely have contributed to underestimation as some of the residual oxygen would be used in sulfide consumption. Even though, this was an unwanted artefact within the context of the direct-rate measurement, an interesting question arises with respect to competition between reoxidation process of [Fe^{2+}] and OM and oxygen consumption by cable bacteria. The direct-rate measurement method could be employed to investigate this, by gradually removing oxygen until an increase in [ΣH_2S] would be observed.

Table 9. Overview of sulfide metabolism and sulfate reduction measurements in oxic incubation cores and in-situ field studies. *For all incubation studies the maximum values were reported. usually around day 14. For in-field studies the warmest season was taken as these temperatures would come closest to R.T. All reported values were in the units mmol*m^{-2}*d^{-1}.*

Sulfide metabolism in oxic incubation experiments at peak activity						
Study		Fe^{2+}-SWI-flux	H_2S-diffusional	SO_4-Reduction	FeS-dissolution	H_2S_{total}
Rao et al. 2016[24]		1.7-3.4	0.48	3.4		3.8
Nielsen et al. 2012[10]		5.9	<1%	0.3	5.9	6.2
Schauer et al. 2014[31]		-	<30%	-		11
Vasquez et al. 2015[12]		-		9		9
Nielsen et al. 2010[2]	*Aarhus Bay*	-	0.5	9.2		9.7
	Aarhus Harbour	-	1.3	0.2		1.5
This study		**0.08-1.64**	**1.5**	**1.3**		**2.8**
Sulfide metabolism in in-situ sediments						
Van der Velde et al. 2016 [28]		0.8-1	<1%	2.1	1	3.1

Malkin et al 2014[22]	**Location**	**Coordinates**	**Time of year**	
	RSM, Oosterschelde the Netherlands Station 130 BCZ	N 51^0 26` 21"	June 2011	3.4
		E 04^0 10` 11"	February 2013	0.8
		N 51^0 16`13"	October 2011	3.1
		E 02^0 54`19"	March 2013	0.7
	MLG Holpervoet and Den Osse Basins, the Netherlands	N 51^0 46`24"	November 2011	3.1
		E 03^0 56`16"	January 2012	2.1
			February 2012	2.8
	OSF,the Netherlands	N 51^0 26`52"	May 2011	0.8

Sulfate reduction rates in the Scheldt		Sulfate reduction rate (mmol*m^{-2}*d^{-1})
Oenema 1990 [53](study used homogenized sediment)	*Eastern Scheldt, the Netherlands*	14 (winter) -68 (summer)
Baeyens et al. 2001[54]	*Ballastplaat, mudfat, Belgium*	10 (spring) -824 (summer)
Vasquez 2016[36]	***Rattekaai, the Netherlands***	**C-mineralization (majority with SO_4) 197**

4.2.5 Potential future usage of the direct rate-measurement

The method as presented in these preliminary experiments still requires some quantitative validation by independent measurements. Validation could be performed by comparison with other consumption rate determination such as via [Fe^{2+}]-depth profiles, accounting for sulfide from FeS-dissolution, sulfate reduction rate measurements and the oxic zone pH-peak method. If the quantative results obtained using this method were to be more or less in line with one another, an in-depth analysis would be possible of sulfide consumption. The main advantage of the direct-rate measurement as presented here would be to determine sulfide consumption without sacrificing the core. Furthermore, no assumptions regarding buffering capacity, which underly the pH-peak method, would be required. This could greatly increase the accuracy in determination of sulfide consumption.

If the method was found to be quantitatively accurate one of the main mysteries in cable bacteria might be solvable, namely, whether cable bacteria are able to fully oxidize sulfide to sulfate.[12,28] A possible way to do this, would be by comparing the proton consumption, based on the pH-peak, with the sulfide consumption, as determined by the direct rate measurement. If cable bacteria would indeed only be able to oxidize sulfide to elemental sulfur, only 2 mol H^+ would be taken up within the oxic zone for every mol of sulfide consumed. ($H_2S^- \rightarrow S^0 + 2\ H^+ + 2\ e^-$ and $½\ O_2 + 2\ H^+ + 2\ e^- \rightarrow H_2O$). However, if the chemo-litho-autotrophic community would indeed use a linking method to rid themselves of all electrons, unfortunately, the pH-peak relation would in such a case likely be the same: ($S^0 + 4\ H_2O \rightarrow SO_4^{2-} + 4\ H^+ + 6\ e^-$ and $1½\ O_2 + 6\ H^+ + 6\ e^- \rightarrow 3\ H_2O$) 8 H^+:1 H_2S.

In literature evaluation of the pH-peak method, by Fe^{2+}-depth profiles and sulfate reduction rates, has been performed only once.[10] For this particular example, within experimental uncertainty, full oxidization was observed. Still, it would be good to validate these experiments for sediments of differing composition, which could also harbor different microbial communities.

4.3 Carbon metabolism and metabolic activity patterns within filaments

Apart from this study, the only direct study on carbon metabolism of cable bacteria has been that of Vasquez et al. 2015.[12] In this paper some interesting observations were made that we will compare with the data and observations in this study: 1) *oxic zone cells showed increased uptake over suboxic cells* and 2) *cable bacteria preferentially take up reduced organic carbon.* Although the experimental set-up was rather similar, some differences should be mentioned: 1) incubation time, which was just 21 days in Vasquez et al., but 120 days in this study, 2) sediment in this study came from Rattekaai whereas in Vasquez et al. 2015 the sediment came from lake Grevelingen and 3) only enriched DIC was supplied to the cable bacteria in this study

4.3.1 Differential metabolic activity and homogenous carbon uptake within the filament

One of the most notable observations within this study has been the absence of any activity for cells residing in the oxic zone. This was almost the exact opposite pattern of Vasquez et al. 2015, in which oxic cells exhibited a two-fold higher activity.[12] The cause for this great discrepancy was not easily deduced. The main conclusion drawn by Vasquez et al. 2015 on this subject, was that there was a difference in energetic yields of the half-reactions, which was reflected by the pattern of carbon uptake within the filament. We, on the other hand, would have to conclude that there was a total absence of energetic yield for the cells within the oxic zone. Oxic zone cells did not fix any DIC and therefore merely seem to serve to reduce oxygen as efficiently as possible for the electron conducting filament below.

This hints towards specialized functions for the oxic-zone-cells within the filament. Morphologically, cell specialization was not observed, but, possibly, differences would be observable on a transcriptional level. A transcriptional response was previously also suggested to adjust the efficiency of oxygen reduction under changing oxygen conditions.[34] Another interesting observation with respect to cellular cooperation was the rather homogenous distribution observed for all active filaments. Such a homogenous spread would be hard to envision if all cells fended for themselves and would individually create and use as much reduction potential as possible. Possibly, the individual cells making up the filament were better capable of cooperation than previously supposed. An interesting question in this respect is whether some form of intra-filament communication occurs, as in cyanobacterial cells, or, that the observed filament patterns rely on an uncoordinated, biochemical mechanism.[55]

4.3.2 Cable bacteria and autotrophy

Unfortunately, due the absence of certain data, the ^{13}C-fractional abundance of the porewater could not be entirely constrained. However, for the most likely range of [DIC]0 in the Rattekaai sediment, 15-30 mM[36], convergence towards a rather similar ratio of ^{13}C-FA:^{15}N-FA was observed. Based on this it seemed that hardly any or even no reduced organic carbon was taken up by the cable bacteria. Although we did not perform a stable-isotope labelling with reduced organic carbon, combined with observations in Vasquez et al 2015, it would seem that cable bacteria have considerable metabolic flexibility in choosing their C-source.[12] Now, combined with the here presented observations, cable bacteria seem able to switch metabolic modus operandi entirely, depending on the changing environmental conditions.

Possibly, for natural settings with a high sedimentation rate, autotrophy would not be the most favourable metabolism.[22,23] Discovery of cable bacteria as autotrophs was however interesting because there are reports in literature of a strong correlation between cable bacteria activity and that of chemo-litho-autotrophs.[12,28] Suggesting some sort of synergetic mechanisms to be present between cable bacteria and the chemo-litho-autotrophic community. One of the suggested synergetic mechanisms was the usage of the electron-conducting-filament for deposition of excess electrons produced in sulfide oxidation by chemo-litho-autotrophs.[12,28] Instead of the exotic linking, however, possibly a more straightforward synergetic mechanism would also be the lowering of pH. From literature two phenomena induced by low pH would work to the benefit of autotrophic cable bacteria, being: 1) the release of DIC stored in calcium carbonates,[9,10,28] and, 2) a decrease in the required reduction potential of rate-limiting carboxylation and carbonyl reduction steps in carbon-fixation pathways.[56,57]

4.3.3 Influence of long incubation time on experimental results

As comes to the forth from the text above, there was a stark difference in experimental results between Vasquez 2015 et al. and the here presented. The most obvious cause for these differences would be the vastly different incubation times. Within the Rattekaai and eastern Scheldt sediment there is a high rate of sulfate reduction (table 8, bottom part), which would most likely have greatly altered the OM content of the sediment over the time scales of incubation. The absence of organic carbon uptake observed in this study could then be explained by depletion of this source all together. Consequently, cable bacteria would then be able to survive almost entirely on DIC, but only do so when required by the environment.

Another consequence of long incubation times would be a depletion of suboxic zone sulfide-sources, which was also suggested by a direct rate-measurement performed after 142 days of incubation (appendix XVII). Therefore, it would seem that the cable bacteria populations at time of labelling only relied on diffusional sulfide to obtain reduction equivalents. Possibly under situations of low sulfide availability the filament behaves in a more communal way, spreading reduction potential more evenly along the filament. Based on these observations, another interesting question arises as to why cable bacteria would maintain the suboxic zone without a gain in sulfide from FeS. Maintaining a large filament comes at a large cellular maintenance cost but it then would seems this could be offset by the gained monopoly on oxic sulfide oxidation.

5. Conclusions and outlook

In this study, preliminary experiments towards the development of a new sulfide consumption rate measurement method were presented. The technique allowed to directly measure sulfide consumption at the exact moment in time without requiring destruction of the incubated cores. Furthermore, no assumptions were used that relate proton consumption to sulfide oxidation. Therefore, this method might be able to increase accuracy in determining the suboxic sulfide consumption. The measured values presented here remain preliminary for now as quantative validation using independent methods was not performed in this study. Sulfate reduction rate measurement and fluxes from Fe^{2+}-depth profiles, should be used to independently determine suboxic zone sulfide consumption. These values could then be compared to values obtained using the direct-rate measurement and subsequently with the pH-peak method.

In the stable isotopic labelling experiments, multiple interesting observations were made that were in stark contrast to previous ideas about cable bacterial carbon metabolism. For one, they suggested that cable bacteria were able to switch to a predominantly autotrophic life-style, increasing even further the observed metabolic flexibility of cable bacteria. Secondly, oxic cells were observed to not take up any DIC thereby suggesting that these cells would solely reduce oxygen, akin to differential cell functioning within filaments. Thirdly, a surprisingly homogenous uptake was observed throughout the filament that was not observed in earlier studies. This could suggest that cable bacteria seem to have ways, actively or passively, to possibly share reduction potential with one another.

Although a plentitude of data and observations could be presented in this report one of the main weaknesses of the study, as it is now, was the asynchronous nature of the experimental efforts. To a large extent this was the result of time required to familiarize with the experimental methods. However, if a more concerted effort would be made, involving all the available experimental methods, some of the main question regarding cable bacterial metabolism could be elucidated namely:

1) Do cable bacteria fully oxidize sulfide?

The approach would be to relate proton consumption, as determined by the pH-peak method, to the sulfide consumption, as measured by the direct-rate measurement. If a ratio of 2:1 would be observed, cable bacteria only oxidize sulfide to elemental sulfur. However, if the chemo-litho-autotrophic community links up to the filament and disposes of all its electron there would not be an alteration in the sulfide to proton consumption ratio compared to cable bacteria, fully oxidizing sulfide.

2) Were the oxic cells truly specialized in transferring electrons and incapable of DIC fixation?

To make sure the oxic cells were exposed to labeled substrate, only a shallow layer of overlying water on top of the core could be labeled. Thus, diffusion, passing the oxic cells, would be required in order for labeled carbon to reach the supposedly suboxic carbon-fixing cells. Now, oxic cells would be at a positional advantage to take up DIC over the suboxic zone cells. If in such a case the same uptake-pattern was observed as here, it would be highly unlikely that oxic cells of the cable bacteria filament produce reduction potential.

3) Are cable bacteria primarily heterotrophic or autotrophic?

To answer this question a second stable-isotope experiment should be performed but this time using labelled reduced organic carbon (propionate). An idea could also be to use ^{14}C-DIC and ^{13}C-propionate and perform a direct competition experiment. This will shed light on the carbon source preferred by cable bacteria.

4) How energetically efficient is the growth of cable bacteria?

As in 3) stable-isotope labelling would be required but, now, should be combined with fluorescent in-situ hybridization (FISH) to estimate the amount of cable bacterial biomass within the sediment.[11,12] Knowing the cable bacterial biomass allows to calculate the sedimentary volumetric carbon fixation rate. Next to this, a biomass-specific sulfide consumption rate could be determined. Relating the two would result in the data required to calculate the amount of carbon taken up for every sulfide oxidized, and, thus the energetic efficiency of growth could be assessed.[58]

After the quantitative results of the direct rate measurement would be validated, an efficient experimental set-up could allow nearly simultaneous measurement of sulfide consumption, cable bacterial biomass and carbon-uptake rate within one core at one point in time. This will allow to determine efficiency of growth on both DIC and reduced organic carbon. Thereby, question 3 and 4 could be answered and if a pH-peak were to be present possibly even question 1.

In this study first steps were made towards a new non-destructive technique to measure sulfide consumption rate. With regard to carbon metabolism we observed that cable bacteria might be capable of even greater metabolic flexibility than previously supposed. On top of this, multiple indications were present that cells function within the context of the entire filament rather than being a mere electron-conducting link in the chain. Although most of the results presented here still await replication, some intriguing observations were made that could once more, change the way we look at cable bacteria.

6. References

1. Trojan, D. *et al.* A taxonomic framework for cable bacteria and proposal of the candidate genera Electrothrix and Electronema. *Syst. Appl. Microbiol.* **39,** 297–306 (2016).

2. Nielsen, L. P., Risgaard-Petersen, N., Fossing, H., Christensen, P. B. & Sayama, M. Electric currents couple spatially separated biogeochemical processes in marine sediment. *Nature* **463,** 1071–1074 (2010).

3. Pfeffer, C. *et al.* Filamentous bacteria transport electrons over centimetre distances. *Nature* **491,** 218–221 (2012).

4. Robert A. Berner and Joseph T. Westrich. Bioturbation and the early diagenesis of carbon and sulfur. *Am. J. Sci.* **285,** 193–206 (1985).

5. Middelburg, J. J. & Levin, L. A. Coastal hypoxia and sediment biogeochemistry. *Biogeosciences Discuss.* **6,** 3655–3706 (2009).

6. Marzocchi, U. *et al.* Electric coupling between distant nitrate reduction and sulfide oxidation in marine sediment. *ISME J.* **8,** 1682–1690 (2014).

7. Risgaard-Petersen, N., Damgaard, L. R., Revil, A. & Nielsen, L. P. Mapping electron sources and sinks in a marine biogeobattery. *J. Geophys. Res. G Biogeosciences* **119,** 1475–1486 (2014).

8. Damgaard, L. R., Risgaard-Petersen, N. & Nielsen, L. P. Electric potential microelectrode for studies of electrobiogeophysics. *J. Geophys. Res. G Biogeosciences* **119,** 1906–1917 (2014).

9. Meysman, F. J. R., Risgaard-Petersen, N., Malkin, S. Y. & Nielsen, L. P. The geochemical fingerprint of microbial long-distance electron transport in the seafloor. *Geochim. Cosmochim. Acta* **152,** 122–142 (2015).

10. Risgaard-Petersen, N., Revil, A., Meister, P. & Nielsen, L. P. Sulfur, iron-, and calcium cycling associated with natural electric currents running through marine sediment. *Geochim. Cosmochim. Acta* **92,** 1–13 (2012).

11. Schauer, R. *et al.* Succession of cable bacteria and electric currents in marine sediment. *ISME J.* **8,** 1314–1322 (2014).

12. Vasquez-Cardenas, D. *et al.* Microbial carbon metabolism associated with electrogenic sulphur oxidation in coastal sediments. *ISME J.* **9,** 1966–1978 (2015).

13. Weijden, C. H. van der. Surface chemistry of disordered mackinawite (FeS). *Geochim. Cosmochim. Acta* **69,** 3469–3481 (2005).

14. Morgan, B. & Lahav, O. The effect of pH on the kinetics of spontaneous Fe(II) oxidation by O2 in aqueous solution - basic principles and a simple heuristic description. *Chemosphere* **68,** 2080–2084 (2007).

15. Seitaj, D. *et al.* Cable bacteria generate a firewall against euxinia in seasonally hypoxic basins. *Proc. Natl. Acad. Sci.* **112,** 13278–13283 (2015).

16. Nielsen, L. P. Ecology: Electrical Cable Bacteria Save Marine Life. *Curr. Biol.* **26,** R32–R33 (2016).

17. van de Velde, S., Callebaut, I., Gao, Y. & Meysman, F. J. R. Impact of electrogenic sulfur oxidation on trace metal cycling in a coastal sediment. *Chem. Geol.* **452,** 9–23 (2017).

18. Sulu-Gambari, F. *et al.* Cable Bacteria Control Iron-Phosphorus Dynamics in Sediments of a

Coastal Hypoxic Basin. *Environ. Sci. Technol.* **50,** 1227–1233 (2016).

19. Müller, H. *et al.* Long-distance electron transfer by cable bacteria in aquifer sediments. *ISME J.* **10,** 2010–2019 (2016).

20. Burdorf, L. D. W. *et al.* Long-distance electron transport occurs globally in marine sediments. *Biogeosciences Discuss.* **0,** 1–35 (2016).

21. Burdorf, L. D. W., Hidalgo-Martinez, S., Cook, P. L. M. & Meysman, F. J. R. Long-distance electron transport by cable bacteria in mangrove sediments. *Mar. Ecol. Prog. Ser.* **545,** 1–8 (2016).

22. Malkin, S. Y. *et al.* Natural occurrence of microbial sulphur oxidation by long-range electron transport in the seafloor. *ISME J.* **8,** 1843–1854 (2014).

23. Lipsewers, Y. A. *et al.* Impact of Seasonal Hypoxia on Activity and Community Structure of Chemo-litho-autotrophic Bacteria in a Coastal Sediment. *Appl. Environ. Microbiol.* **83,** AEM.03517-16 (2017).

24. Rao, A. M. F., Malkin, S. Y., Hidalgo-Martinez, S. & Meysman, F. J. R. The impact of electrogenic sulfide oxidation on elemental cycling and solute fluxes in coastal sediment. *Geochim. Cosmochim. Acta* **172,** 265–286 (2016).

25. Holmkvist, L., Ferdelman, T. G. & Jørgensen, B. B. A cryptic sulfur cycle driven by iron in the methane zone of marine sediment (Aarhus Bay, Denmark). *Geochim. Cosmochim. Acta* **75,** 3581–3599 (2011).

26. Kappler, A. & Bryce, C. Cryptic biogeochemical cycles: unravelling hidden redox reactions. *Environ. Microbiol.* **19,** 842–846 (2017).

27. Boschker, H. T. S., Vasquez-Cardenas, D., Bolhuis, H., Moerdijk-Poortvliet, T. W. C. & Moodley, L. Chemoautotrophic carbon fixation rates and active bacterial communities in intertidal marine sediments. *PLoS One* **9,** (2014).

28. van de Velde, S. *et al.* The impact of electrogenic sulfur oxidation on the biogeochemistry of coastal sediments: A field study. *Geochim. Cosmochim. Acta* **194,** 211–232 (2016).

29. Walker, D. J. F. *et al.* Electrically conductive pili from pilin genes of phylogenetically diverse microorganisms. *ISME J* (2017).

30. Madigan, Michael, Martinko, John, Stahl, David, Clark, D. in *Biology of Microorganisms* 381–382 (2012).

31. Schauer, R. *et al.* Succession of cable bacteria and electric currents in marine sediment. *Isme J.* **8,** 1314–1322 (2014).

32. Laanbroek, H. J. & Pfennig, N. Oxidation of short-chain fatty acids by sulfate-reducing bacteria in freshwater and in marine sediments. *Arch. Microbiol.* **128,** 330–335 (1981).

33. Widdel, F. & Pfennig, N. Studies on dissimilatory sulfate-reducing bacteria that decompose fatty acids II. Incomplete oxidation of propionate by Desulfobulbus propionicus gen. nov., sp. nov. *Arch. Microbiol.* **131,** 360–365 (1982).

34. Malkin, S. Y. & Meysman, F. J. R. Rapid redox signal transmission by 'cable bacteria' beneath a photosynthetic biofilm. *Appl. Environ. Microbiol.* **81,** 948–956 (2015).

35. Pallud, C. & Van Cappellen, P. Kinetics of microbial sulfate reduction in estuarine sediments. *Geochim. Cosmochim. Acta* **70,** 1148–1162 (2006).

36. Cardenas, D. V. Bacterial Chemoautotrophy in Coastal Sediments. (2016).

37. Cragin, J. H. & Foley, B. T. *Sample digestion and drying techniques for optimal recovery of mercury from soils and sediments*. (1985).

38. Fondriest enviromental inc. Dissolved Oxygen." Fundamentals of Environmental Measurements. (2013). Available at: http://www.fondriest.com/environmental-measurements/parameters/water-quality/dissolved-oxygen/.

39. Jeroschewski, P., Steuckart, C. & Ku, M. An Amperometric Microsensor for the Determination of H 2 S in Aquatic Environments. *Anal. Chem.* **68,** 4351–4357 (1996).

40. Soetaert, K., Petzoldt, T. & Meysman, F. marelac : Tools for Aquatic Sciences. *http://CRAN.R-project.org/package=marelac* (2010).

41. Boudreau, B. P. *Diagenetic Models and their Implementation*. (1996).

42. Stookey, L. L. Ferrozine-a new spectrophotometric reagent for iron. *Anal. Chem.* **42,** 779–781 (1970).

43. Viollier, E., Inglett, P. W., Hunter, K., Roychoudhury, a N. & Van Cappellen, P. The Ferrozine Method Revisited: Fe (II)/Fe (III) Determination in Natural Waters. *Appl. Geochemistry* **15,** 785–790 (2000).

44. Solórzano, L. Determination of ammonia in natural waters by the phenolhypochlorite methods. *Limnol. Oceanogr.* **14,** 799–801 (1969).

45. Tzollas, N. M., Zachariadis, G. A., Anthemidis, A. N. & Stratis, J. A. A new approach to indophenol blue method for determination of ammonium in geothermal waters with high mineral content. *Int. J. Environ. Anal. Chem.* **90,** 115–126 (2010).

46. Polerecky, L. *et al.* Look@NanoSIMS - a tool for the analysis of nanoSIMS data in environmental microbiology. *Environ. Microbiol.* **14,** 1009–1023 (2012).

47. Rickard, D. The solubility of FeS. *Geochim. Cosmochim. Acta* **70,** 5779–5789 (2006).

48. Rickard, D. & LutherIII, G. W. Chemistry of Iron Sulfides. *Chem. Rev.* **44,** 514–562 (2007).

49. Ohfuji, H. & Rickard, D. High resolution transmission electron microscopic study of synthetic nanocrystalline mackinawite. *Earth Planet. Sci. Lett.* **241,** 227–233 (2006).

50. Pankow, J.J and Morgan, J. F. Dissolution of Tetragonal Ferrous Sulphide (Mackinawite) in Anoxic Aqueous Systems. 2. Implications for the Cycling of Iron, Sulfur, and Trace Metals. *Environ. Eng. Sci.* **14,** (1980).

51. Hofmann, A. F., Soetaert, K., Middelburg, J. J. & Meysman, F. J. R. AquaEnv: An Aquatic Acid–Base Modelling Environment in R. *Aquat. Geochemistry* **16,** 507–546 (2010).

52. Nielsen, Lars Peter; Risgaard-Petersen, N. Rethinking Sediment Biogeochemistry After the Discovery of Electric Currents. *Annu. Rev. Mar. Sci.* **7,** 425–442 (2015).

53. Oenema, O. Sulfate reduction in fine-grained sediments in the Eastern Scheldt , southwest Netherlands. *Biogeochemistry* **9,** 53–74 (1990).

54. Panutrakul, Suwanna, Monteny, Frank, Baeyens, W. Seasonal Variations in Sediment Sulfur Cycling in the Ballastplaat Mudflat , Belgium. *Estuaries* **24,** 257–265 (2001).

55. Kumar, K., Mella-herrera, R. A. & Golden, J. W. Cyanobacterial Heterocysts. *Cold Spring Harb. Perspect. Biol.* 1–19 (2010).

56. Bar-Even, A., Flamholz, A., Noor, E. & Milo, R. Thermodynamic constraints shape the structure of carbon fixation pathways. *Biochim. Biophys. Acta - Bioenerg.* **1817,** 1646–1659 (2012).

57. Bar-Even, A., Noor, E. & Milo, R. A survey of carbon fixation pathways through a quantitative lens. *J. Exp. Bot.* **63,** 2325–2342 (2012).

58. Klatt, J. M. & Polerecky, L. Assessment of the stoichiometry and efficiency of CO(2) fixation coupled to reduced sulfur oxidation. *Front. Microbiol.* **6,** 484 (2015).

59. Polerecky, L. Mprplotter. (2008). Available at: http://microsen-wiki.net/doku.php/microprofiling:mprplotter_howto.

Appendices

Appendix I. Lateral variability of geochemical micro-sensor depth-profiles in incubated sediment.

Micro-sensor profiles were measured at different locations in the core. As can be observed variability for H_2S is only observed in the [ΣH_2S] of the euxinic zone. Variability does not influence the depth of the euxinic front and therefore variability does not influence the length of the suboxic zone. In figure i-A there was some variability in pH in the shallow part of the sediment. The absolute pH-minimum however was unaffected by this.

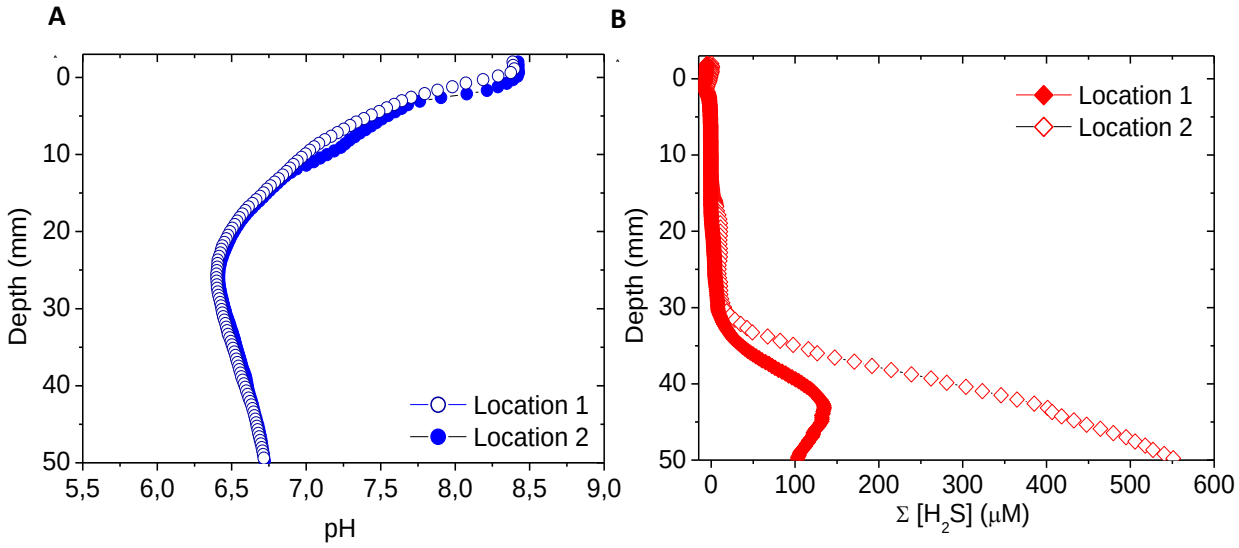

Figure i. micro-sensor depth profile measured at two distinct locations in one core to assess lateral heterogeneity. Panel A: pH. Panel B: H_2S

Appendix II. indicator development for cores incubated at the same time point.

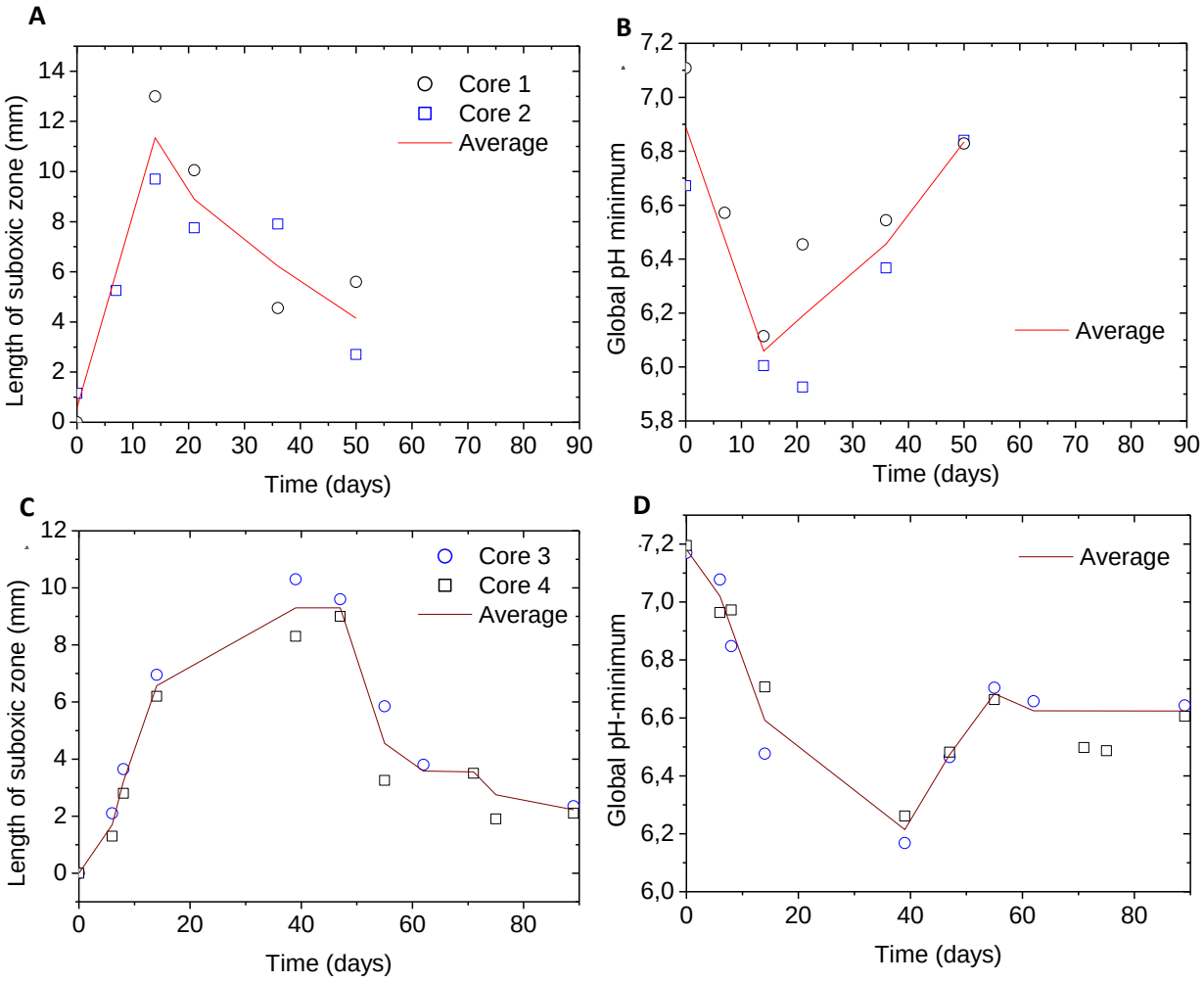

Figure ii. Panel A: development of the length of suboxic zone for core 1 and 2. Panel B: Global pH-minimum development core 1 and 2. Panel C: development of the length of the suboxic zone for core 3 and 4. Panel D: Global pH-minimum development core 3 and 4.

Because of averaging the intense and transient peak in individual peaks was not easily observed in figure 9. To show that this behavior does arise in most core figure ii is presented. The main data from figure 9 was built up from five cores. with three incubation dates. Interestingly, there is a much stronger similarity in core development between cores incubated at the same point in time than between cores at different time points. To explain this, there could either be an alteration over time of stock sediment, differential sample handling, although efforts were made to limit this, or a combination of both.

Appendix III. Calibration curves for [Fe^{2+}] and [NH_4]

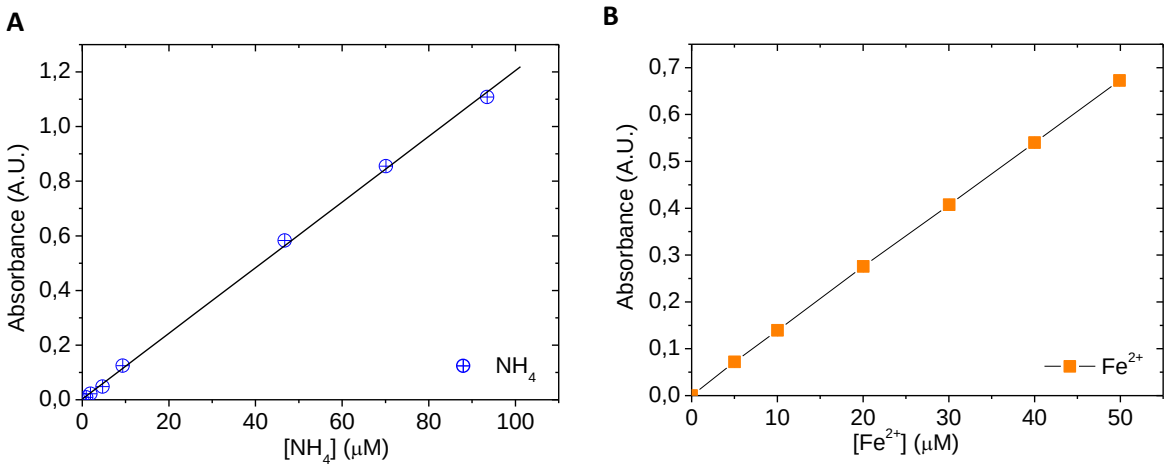

Figure iii. Calibration lines for colorimetric determination of ammonium and ferrous iron. Panel A: Ammonium (*Y=0.0041x, R^2=0.9982)* **Panel B: Ferrous iron.** *(y= 0.0134x,R^2 = 0.9999) These lines serve as an example calibration lines as new lines were made for every iron and ammonium depth profile determination.*

Appendix IV. Picture of incubated core.

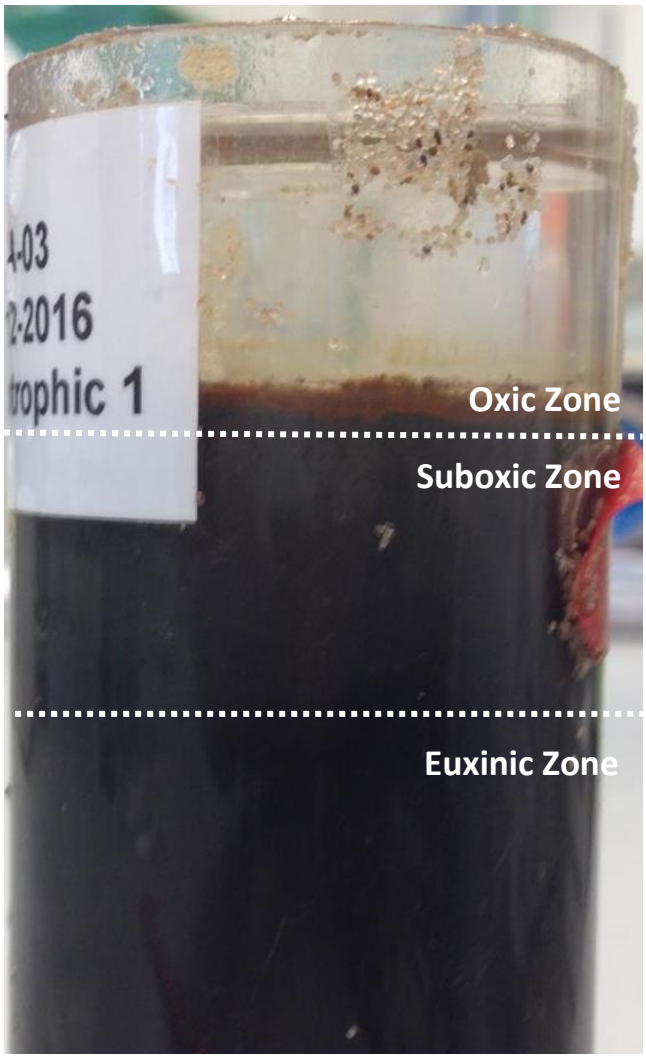

Figure iv. Incubated Rattekaai sediment. *This core has been incubated for 94 days at this point. Quite clearly the orange layer on top of the sediment can be seen. Notice also the lighter colour in the suboxic zone depth range due to dissolution of the black FeS-minerals. Unfortunately this colour difference is more easily appreciated in person than from a picture.*

Appendix V. Calculation of fluxes and consumption rate

Calculation of fluxes and diffusion coefficients

Table i. Overview of diffusive species within the context of this report. *D_0 is the standard diffusion coefficient as taken from literate. D_{sed} is the diffusion coefficient adjusted for the relevant sediment characteristics*.

SPECIES	D_0 ($*M^2*S^{-1}$) [40,41]	D_{SED} ($*M^2*S^{-1}$)
H_2S	$1{,}56*10^{-9}$	$6.77*10^{-10}$
HS^-	$1{,}51*10^{-9}$	$6.57*10^{-10}$
O_2	$2{,}02*10^{-9}$	$8.81*10^{-10}$
HCO_3	$1.01*10^{-9}$	$4.40*10^{-10}$
FE^{2+}	$6.5*10^{-10}$	$2.8*10^{-10}$

Example calculation:

The diffusion coefficient (T=21^{0}C , p =1 bar and Salinity= 32) was adjusted for sediment tortuosity using the following formula:

$$Dsed = \frac{D0*\varphi}{1-2\ln(\varphi\ )}$$ [28]

$$=\frac{1.56*10^{-9}*0.72}{1-2*\ln(0.72\ )}=6.77*10^{-9}\ (*m^{-2}*s^{-1})$$

ΣH_2S diffusing into the suboxic zone consisted of two species H_2S and HS^-. To reach one diffusion coefficient for the sulfide species H_2S and HS^-, the concentration of [H_2S] was integrated over the depth range 2.2-3.5 mm. Secondly the [H_2S] was converted, using pH, into Σ[H_2S] and subsequently integrated over the same depth range. This was performed using the mprplotter program available from the internet.[59] Thus, we found a value of 3.39 nmol*cm^{-2} for ΣH_2S and for H_2S a value of 2.89 nmol*cm^{-2} was found. Relative weight of H_2S is then 2.89/3.39=0.853 and for HS^-=1-0.853=0.147. Multiplying this weight with their corresponding diffusion coefficent yields a total diffusion coefficient for total sulfide of $6.73*10^{-10}$ m^{-2}*s^{-1}.

Determination of the flux was performed by taking the profile`s constant slope from the euxinic zone to the suboxic zone (figure v). Next, using this diffusion coefficient and Fick`s law over the range of 2.2 mm to 3.5 mm, we found a flux of 0.0033 mol*m^{-2}*day^{-1} for the Σ H_2S flux into the suboxic zone. For O_2 we performed the same procedure over the depth range 0 mm to 1.5 mm, and obtained a value of 0.013 mol*m^{-2}*day^{-1}.

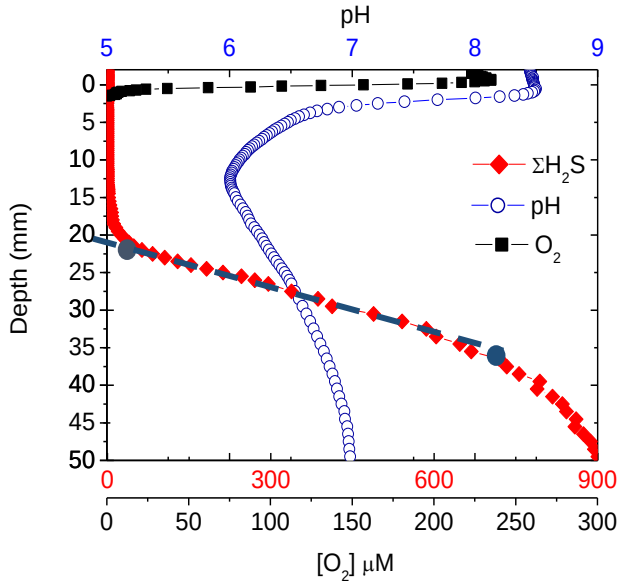

Figure v. Depiction of the method to obtain values for oxygen and sulfide fluxes into the suboxic zone from pH, O_2 and H_2S-Profiles. *The blue dotted line indicates the part of the graph employed to obtain the H_2S-influx into the suboxic zone from the euxinic zone.*

Iron flux determination

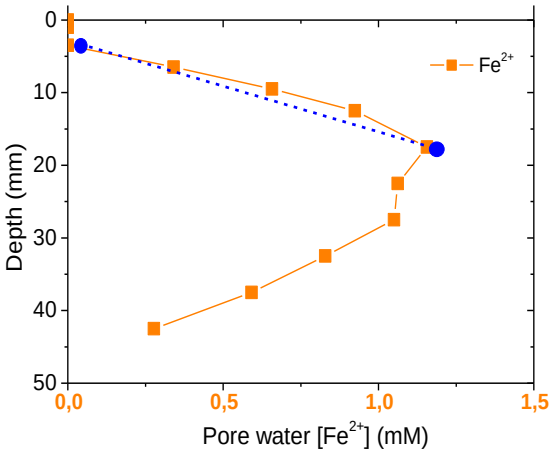

Figure vi. Iron profile from which SWI flux was determined. *Blue dots and the line indicate the depth range over which the flux was determined for ferrous iron flux towards the SWI.*

Because ferrous ions reach a considerable concentrations within the suboxic zone, it was necessary to add a term describing the electrostatic effect on its flux. This is described by the following equation (section 2.4, equation 2) :

$$J_{Fe2+} = -\phi * D_{sed} * [(\frac{dC}{dz} + \frac{nF}{RT} * C * \frac{d\psi}{dz})]$$

Using the values as in the text box and as concentrations of iron the points as indicated by the blue dots in figure vi ($17.5*10^{-3}$ m, 1.15 mol*m^{-3} and $3.5*10^{-3}$ m, 0 mol*m^{-3}) gives the following calculation:

F=Faraday Constant=96485 C*mol^{-1}
n=charge of the species=2
R=gas constant=8.3145 J*K^{-1}*mol^{-1}
T=temperature= 294 K
Z=distance over which flux was determined
$\frac{d\psi}{dz}$=-0.08 V*m^{-1}. [10]
C=average [Fe^2] in the range over which flux was determined=0.506 mol*m^{-3}
D_{sed}=$2.8*10^{-10}$ m^2*s^{-1} (iron)
ϕ=porosity of the sediment (section 3.1)

$$J_{Fe2+} = -0.72*2.8*10^{-10}*[(\frac{1.15-0}{(17.5-3.5)*10\text{^}-3} + \frac{2*96485}{8.3145*294} * 0.506 * 0.08)]$$

$$= -1.49 \text{ mmol*m}^{-2}\text{*d}^{-1}$$

Appendix VI. Depth specific rates of [ΣH_2S] production for both cores subjected to direct-rate measurements.

Table ii. Overview of depth specific rates in the suboxic zone for core 1. The average Initial slope of ΣH_2S-increase was *converted to mmol S*m^{-2}*min^{-1} by multiplying the depth-specific rate with the suboxic zone length. All presented values were averaged over 2 cycles.*

DEPTH (MM)	pH	Aereal ΣH_2S-consumption (mmol*m^{-2}*d^{-1})	Average Initial slope of H+-decrease (M*min^{-1})	Average Initial slope of ΣH_2S-increase (M*min^{-1})	Buffering Capacity (β)
CORE 1 DAY 12					
3.5	6.28	1.04	$1.45*10^{-9}$	$0.091*10^{-6}$	78
5.5	6.10	1.11	$5.02*10^{-9}$	$0.097*10^{-6}$	35
8.5	5.99	1.44	$6.73*10^{-9}$	$0.126*10^{-6}$	44
10.5	5.96	2.72	$1.45*10^{-8}$	$0.238*10^{-6}$	51
				Average	**52**
CORE 1 DAY 21					
5.5	6.23		$2.87*10^{-9}$	$0.091*10^{-6}$	53
7.5	6.14		$2.03*10^{-9}$	$0.139*10^{-6}$	39
				Average	**46**

Table iii. Overview of depth specific rates in the suboxic zone for core 2. Average initial slopes of ΣH_2S-increase were *converted to mmol S*m^{-2}*d^{-1} by multiplying the depth-specific rate with the suboxic zone length All presented values were averaged over 2 cycles.*

DEPTH (MM)	pH	Aereal ΣH_2S-consumption (mmol*m^{-2}*d^{-1})	Average Initial slope of H+-decrease (M*min^{-1})	Average Initial slope of ΣH_2S-increase (M*min^{-1})	Buffering Capacity (β)
CORE 2 DAY 12					
5.5	6.24	0.88	$4.59*10^{-9}$	$0.077*10^{-6}$	31
8.5	6.05	0.89	$7.49*10^{-9}$	$0.078*10^{-6}$	20
12	5.98	1.41	$8.02*10^{-9}$	$0.124*10^{-6}$	34
				Average	**28**
CORE 2 DAY 21					
5.5	6.23	0.79	$8.92*10^{-9}$	0.070	12
8	6.06	1.09	$6.30*10^{-9}$	0.095	26
				Average	**19**

Appendix VII. pH-direct rate measurement correlation

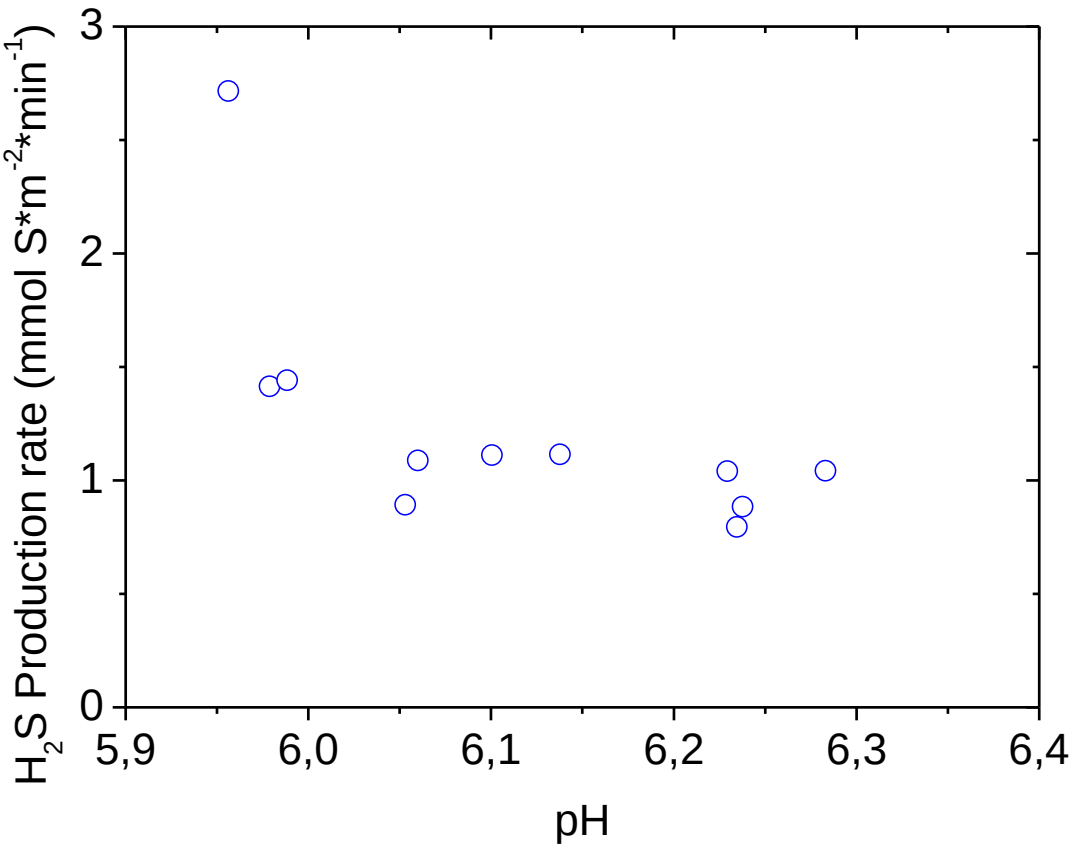

Figure vii. The correlation between pH and observed consumption rates. *Data points were collected at different depths and pH values on two independent cores incubated for 12 days.*

Appendix VIII. Overview of the fitted curves for core 1 day 12

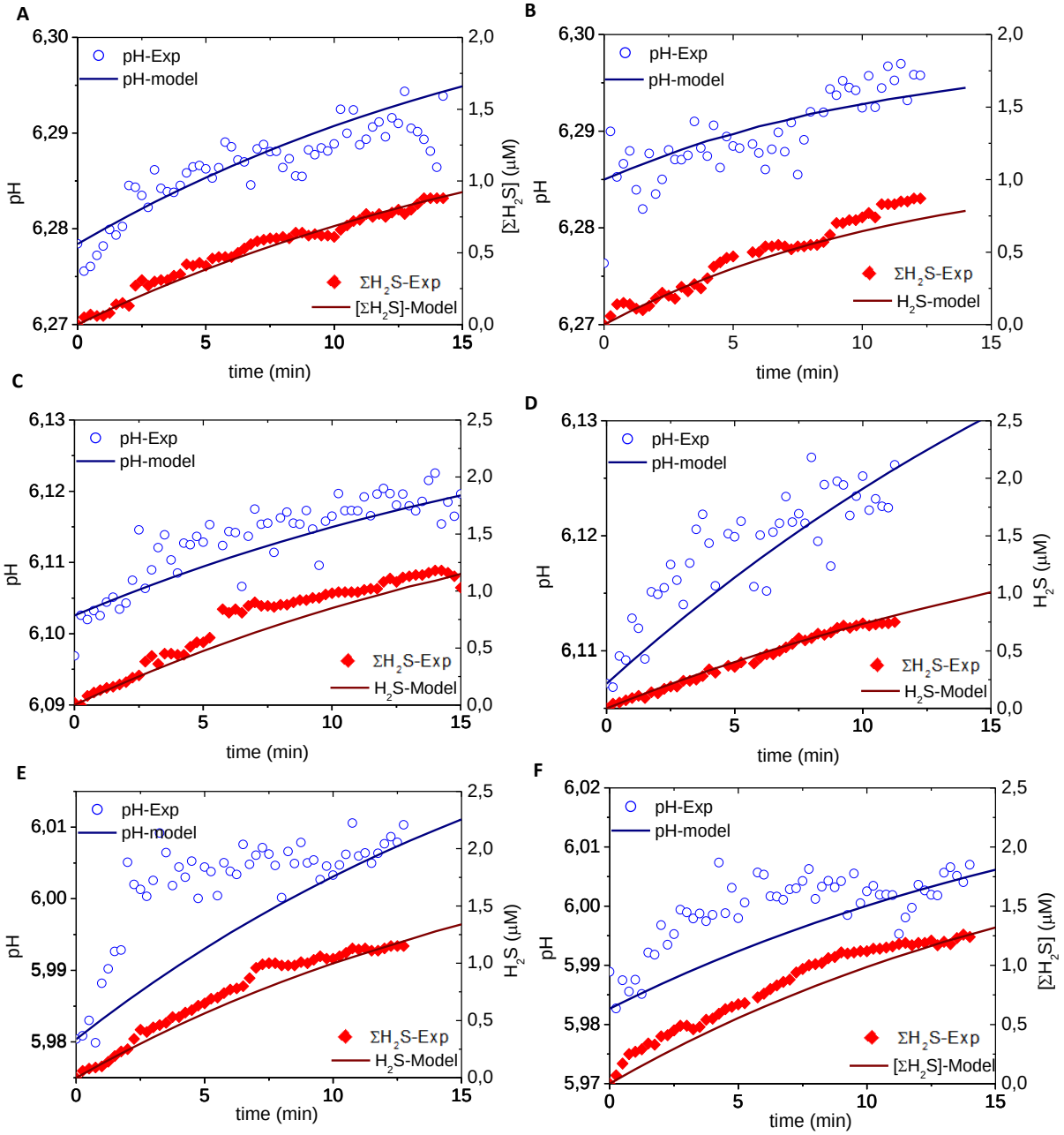

Figure viii. pH and ΣH_2S- dynamics, modelled and experimental curves, during anoxic perturbation at different depths. Panel A and B: depth of 3.5 mm: Cycle 1 and 2. Panel C and D: depth of 5.5 mm. Panel E and F: depth of 8.5 mm Cycle 1 and 2.

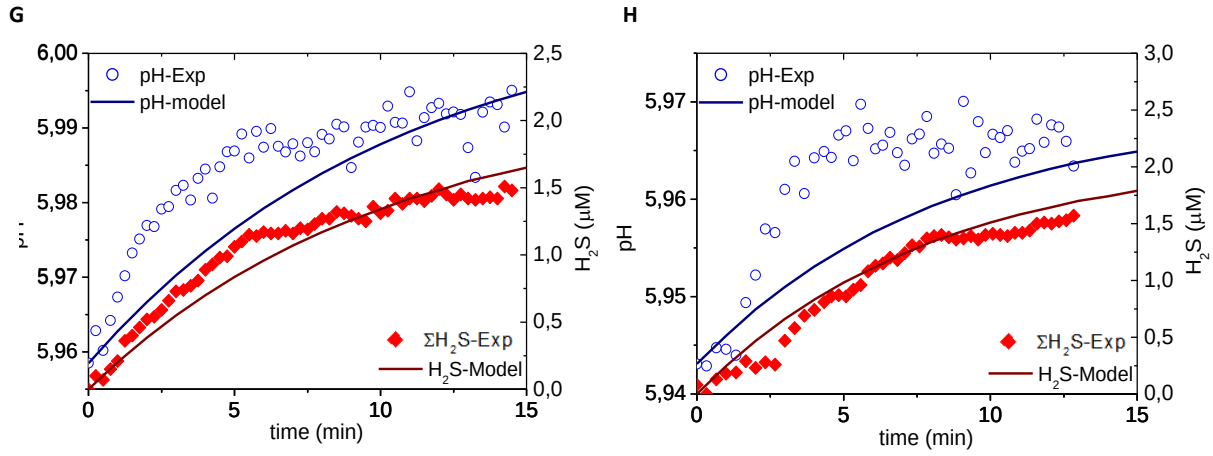

Figure viii. pH and ΣH_2S- dynamics, modelled and experimental curves, during anoxic perturbation at different depths. panel G and H: Depth of 10.5 mm cycle 1 and 2.

Appendix IX. Overview of the geochemical profiles for the two cores subjected to direct-rate measurements.

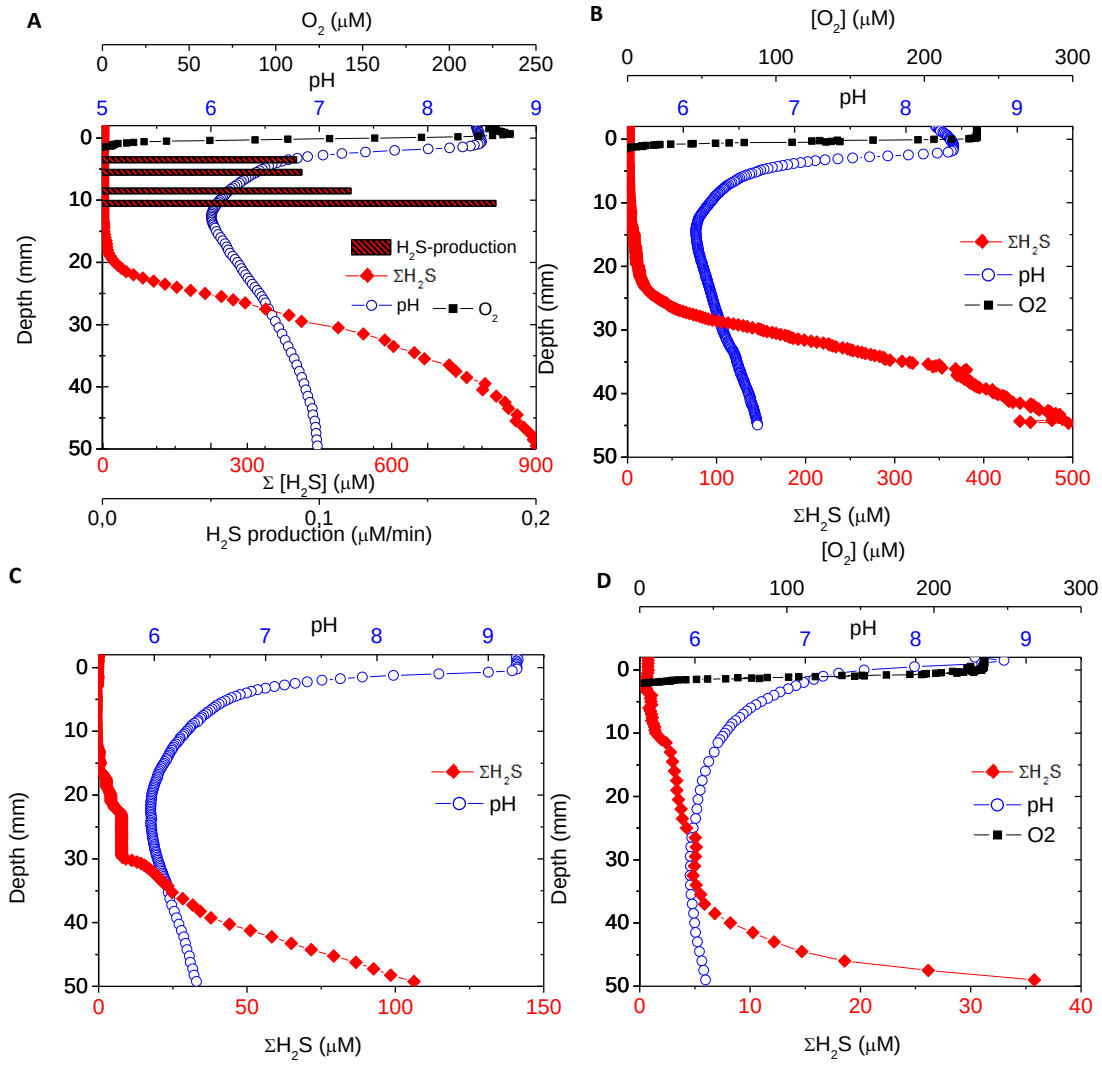

Figure ix. pH, O_2 and H_2S micro-sensor profiles for different cores at different incubated times. Panel A Core 1, incubated 12 days. Panel B: core 1, incubated 21 days. Panel C: Core 2, incubated 12 days. Panel C: core 2, incubated 21 days.

Appendix X. Artificial sea water composition

Table iv. Composition of Ca/Mg-free artificial sea water.

Dissolved molecule	Concentration (M)	Ionic specie	Concentration (M)
NaCl	$4.49*10^{-1}$	Na^{+}_{tot}	$4.70*10^{-1}$
KCl	$1.20*10^{-2}$	K^{+}_{tot}	$1.20*10^{-3}$
Na_2SO_4	$2.80*10^{-2}$	Cl^{-}_{tot}	$5.21*10^{-1}$
NaBr	$4.40*10^{-4}$	$SO_4^{2-}{}_{tot}$	$2.80*10^{-2}$
$SrCl*6\ H_2O$	$9.00*10^{-5}$	Br^{-}_{tot}	$4.40*10^{-4}$
		Sr^{+}_{tot}	$9.00*10^{-5}$

Appendix XI. Enrichment calculations in the porewater of the core

^{13}C-enrichment

Injection was performed into a circle with a 1 cm diameter. Dimensions of the volume into which injection were performed was as follows. Dimensions core: d (diameter)=0.01 m, h (height of colum) =0.06 m, ϕ(porosity))=0.72.

Total liquid volume(TLV) core= $\phi*\pi*h*(d/2)^2$=3.39*10^{-6} m^3= 3.4 ml

$DIC0$ =10 mM [H_2CO_3].[28]

^{13}C-FA(bg)=^{13}C natural enrichment (^{13}C/(^{12}C+^{13}C))=0.01.

Injected solution contained:

$DICinc$ =62 mM [H_2CO_3], F13Cinj=(0.99) 99% ^{13}C enriched, **Injected volume(IV)**=0.5 ml.

DIC0=*total carbonate before tracer injection*=1.78 mM
DIC1= *total carbonate after tracer injection*
DICinc=*[DIC] in injection liquid*=62 mM
IV=*Volume of injected liquid containing isotopically labelled compounds*=0.5 ml
TLV=*total liquid volume of the core*= 3.4 ml
^{13}C-E(bg)=*natural fractional abundance of 13C* =0.01
^{13}C-E(inj)=*fractional abundance of 13C in injected nutrients*=0.99
^{13}C-E(pw)=*Fractional abundance of porewater after injection*
ϕ=porosity of the sediment

Assuming complete displacement of present porewater , the new $[H_2CO_3]_{tot}$ becomes:

$$\frac{IV*[DICinc](62mM)+(TLV-IV)*[DIC0](20\ mM)}{TLV}$$

DIC1= 26 mM.

The portion of this that is enriched:

$$\mathrm{F13C1} = \frac{IV(0.5)*[DICinc](62mM)*\mathbf{13}\mathrm{C-E(inj)}(0.99)}{TLV*(DIC1)} + \frac{(TLV-IV)(3.4-0.5)*DIC0(20\ mM)*^{13}\mathrm{C-E(bg)}(0.01)}{TLV*(DIC1)}$$

^{13}C-E(pw)= $(\frac{13C}{12C+13C})$ = 0.35

^{15}N-enrichment

From the NH_4 geochemical profile it was found that the average NH_4 concentration was 0.47 mM.

We injected a 0.5 ml solution containing 0.35 mM $^{15}NH_4Cl$. Applying the previous type of calculation (using a background enrichment of 0.0037) we find an enrichment of 0.13.

Appendix XII. Background enrichment and natural fractionation

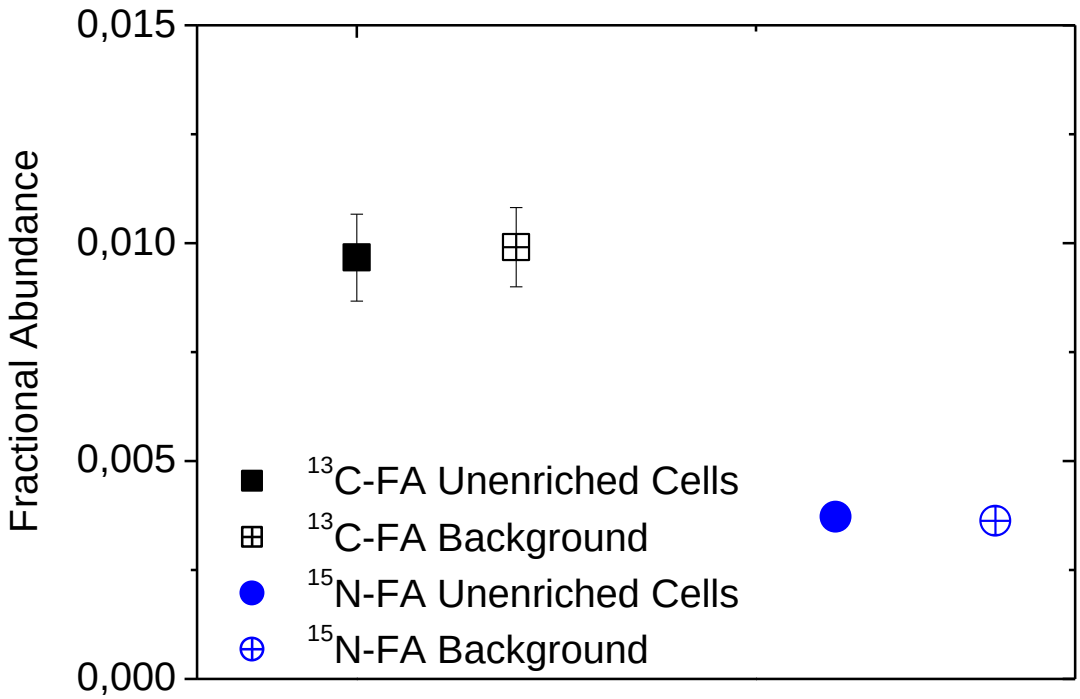

Figure x. Comparison of enrichment values for background and unenriched filaments. *Here presented are the mean ^{13}C- and ^{15}N- fractional abundances for unenriched cells and backgrounds. Indicated with the bars are the standard deviations.*

Appendix XIII. Filament count examples for the enriched samples from the suboxic zone

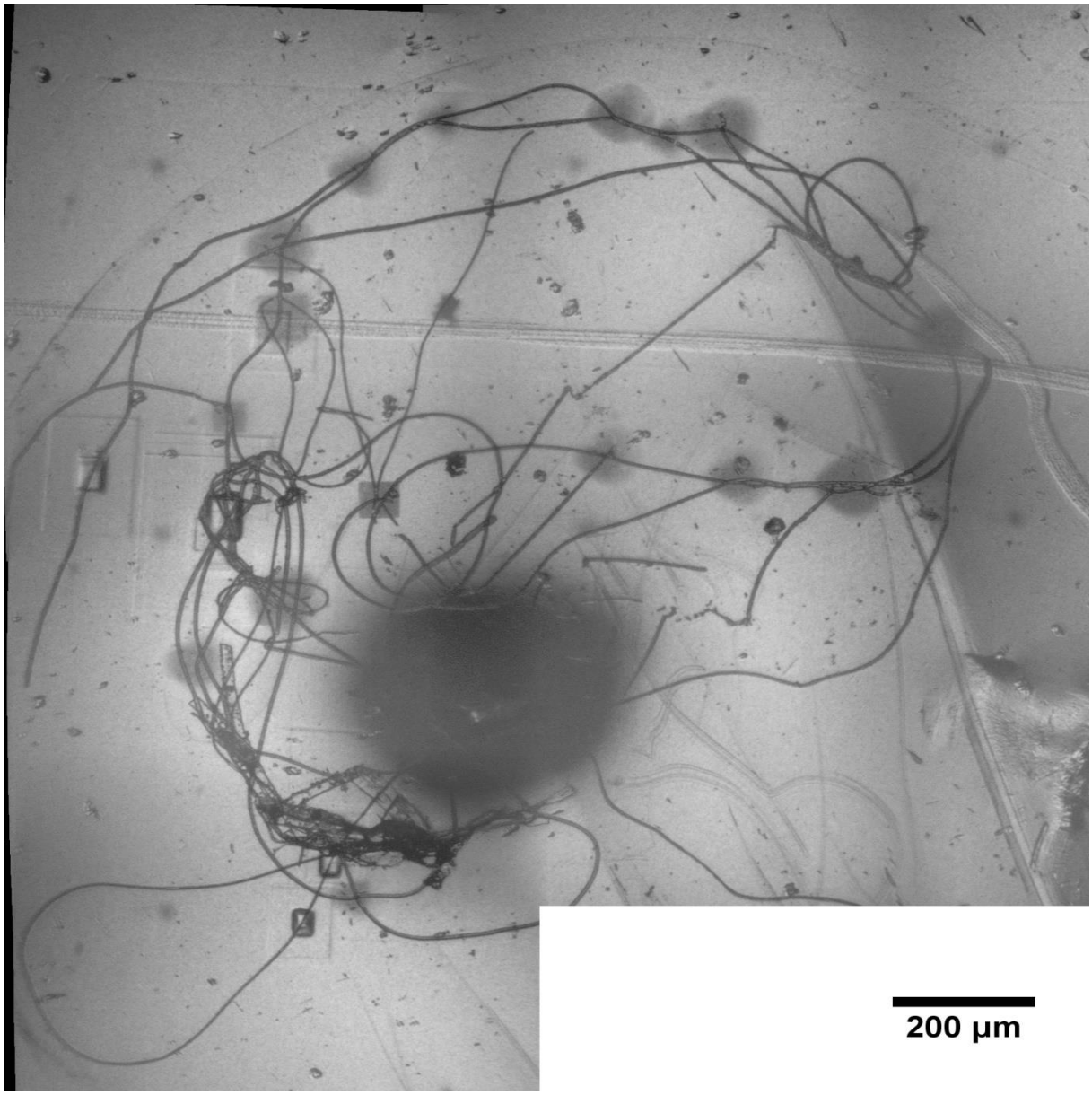

Figure xi. Untreated enriched samples that originated from the suboxic zone and was analysed with NanoSIMS. *Filaments A and C were enriched and mentioned in the text as filament A and C.*

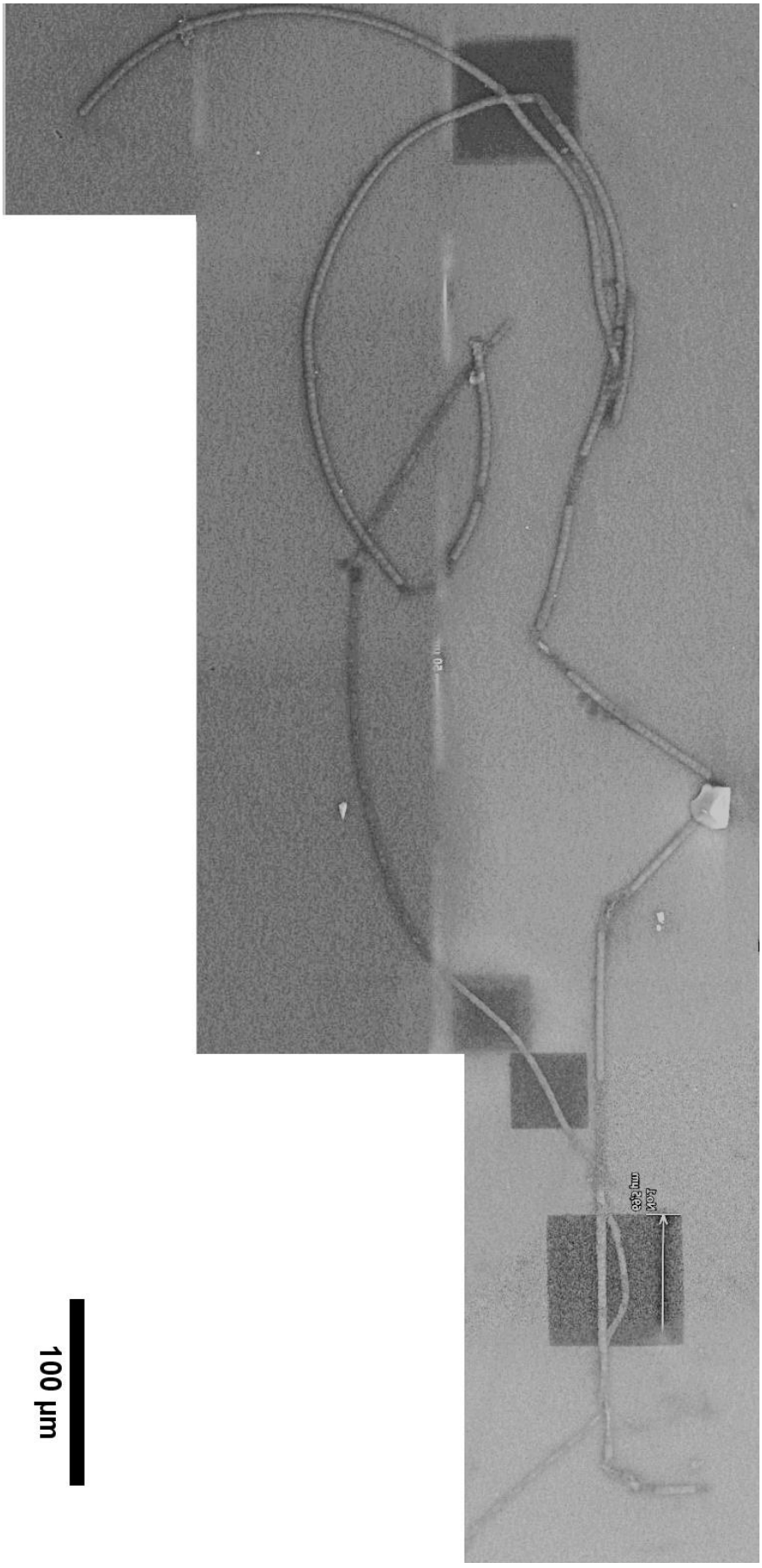

Figure xii. Enriched samples from the suboxic zone, treated with SDS and analysed using NanoSIMS. *These filaments were signified in the text as SDSA,SDSB and SDS C.*

Appendix XIV. Growth of cable bacteria and correlation between carbon and nitrogen uptake

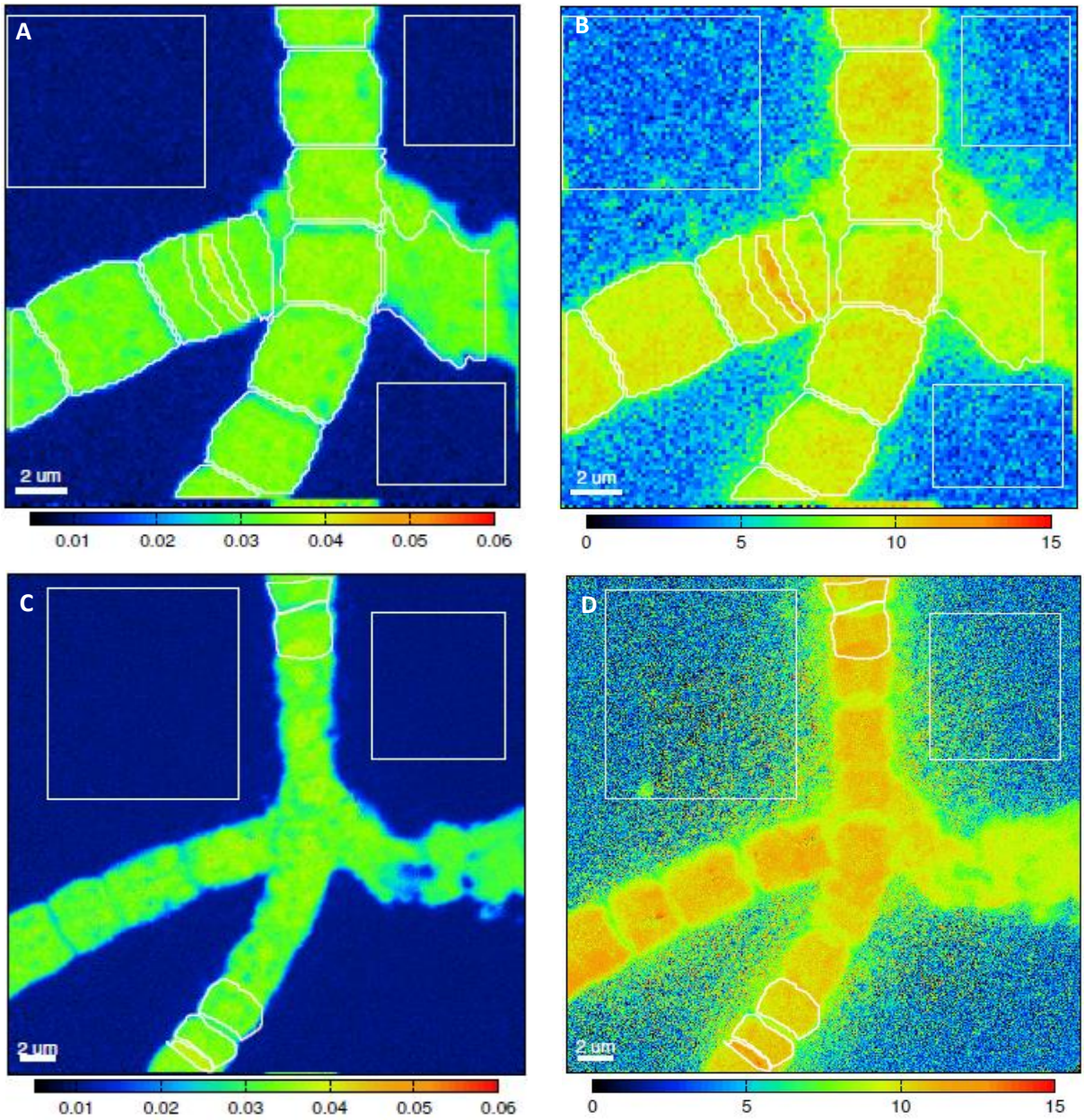

Figure xii. Images of ^{13}C and ^{15}N-enrichment for possible dividing cells of the filament. Panel A: ^{13}C-enrichment zoomed in. Panel B: ^{15}N-enrichment. Panel C: ^{13}C-enrichment zoomed out view Panel D: ^{15}N-enrichment zoomed out view. *Panel C and D are zoomed out compared to panel A and B, revealing another ostensibly dividing cell. The axis for ^{15}N-enrichment was in *10-3 (panel B and D). ^{13}C-enrichment was calculated as: $\frac{\square^{13}C}{\square^{13}C\square+\square^{12}C}$. ^{15}N enrichment was calculated as: $\frac{\square^{12}C^{15}N}{\square^{12}C^{14}N+\square^{12}C^{15}N}$*

Appendix XV. Enrichment along the filaments treated with SDS

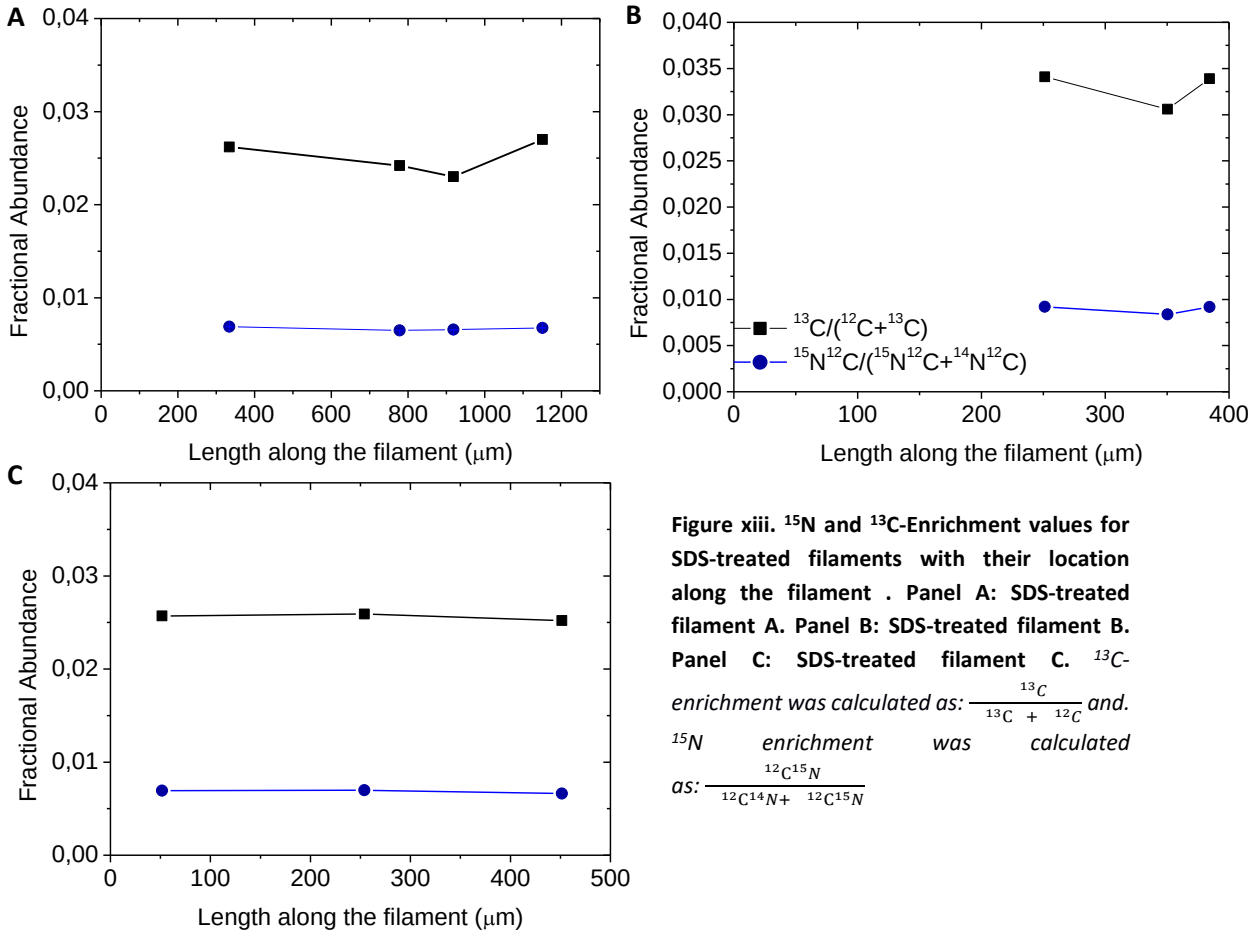

Figure xiii. ^{15}N and ^{13}C-Enrichment values for SDS-treated filaments with their location along the filament . Panel A: SDS-treated filament A. Panel B: SDS-treated filament B. Panel C: SDS-treated filament C. *^{13}C-enrichment was calculated as:* $\frac{^{13}C}{^{13}C + {}^{12}C}$ *and. ^{15}N enrichment was calculated as:* $\frac{^{12}C^{15}N}{^{12}C^{14}N + {}^{12}C^{15}N}$

Appendix XVI. Overview of the mean enrichment values of the enriched filaments

Table v. Overview of ^{13}C and ^{15}N- enrichment of the five enriched filaments, the variability on the cell level and the corresponding average assimilation rate constants. *^{13}C-enrichment was calculated as:* $\frac{^{13}C}{^{13}C + ^{12}C}$ *and. ^{15}N enrichment was calculated as:* $\frac{^{12}C^{15}N}{^{12}C^{14}N + ^{12}C^{15}N}$

FILAMENT	AVERAGE ^{13}C-ENRICHMENT OF THE FILAMENT (^{13}C-E(BM))	VARIABILITY ON A CELL LEVEL (CALCULATED AS STDEV)	AVERAGE ^{15}N-ENRICHMENT OF FILAMENT (^{15}N-E(BM))	VARIABILITY ON A CELL LEVEL (CALCULATED AS STDEV)	CARBON ASSIMILATION RATE CONSTANT ($C*C_{BIOMASS}^{-1}*D^{-1}$)	NITROGEN ASSIMILATION RATE CONSTANT ($N*N_{BIOMASS}^{-1}*D^{-1}$)
A	$3.21*10^{-2}$	$1.91*10^{-3}$	$1.01*10^{-2}$	$4.81*10^{-4}$	0.118	0.121
B	$1.40*10^{-2}$	$9.19*10^{-4}$	$4.67*10^{-3}$	$2.44*10^{-4}$	0.019	0.022
SDS-A	$2.55*10^{-2}$	$1.27*10^{-3}$	$6.72*10^{-3}$	$1.99*10^{-4}$	0.059	0.085
SDS-B	$3.29*10^{-2}$	$2.95*10^{-3}$	$8.83*10^{-3}$	$6.73*10^{-4}$	0.100	0.125
SDS-C	$2.44*10^{-2}$	$1.36*10^{-3}$	$6.64*10^{-3}$	$2.02*10^{-4}$	0.057	0.079